Structural interrogation of enzyme mechanism and dynamics

Dissertation

for the award of the degree
"Doctor rerum naturalium"
of the Georg-August-Universität Göttingen

within the doctoral program
Biomolecules: Structure – Function – Dynamics
of the Göttingen Graduate School for Neurosciences,
Biophysics, and Molecular Biosciences (GGNB)

submitted by
Alexander Mehr

from München, Germany

Max Planck Institute for Multidisciplinary Sciences

Göttingen, Germany

2023

Thesis Committee

Prof. Dr. Holger Stark
Structural Dynamics
Max Planck Institute for Multidisciplinary Sciences

Prof. Dr. Kai Tittmann
Molecular Enzymology
Georg-August-Universität Göttingen

Prof. Dr. Ricardo Mata
Computational Chemistry and Biochemistry
Georg-August-Universität Göttingen

Members of the Examination Board

1st Referee: Prof. Dr. Holger Stark
Structural Dynamics
Max Planck Institute for Multidisciplinary Sciences

2nd Referee: Prof. Dr. Ricardo Mata
Computational Chemistry and Biochemistry
Georg-August-Universität Göttingen

Dr. Ashwin Chari
Structural Biochemistry and Mechanisms
Max Planck Institute for Multidisciplinary Sciences

Dr. Alexander Stein
Membrane Protein Biochemistry
Max Planck Institute for Multidisciplinary Sciences

Dr. Alex Faesen
Biochemistry of Signal Dynamics
Max Planck Institute for Multidisciplinary Sciences

Prof. Dr. Henning Urlaub
Bioanalytical Mass Spectrometry
Max Planck Institute for Multidisciplinary Sciences

Date of oral examination: April 18th, 2023

Affidavit

I hereby declare that this dissertation with the title “Structural interrogation of enzyme mechanism and dynamics” has been written independently and with no other aids or sources than quoted.

Alexander Mehr

Göttingen, 17.02.2023

Acknowledgements

I am very grateful to Holger Stark and Ashwin Chari for have been given the opportunity to write my PhD thesis in their department. I am especially thankful for all the help from Ashwin who always had an sympathetic ear to discuss anything, be it of experimental or personal nature, and taught me how to tackle scientific questions. Thinking back, I have learned so much since I joined the lab as a master student in 2018, which I owe to Ashwin.
I am thankful for the members of my thesis advisory committee, Holger Stark, Kai Tittmann, and Ricardo Mata, who provided valuable insights during our meetings and were supportive in the course of my thesis. I want to thank Alexander Stein, Alex Faesen, and Henning Urlaub, for joining the examination board.
Several people were involved in this project, which I want to thank specifically. I want to thank Arwen Pearson for all the helpful advice during our Zoom meetings, as well as for the support during the time-resolved experiments at T-REXX. I want to thank Pedram Mehrabi, Eike Schulz, David von Stetten, and Michael Agthe, who set up the experiments at T-REXX, and provided a wonderful time during the night shifts. David von Stetten kindly processed the time-resolved data, which was a huge help. I am also grateful for the excellent P14 beamline provided by Thomas Schneider and the excellent beamline support by Gleb Bourenkov, who also performed the helical mesh scans.
I thank Vladimir Belov for the synthesis of MAP inhibitor. I also want to thank Cromarte Rogers for the proof-reading of my thesis, discussions about chemistry during our zoom meetings, and for the synthesis of the lipoamide analogue. I want to thank Trevor Huyton and Dirk Görlich for the generation of the alpaca nanobody sequence and provision of nedp1 protease, as well as Sabin Prajapati and Ai Woon Yee for initial biochemical characterization of the nanobody.
I want to also thank all past and present members of our department, who helped me tremendously during the last 4 years and provided an amazing work environment. Thanks to Emma for correcting my English. I could always rely on Gabi and Suzan who are the organizational backbone of the lab. I had a lot of fun with Kashish, Karl, Fabian, Lukas, Uma and Ben. I also want to thank present members of Team Halbstark: Lena, Eduardo, Alina and Justas, who provided a sporty balance to the office and lab work.
I would also like to thank Taalke, who was a huge support in the last 2.5 years, and also my family who have always supported me. I am very happy to have you all.

Abstract

The pyruvate dehydrogenase complex (PDHc) is one of the largest macromolecular enzyme complexes, and serves an universally important metabolic function by converting pyruvate into acetyl-CoA. Therefore, the PDHc connects glycolysis with the citric acid cycle, and fatty acid biosynthesis. The protein complex consists of the three different enzymes E1, E2, and E3, which catalyze pyruvate decarboxylation, acetyl transfer, and reoxidation of the lipoyl moiety sequentially. A small protein domain, which is attached to a flexible linker, transfers reaction intermediates to the different active sites in a process called substrate channeling. PDH deficiency leads to lethal neurological disorders, and the PDHc might be a valuable antibiotic target. Its importance for cellular function, and unique structural organization makes it an attractive target for structural investigations. Multiple crystal structures of its individual subunits have been elucidated. However, structures reported thus far were generally limited to 1.7-2.6 Å resolution, and little information is available about the interaction with its essential cofactor lipoamide. Furthermore, structural information of reaction intermediates and dynamics of the E1, a thiamine diphosphate dependent enzyme, have not been elucidated so far.

In this thesis, the full decarboxylation reaction of the *Bacillus subtilis* PDH E1 was analyzed by time-resolved serial crystallography. Parameters such as purification, micro-crystallization, sample delivery, and data collection were optimized. This lead to the collection of datasets with high completeness and reproducible diffraction to 2.3-2.5 Å. Structures of multiple time points during the reaction were elucidated. The time points showed a structural non-equivalence of the two active sites called half-of-the-sites reactivity. A post-crystallization protocol was established, which resulted in macro-crystals diffracting to high resolution. Multiple decarboxylation intermediates were elucidated at 0.95-1.03 Å, which helped the interpretation of the time-resolved data. The pre-decarboxylation intermediate exhibited enzyme mediated substrate- and cofactor bond distortions, which might contribute to its efficient catalysis. The post-decarboxylation intermediate showed a similar tautomeric equilibrium as observed in the pyruvate oxidase, which highlights common features of thiamine dependent enzymes. The high resolution allowed the visualization of a proton network connecting both active sites. A substrate mediated protonation asymmetry was observed, which could be a driving factor in half-of-the-sites reactivity. The structures also helped the elucidation of the E1 inhibition mechanism by fluoropyruvate. The formation of a tricyclic ThDP form including a seven-membered ring was observed.

High resolution structures of E2 and E3 enzymes in complex with the essential cofactor lipoamide were elucidated. These lead to the proposal of a new catalytic aspartate residue residing in a loop region, which closes its conformation upon cofactor binding. The E3-

lipoamide interaction was trapped for the first time, which showed, how flavin dependent oxidoreductases accommodate the thiol moieties of their respective substrates.
In summary, successful elucidation of reaction intermediates showed the complementarity of time-resolved crystallography and classical cryo-crystallography. Optimization of biochemical and technical protocols, such as post-crystallization, cryo-trapping, and data collection strategies, lead to the discovery of previously unobserved structural details of all three subunits of the pyruvate dehydrogenase complex in high spatial and temporal resolution.

Contents

Abbreviations

6AH	6-(acetylthio)hexanoic acid
8AO	8-(acetoamido)octanoic acid
Å	Ångström
ATP	Adenosine triphosphate
BCDHc	Branched chain α-ketoacid dehydrogenase complex
CAP	α-keto-isocaproate
CC	Correlation coefficient
CD	Catalytic domain
CoA	Coenzyme A
DESY	Deutsches Elektronen Synchrotron
DMSO	Dimethyl sulfoxide
DNA	Deoxyribonucleic acid
dNTP	Deoxy Nucleoside triphosphate
DTT	Dithiothreitol
E3BP	E3 binding protein
EDO	Ethylene glycol
EDTA	Ethylenediaminetetraacetic acid
EM	Electron microscopy
EMBL	European Molecular Biology Laboratory
ESRF	European Synchrotron Radiation Facility
FAD	Flavin adenine dinucleotide
GF	Gel filtration
GOL	Glycerol
HARE	Hit and return
IPTG	Isopropyl β-D-1-thiogalactopyranoside
kDa	Kilo Dalton
keV	Kilo electron volt
LAMA	Liquid application method for time-resolved analyses
LB	Lysogeny broth
LBHB	Low barrier hydrogen bond
LD	Lipoyl domain
MAP	Methyl acetyl phosphonate
MPD	2-methyl-2,4-pentandiol
MPINAT	Max Planck Institute for Multidisciplinary Sciences

MVA	α-keto-methylvalerate
NAD	Nicotinamide adenine dinucleotide
NB	Nanobody
Ni-NTA	Nickel-nitrilotriacetic acid
NMR	Nuclear magnetic resonance
ODHc	2-oxoglutarate dehydrogenase complex
OXO	2-oxoglutarate
PAGE	Polyacrylamide gel electrophoresis
PCR	Polymerase chain reaction
PDB	Protein Data Bank
PDHc	Pyruvate dehydrogenase complex
PDK	Pyruvate dehydrogenase kinase
PDP	Pyruvate dehydrogenase phosphatase
PEG	Polyethylene glycol
PMSF	Phenylmethylsulfonyl fluoride
PSBD	Peripheral subunit binding domain
RMSD	Root mean square deviation
SAM	S-adenosylmethionine
SDS	Sodium dodecyl sulfate
SSX	Serial synchrotron X-ray crystallography
TB	Terrific broth
TCA	Tricarboxylic acid
TCEP	Tris-(2-carboxyethyl)phosphine
TEV	Tobacco Etch Virus
ThDP	Thiamine diphosphate
Tris	Tris-(hydroxymethyl)aminomethane
TRX	Time-resolved X-ray crystallography
UV-Vis	Ultraviolet-visible
XFEL	X-ray Free Electron Laser

List of tables

List of figures

1 Introduction

1.1 Macromolecular protein complexes

Proteins play important roles inside the cell. Their function ranges from structural support to catalysis of a variety of reactions in signaling, transport, DNA replication and metabolism. Some enzymes have evolved to form larger protein assemblies which use substrate channeling processes, i.e., the transport of substrates and products to multiple reaction sites without their release to the environment. Physiological advantages of substrate channeling are the shielding of toxic or labile reaction intermediates from the cellular environment [1], the protection of intermediates from competing reactions, and the enhancement of catalytic activity [2]. Prominent examples of macromolecular protein complexes include the proteasome, the fatty acid synthase, the spliceosome, and 2-oxoacid dehydrogenase complexes. 2-oxoacid dehydrogenase complexes are large macromolecular protein complexes with a size of up to 11 MDa [3]. Three different 2-oxoacid dehydrogenase complexes exist within the cell: The oxoglutarate dehydrogenase complex (ODHc), the branched-chain α-ketoacid dehydrogenase complex (BCDHc), and the pyruvate dehydrogenase complex (PDHc). Their substrates are 2-oxoglutarate, branched-chain α-ketoacids, and pyruvate, respectively. They have been subject to studies for over 60 years since their initial isolation in the 1960s [4,5], but still garner great interest due to their unique structural organization and vital role in cellular metabolism.

1.1.1 Role of 2-oxoacid dehydrogenase complexes in metabolism and disease

ODHc, also known as the α-ketoglutarate dehydrogenase complex, catalyzes a reaction in the citric acid cycle. It converts α-ketoglutarate to succinyl-CoA while producing CO_2 and nicotinamide adenine dinucleotide (NADH). Succinyl-CoA can either proceed in the citric acid (TCA) cycle to generate reducing equivalents such as NAD and flavin adenine dinucleotide (FAD) or it undergoes substrate level phosphorylation in the absence of oxygen [6]. The reducing equivalents (in the form of NADH and $FADH_2$) can enter the electron transport chain for energy production via oxidative phosphorylation. Deficiencies of the ODHc are often accompanied by severe neurological disorders [7]. The BCDHc takes part in the branched-chain amino acid catabolism. It converts the ketoacids of leucine, isoleucine and valine to isovaleryl-CoA, 2-methylbutyryl-CoA, and isobutyryl-CoA, respectively [8]. This reaction also yields CO_2 and NADH. Deficiencies of the BCDH complex can lead to maple syrup urine disease, where the sweet urine odor of affected patients lead to its

name. Other symptoms of BCDH deficiency include developmental delay and feeding difficulties [9]. The PDH complex occupies a key role in cellular metabolism. This is evidenced by the fact that proteins from the PDHc belong to the 50 most abundant proteins in the cell [10]. It converts pyruvate generated in glycolysis to acetyl-CoA. Acetyl-CoA can enter the TCA cycle to form citrate along with oxaloacetate [11,12]. Acetyl-CoA can be metabolized as starting block for fatty acid biosynthesis [13]. Therefore, it connects several essential metabolic pathways. Loss of function mutations in the proteins of the PDH complex can be lethal [14]. Symptoms of PDHc deficiency are neurological disorders, developmental delay and mitochondrial acidosis [15]. A study identified the PDHc as potential target for antimicrobials [16].

1.1.2 Structural organization of the pyruvate dehydrogenase complex

All 2-oxoacid dehydrogenase complexes share similar structural features. They are all comprised of multiples of three different enzymes that act sequentially. The PDHc, for example, consists of the pyruvate dehydrogenase (E1), dihydrolipoyl transacetylase (E2) and dihydrolipoyl dehydrogenase (E3) [17]. Figure 1.1 shows the schematic organization of the PDHc. The core of the complex is formed by non-covalent interactions between multiple E2 subunits. 2-oxoacid dehydrogenase cores are either assembled as a cube or a dodecahedron. 24 E2 subunits form a cubic core, for example in the ODHc and BCDHc of bacteria, plants and eukaryotes, or in the PDHc of gram negative bacteria, such as *Escherichia coli*. 60 E2 subunits form an icosahedral, ball shaped, hollow core structure in eukaryotes and in most gram-positive bacteria such as *Geobacillus stearothermophilus* [18-20]. The E2 subunits consist of three different domains: The catalytic domain (CD), the peripheral subunit binding domain (PSBD), and the lipoyl domain (LD) (figure 1.1) [21]. The catalytic domain of the E2 enzyme forms trimers, which sit on the vertices of the cubic or dodecahedral complexes. Both E1 (blue) and E3 (orange) subunits are bound by the E2 (green) in a mutually exclusive manner. Non-covalent binding is mediated by the PSBD, which is connected to the CD via an alanine and proline rich, flexible linker region. In eukaryotic PDH complexes the E3 is bound by an additional component, the E3 binding protein (E3BP) [22]. The PSBD is connected to the LD via another flexible interdomain linker. The LD shuttles reaction intermediates between the E1, E2 and E3, and therefore mediates substrate channeling. While the E1, and E2 enzymes are unique to their respective 2-oxoacid dehydrogenase complex, the E3 is shared by PDHc, ODHc, BCDHc and the glycine cleavage system [17,23]. The core can bind up to 60 copies of E1 enzymes in the absence of E3 subunits and vice versa [24].

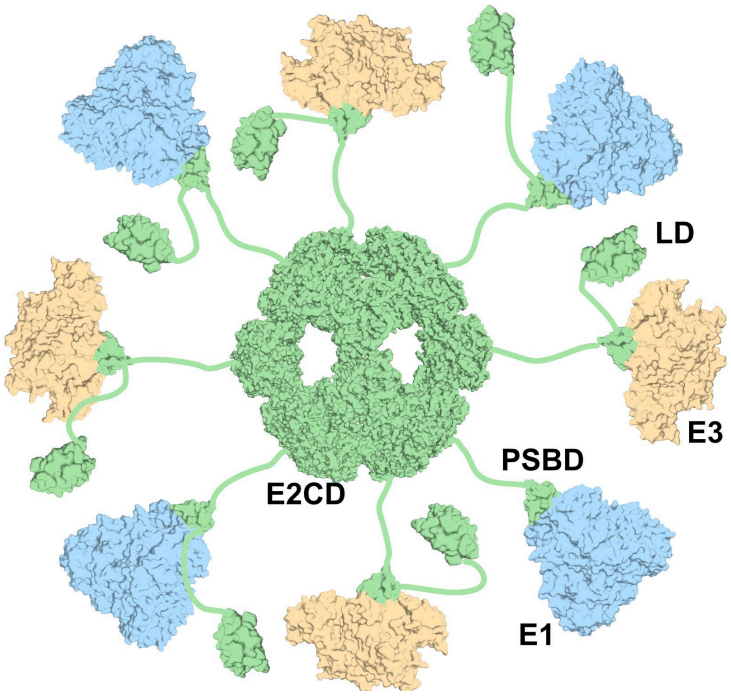

Figure 1.1: Schematic organization of the icosahedral pyruvate dehydrogenase complex. Structures of the *Geobacillus stearothermophilus* PDH E1 (PDB ID: 1W85), E2 core (PDB ID: 1B5S), E2 lipoyl domain (PDB ID: 1LAC) and E3 (PDB ID: 1EBD) subunits are arranged schematically into an icosahedral PDH complex. 60 E2 subunits (green) assemble into the icosahedral core. The PSBD, which binds E1 (blue) and E3 (orange) non-covalently, is attached to the core by a flexible linker. The PSBD is connected to the LD by another linker region. The LD mediates substrate channeling by shuttling reaction intermediates between the three active sites. Adapted from Goodsell, Molecule of the month [25].

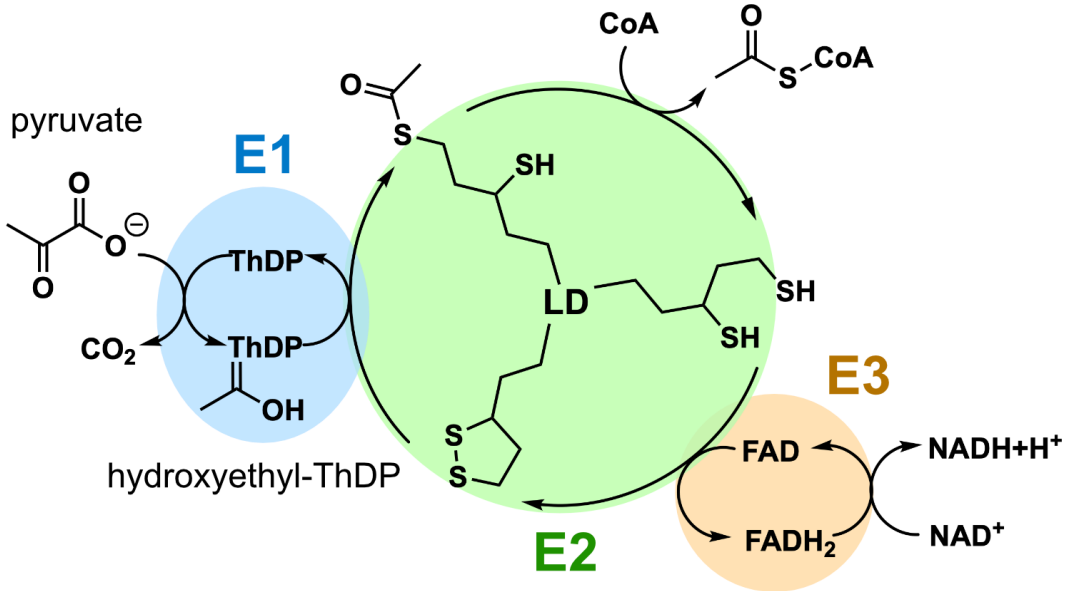

Figure 1.2: The reaction cycle of the pyruvate dehydrogenase complex. The E1 subunit (blue) decarboxylates pyruvate, which leaves an acetyl group covalently attached to its cofactor thiamine diphosphate (ThDP) in the form of hydroxyethyl-ThDP. The lipoyl group, covalently attached to a flexible domain of the E2 (green), transfers the acetyl group from the E1 to coenzyme A (CoA) in the E2 active site to yield acetyl-CoA. The reduced lipoyl group is reoxidized by the E3 subunit (orange), which reduces NAD^+ to NADH with the help of its cofactor FAD. Modified from [26].

The exact stoichiometry of E1:E2:E3 is not known, since expression and purification protocols, as well as assembly *in vivo* or *in vitro* might influence subunit stoichiometry. So far, the complete structure of the PDHc has not been elucidated as yet due to its inherent flexibility and dynamics [27]. Figure 1.2 shows the reaction cycle of the PDHc. The E1 decarboxylates pyruvate with the help of its cofactor thiamine diphosphate (ThDP), a vitamin B1 derivative. An acetyl moiety remains covalently bound to the cofactor after decarboxylation, which is then termed hydroxyethyl-ThDP. The E2 LD transfers the acetyl group to the E2 CD active site to yield acetyl-CoA. The prosthetic group responsible for the transfer is called the lipoyl group. After reductive acetyl-transfer, the LD shuttles the reduced lipoyl group to the E3 active site, which regenerates the complex by re-oxidation of the dithiolane ring. Re-oxidation produces the reducing equivalent NADH.

1.1.3 Regulation of the pyruvate dehydrogenase complex

The PDHc is present in most organisms. In prokaryotes the PDHc is located in the cytoplasm, in eukaryotes, the PDHc resides in mitochondria and plastids. The PDHc is an important metabolic gatekeeper. As a consequence, it is regulated extensively. In *E. coli*, the PDHc is transcriptionally regulated, for example by the transcription factor PdhR [28]. Transcription of the *pdh* operon is repressed by PdhR. When pyruvate is available, a PdhR-pyruvate complex is formed, which is not able to bind DNA. As a consequence, transcription of the *pdh* operon is activated. In eukaryotes, PDHc is regulated post-translationally. Pyruvate dehydrogenase kinases (PDK) can inactivate the PDHc by phosphorylation of the E1. The site of phosphorylation are three different serine residues in a loop adjacent to the active site of the E1 subunit [29]. Pyruvate dehydrogenase phosphatases (PDP), on the other hand, activate the E1 by dephosphorylation. The activity of the kinases is regulated by substrate and product concentrations [30]. For example, NADH and acetyl-CoA stimulate PDKs, whereas CoA, NAD^+, ADP, and pyruvate inhibit PDK activity. Metabolic pathways are often regulated at irreversible steps. The same holds true for the PDHc, since decarboxylation by E1 is an irreversible reaction.

1.2 Enzymatic vs non-enzymatic decarboxylation reactions

In cells, a variety of metabolites are decarboxylated. Different cofactors have evolved over time to facilitate decarboxylation of very stable reactants. One example for such a cofactor is pyridoxal phosphate (PLP). PLP, or vitamin B6 phosphate, is a cofactor in a variety of reactions such as trans-amination reactions and decarboxylation of amino acids. The cofactor is usually covalently attached to a lysine residue, called an internal aldimine. It forms

a Schiff base with the incoming amine of amino acids, termed external aldimines, to facilitate decarboxylation [31]. Another example is thiamine diphosphate (ThDP). ThDP dependent enzymes generally facilitate efficient C-C bond cleavage such as in the decarboxylation of α-ketoacids, for example pyruvate decarboxylase and pyruvate oxidase, the cleavage of sugars, for example transketolase in the pentose phosphate pathway, or cleavage of branched acyl-CoA in the 2-hydroxyacyl-CoA lyase [32-34]. A similar mechanism underlies cofactor mediated decarboxylation reactions. Both PLP or ThDP act as an electron "sink", which stabilizes the free electron pair resulting from C-C cleavage, for example after decarboxylation of α-keto-acids or amino acids. Figure 1.3 compares the reaction conditions for enzymatic and non-enzymatic decarboxylation of different ketoacids. Enzymatic decarboxylation of pyruvate by the PDHc and acetoacetate by the acetoacetate decarboxylase (ADC) requires mild reaction conditions such as room temperature and neutral pH [35,36]. Some β-ketoacids, such as acetoacetic acid, readily decarboxylate upon heating. In contrast, α-ketoacids such as pyruvate, do not decarboxylate upon heating and require high temperatures and catalysts such as cyanide for decarboxylation in chemical reactions [37,38].

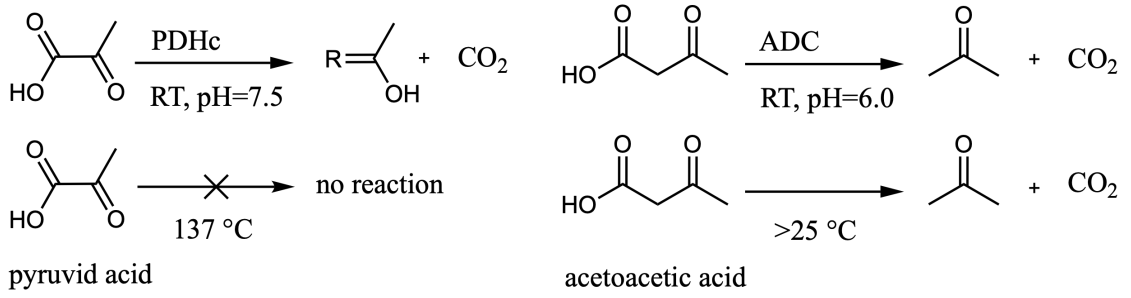

Figure 1.3: Reaction conditions of enzymatic and non-enzymatic decarboxylation of α-ketoacids. Enzymatic and non-enzymatic reaction conditions for the decarboxylation of pyruvic acid and acetoacetic acid are shown. Enzymatic decarboxylation occurs at mild reaction conditions. β-ketoacids readily decarboxylate upon heating, while α-ketoacids do not decarboxylate upon heating.

It is important to understand enzymatic decarboxylation mechanisms, since enzymatic decarboxylation can be an environmentally friendly path in material synthesis, energy production or other industrial applications [39]. The *Escherichia coli* E1, for example, was modified to catalyze stereoselective carbo-ligation reactions [40].

1.3 The pyruvate dehydrogenase E1

The E1 of the PDHc is a protein complex consisting of a dimer in gram-negative bacteria such as *E. coli* (figure 1.4A), or two α- and β- subunits forming a hetero-tetramer in humans and gram-positive bacteria (figure 1.4B). It belongs to the family of thiamine diphosphate (ThDP) dependent enzymes. Each E1 complex contains two active sites, which are formed

at the interface of α- and β-subunits in the hetero-tetrameric form [41,42]. The E1 catalyzes two reactions sequentially: Oxidative decarboxylation of pyruvate and transfer of the acetyl group to the lipoyl arm via reductive trans-acetylation.

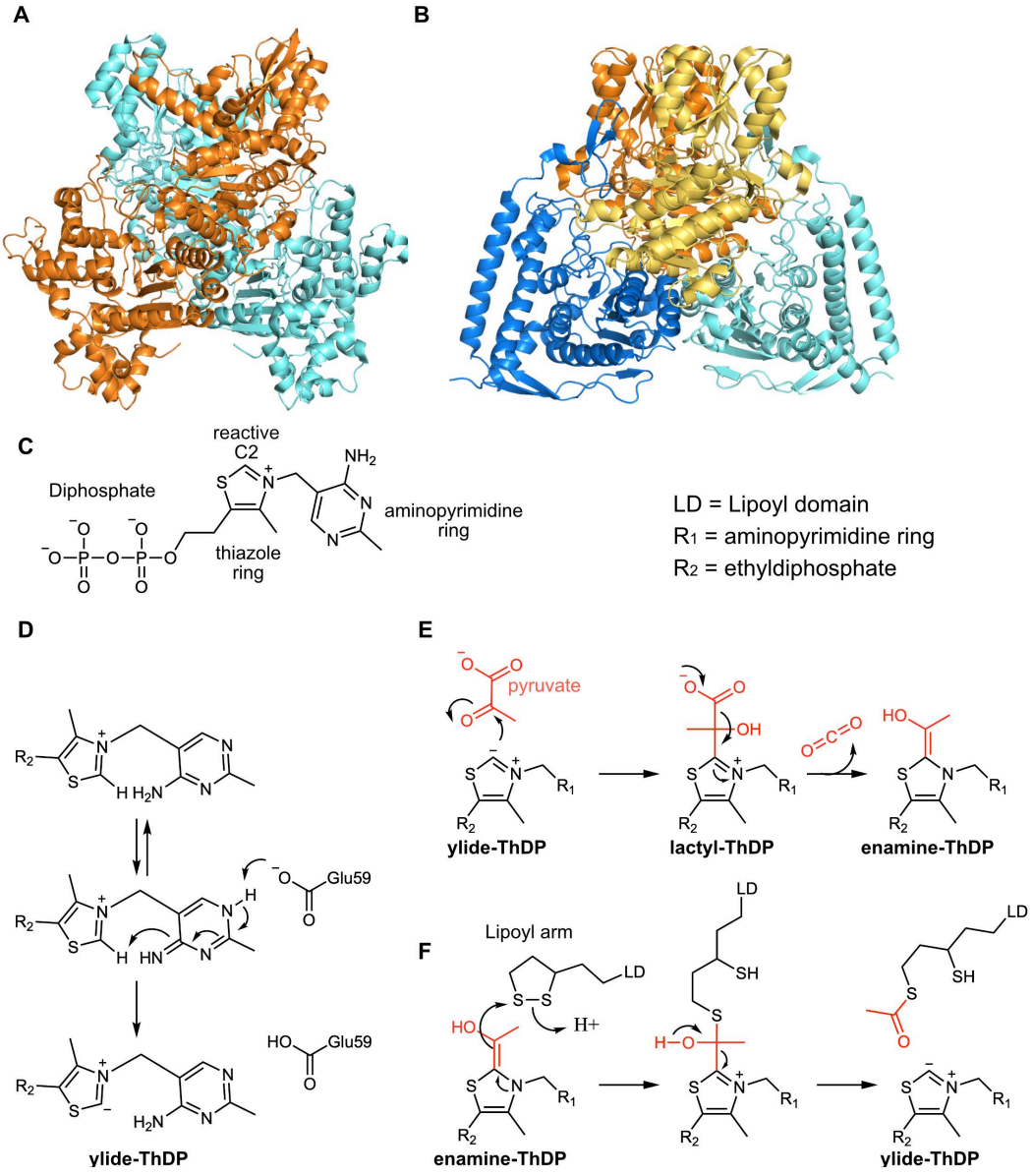

Figure 1.4: Crystal structure and reaction mechanism of the PDHc E1. A) Cartoon representation of the *Escherichia coli* PDHc E1 dimer (PDB ID:2G67). The two subunits are depicted in blue and orange. B) Cartoon representation of the human PDHc E1 (PDB ID: 1NI4). Human E1 is a heterotetrametric protein with two α (cyan and blue) and two β subunits (orange and yellow). C) The chemical structure of thiamine diphosphate is shown. D) Thiamine diphosphate is activated by conserved glutamate residue (Glu59 in humans), which deprotonates N4′ of the aminopyrimidine ring. This leads to proton abstraction from C2 of the thiazole ring forming the reactive ylide. E) Nucleophilic attack of the ketone carbon of pyruvate (red) by the reactive C2 leads to formation of the pre-decarboxylation intermediate lactyl-ThDP. Lactyl-ThDP is decarboxylated to yield the post-decarboxylation intermediate enamine-ThDP. F) A potential reaction mechanism of reductive transacetylation is shown. Enamine-ThDP facilitates a nucleophilic attack on the dithiolane ring, which results in formation of a tetrahedral intermediate. The intermediate collapses to yield the free ylide and the acetylated lipoyl group.

Both reactions are catalyzed with the help of ThDP. ThDP, a derivative of vitamin B1, contains a diphosphate group, a thiazole ring, which is a nitrogen and sulfur containing heterocycle, and an aminopyrimidine ring (figure 1.4C). Breslow identified the C2 of the thiazole ring as the reactive atom [43,44]. C2 needs to be deprotonated to facilitate a nucleophilic attack, but the pKa is high in solution. Therefore it needs to be activated by the enzyme [45]. The cofactor is activated by the conserved glutamate residue Glu59, which deprotonates N1´ (Figure 1.4D). Deprotonation leads to proton transfer from C2 to N4´ of the aminopyrimidine ring, which leads to formation of a reactive ylide [46]. A ylide is characterized by adjacent positive and negative charges. There is an ongoing debate, whether the reactive form of ThDP is a carbanion or a carbene. A stable carbene has been observed in the pyruvate oxidase of *Lactobacillus plantarum*, for example, which catalyzes the conversion of phosphate and pyruvate into acetyl phosphate [47]. The proposed mechanism for pyruvate decarboxylation by the E1 is depicted in figure 1.4E: In a first step, the C2 carbanion/carbene nucleophile attacks the ketone carbon of pyruvate, which results in the pre-decarboxylation intermediate lactyl-ThDP. Pyruvate is decarboxylated, which results in the post-decarboxylation intermediate enamine-ThDP, which has been termed the Breslow intermediate after its discovery by Ronald Breslow in 1958 [44]. Reductive trans-acetylation is catalyzed with the help of the lipoyl arm of the LD, which contains a dithiolane ring. Different mechanisms for reductive trans-acetylation have been postulated [48-54]. One mechanism is shown in figure 1.4F, where the enamine attacks the disulfide and the S6 sulfur is protonated concertedly, which leads to formation of a tetrahedral intermediate. This intermediate collapses back into ylide-ThDP and acetylated lipoyl group. As a consequence, the lipoyl arm leaves the active site towards the E2. Another mechanism involves reduction of the enamine to acetyl, which then undergoes nucleophilic attack by a thiolate of the lipoamide. Several studies have been conducted that provide evidence for both mechanisms, but a lack of structural data for the interaction between the lipoamide and E1 precludes further elucidation of the underlying mechanism.

1.4 Half-of-the-sites reactivity and low-barrier hydrogen bonds

Another aspect of the E1, which is not fully understood, is its active site asymmetry during catalysis, termed half-of-the-sites or alternating-sites reactivity. Many multi-subunit enzymes display half-of-the-sites reactivity, which is a form of negative cooperativity, where only one enzyme active site is active at a time [55-57]. Most ThDP dependent enzymes are dimers and therefore contain two active sites. Several studies have shown that there are structural and temporal differences between the two active sites during pyruvate decarboxylation. Phosphorylation of one active site of the human PDHc E1, for example, inactivated

the whole dimer [58]. Kinetic evidence was reported, where the rate of cofactor activation, substrate binding, and turnover is faster in one active site [59]. Since then, alternating-sites reactivity has been termed a common theme in thiamine diphosphate dependent enzymes [60]. Two models have tried to explain the underlying cause. One mechanism based on theoretical calculations was termed flip-flop mechanism, where structural changes in the active site lead to asymmetries in the E1 protein complex [61]. Another model was suggested after the discovery of a proton channel connecting two active sites in the *Bacillus stearothermophilus* PDH E1. This model does not involve major structural motions, but communication of the active sites via a proton wire [62].

A special type of hydrogen bond which is involved in enzyme cooperativity and catalysis is the low-barrier hydrogen bond (LBHB) [63,64]. LBHBs are hydrogen bonds, which are equally shared between the bond donor and acceptor pair. LBHBs have been detected in a variety of protein structures including subtilisin, photoactive yellow protein, and chymotrypsin [65-67]. Other authors postulated a LBHB-facilitated general base mechanism in serine proteases [68]. High resolution crystal structures of thiamine diphosphate dependent enzymes such as the *Lactobacillus plantarum* pyruvate oxidase (LpPOX), and the human transketolase (HsTK), revealed the formation of low-barrier hydrogen bonds (LBHB) between ThDP and residues inside the channel connecting both active sites [47,63,69]. Substitution of residues participating in LBHB formation disrupted the LBHB. As a consequence, active site cooperativity was lost. The occurrence of LBHBs in the E1 has not been reported so far.

Decarboxylation of pyruvate and reductive trans-acetylation are the first steps of a multistep reaction involving three different enzymes. The next steps are catalyzed by the E2 enzyme.

1.5 The PDH E2 – domain architecture

The E2 subunit forms the “core” of PDHc and catalyzes the acetyl-transfer from ThDP to CoA resulting in acyl-CoA. The protein is comprised of three domains: the lipoyl domain (LD), peripheral subunit binding domain (PSBD), and a C-terminal catalytic domain (CD) (figure 1.5). The catalytic domain trimer harbors the CoA binding site. The CD forms trimers, which assemble either into the octahedral or dodecahedral cores (figure 1.5B). Core assembly is mediated by an amino acid sequence located at the C-terminus [20]. The PSBD, which binds E1 and E3 subunits, is connected to the CD by a alanine and proline rich flexible linker region. Figure 1.5C shows the crystal structures of the *G. stearothermophilus* E1 and E3 complexes bound by PSBD [70]. The E1 is bound by a single PSBD, which binds across the two-fold axis between two β-subunits. The E3 is also bound close to the two fold axis of the dimer [71]. The lipoyl domain is a small 10 kDa protein, which

shuttles between E1, E2, and E3 active sites and therefore mediates substrate channeling (figure 1.5A). The number of lipoyl domains can vary between different organisms. E2 of gram positive bacteria contain one LD, humans contain two and *E. coli*, for example, contains three LDs [18]. Figure 1.5A shows the *Geobacillus stearothermophilus* lipoyl domain structure solved by solution NMR [72]. It contains two antiparallel β-strands, which are connected by loop regions. One loop harbors a lysine residue which is post-translationally modified with lipoic acid. Residues of another loop region, here described as recognition loop, were shown to interact with the E1 directly. Deletion of the recognition loop inhibited the PDH complex [73]. Post-translational modification of the lipoyl domain is catalyzed by lipoate protein ligases and lipoyl transferases [74,75].

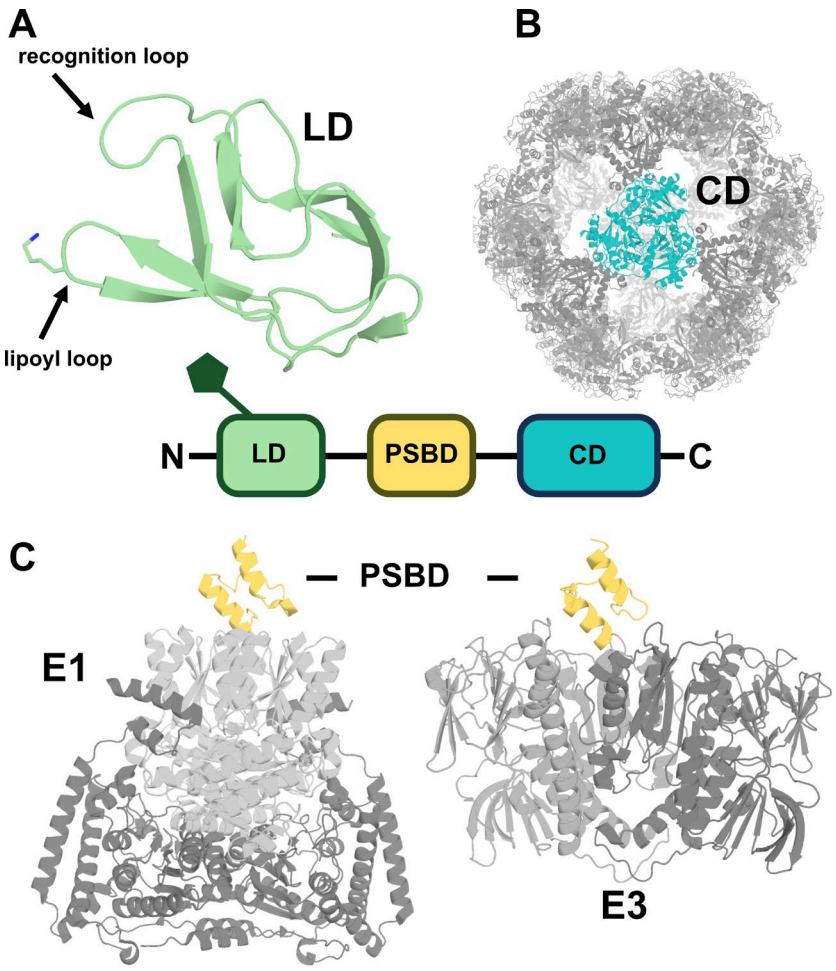

Figure 1.5: Domain architecture of the PDHc E2. The E2 consists of three domains: The N-terminal lipoyl domain (LD, green) is connected by a flexible linker to the peripheral subunit binding domain (PSBD, yellow). The PSBD is connected by another flexible linker to the C-terminal catalytic domain (CD, blue). The solution NMR structure of *G. stearothermophilus* LD is shown (PDB ID:1LAC). The lysine residue Lys42 is depicted, which is the site of post-translational modification with lipoic acid. One molecule of PSBD binds to one molecule E1 (PDB ID:1W85) or E3 (PDB ID:1EBD). The icosahedral core is shown, with one trimer colored in blue (PDB ID:1B5S).

1.5.1 Lipoic acid metabolism

Lipoic acid, initially termed pyruvate oxidation factor [76], is a sulfhydryl/disulfide containing coenzyme which has been isolated in 1951 from bovine liver extract [77,78]. It was named such as a consequence of its good solubility in organic solvents, poor solubility in water as well as its acidic properties. Today, α-lipoic acid is being used as treatment in patients with diabetic neuropathy due to its antioxidative properties [79]. Lipoic acid contains a dithiolane ring with a chirality center at C6. Only its R-(+)-enantiomer is present in nature (figure 1.6). α-lipoic acid is present in all three domains of live. In *E. coli*, *B. subtilis*, and humans, lipoic acid can be synthesized from an octanoyl moiety attached to a transfer protein, like the LD, or the H-protein of the glycine cleavage system.

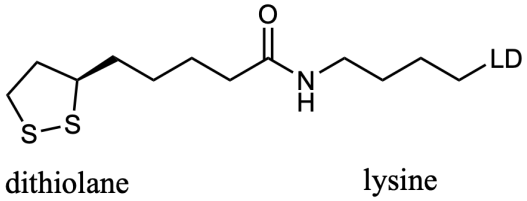

Figure 1.6: Post-translational modification of the LD by R-(+)-lipoic acid. Lipoic acid contains a dithiolane ring and a carboxyl group. The dithiolane ring is the reactive moiety. A lysine residue on the LD is post-translationally modified with lipoic acid, which results in the formation of a peptide bond.

The responsible lipoyl synthases are S-adenosylmethionine (SAM) dependent enzymes, which insert sulfur atoms at C6 and C8 positions [80]. Lipoyl transferases transfer the lipoyl group from the H-protein to the respective lipoyl domains [81]. In *E. coli* and *B. subtilis*, lipoic acid can also be attached to the LD in the scavenging pathway by lipoate protein ligases [74]. When attached to a lipoyl carrier protein, such as the LD, it functions as a "swinging arm", which transports reaction intermediates to the three active sites of the PDHc [19].

1.5.2 Catalytic mechanism of the E2

The catalytic domain of the E2 mediates acetyl transfer from S8-acetylated lipoamide to CoA, which yields acetyl-CoA and dihydrolipoamide [51]. Biochemical and structural studies revealed functional similarities with the chloramphenicol acetyl transferase, which catalyzes acetyl transfer from CoA to chloramphenicol [82,83]. Acetyl transfer is suggested to follow the same mechanism in the E2, where a thiolate is formed at CoA. The thiolate nucleophile then attacks the ketone carbon of the acetyl group. The resulting tetrahedral intermediate collapses into dihydrolipoamide and acetyl-CoA (figure 1.7). Several important residues have been identified by structural and biochemical studies.

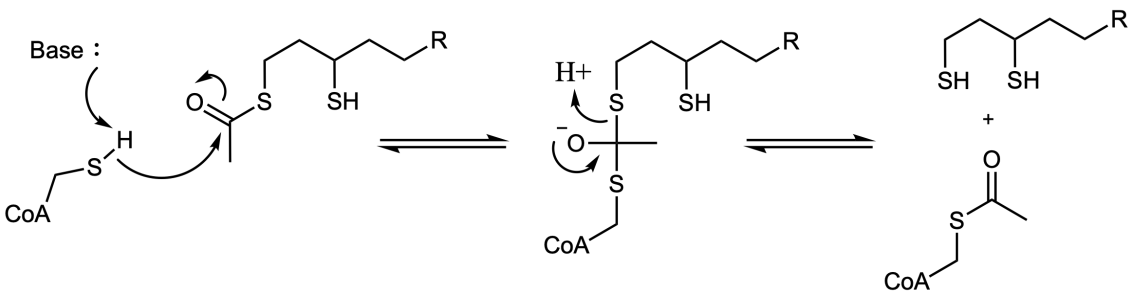

Figure 1.7: Reaction mechanism of acetyl transfer catalyzed by the E2. A base activates CoA by proton abstraction. The resulting thiolate carries out a nucleophilic attack at the ketone carbon of the acetyl group, which results in a tetrahedral intermediate between the lipoamide and CoA. The intermediate collapses and releases reduced lipoamide and acetyl-CoA.

The CD of *Acetobacter vinelandii* showed a catalytic histidine and aspartate pair, which activates CoA for nucleophilic attack [84]. Site-directed mutagenesis also revealed an important serine residue in the *E. coli* E2CD [85]. A synchronized gating mechanism was discovered in the cubic bovine BCDHc E2 core, where CoA binding opened the entrance to the lipoamide channel [86]. It is unclear, whether a similar mechanism is present in icosahedral E2 cores. After acetyl-transfer to CoA, dihydrolipoamide is formed. Dihydrolipoamide is re-oxidized in the E3 before the next reaction cycle.

1.6 The PDH E3 - Dihydrolipoyl dehydrogenase

The E3 is shared among all 2-oxo acid dehydrogenase complexes and the glycine cleavage system. The E3 forms a homodimer with a size of 100 kDa and belongs to a class of flavin-dependent proteins which catalyze the re-oxidation of the lipoyl group under production of NADH [17]. Several structures of dihydrolipoamide dehydrogenases have been elucidated in the recent years, including *E. coli*, *Mycobacterium tuberculosis* and human E3 [87-89]. Figure 1.8 shows the structure of the human PDH E3 dimer bound by FAD and NADH (PDB ID: 1ZMD). Each dimer contains a FAD and NADH binding domain. The active site contains a redox active disulfide bridge formed by two cysteine residues, which are in proximity to the isoalloxazine ring of FAD (figure 1.8B). The postulated reaction mechanism is similar to other FAD dependent reductases (figure 1.9) [90,91]. The reduced lipoyl group forms a mixed disulfide with one of the catalytic cysteines. The electrons are transferred to yield a thiolate anion, which forms a covalent adduct with FAD [91]. Oxidized lipoamide leaves the active site. Electrons are transferred to FAD to yield $FADH_2$. $FADH_2$ reduces NAD^+ to NADH, which completes the reaction cycle. Although multiple crystal structures of the E3 enzyme have been elucidated, no information of the position and interaction of the lipoamide with the E3 has been reported so far.

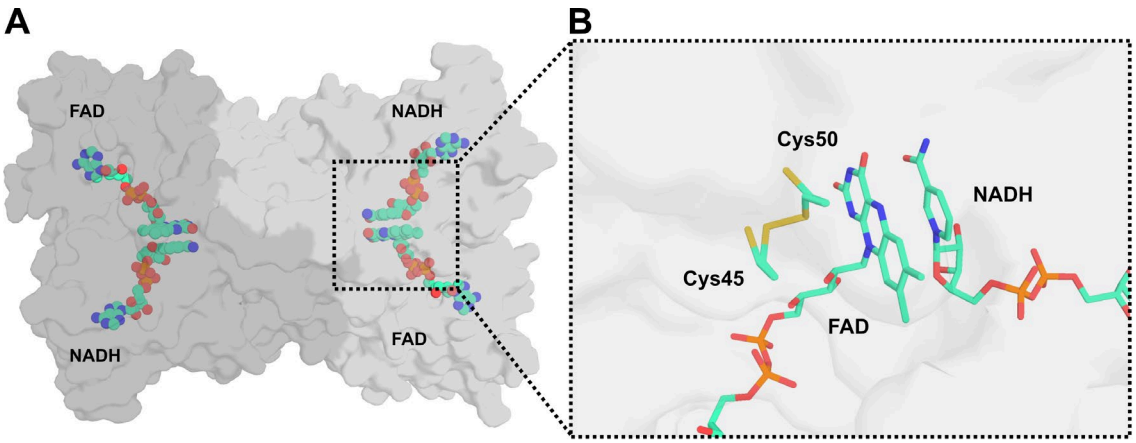

Figure 1.8: Cartoon representation of the human PDHc E3 bound by FAD and NAD. A) Human PDHc E3 is a homodimer. Each monomer contains a FAD and NAD+ binding site (PDB ID: 1ZMD). B) The active site of the E3 shows the nicotinamide ring of NADH stacked against the isoalloxazine ring system of FAD. Cys45 and Cys50 form the catalytic disulfide.

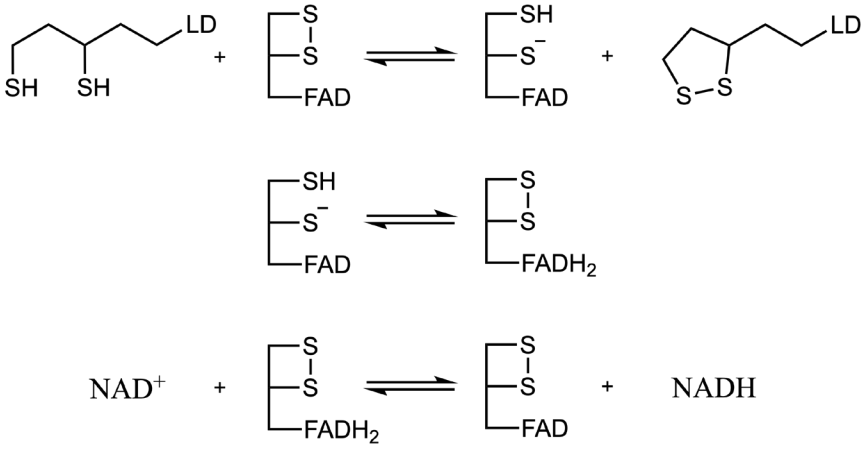

Figure 1.9: A simplified reaction mechanism of the dihydrolipoyl dehydrogenase. The reduced lipoamide is oxidized by thiolate-disulfide exchange with the active site disulfide, which results in the release of the oxidized lipoamide and formation of a thiolate anion in the active site. The thiolate anion reduces FAD to $FADH_2$, which regenerates the disulfide. $FADH_2$ reduces NAD^+ to NADH.

The pyruvate dehydrogenase plays an universally important metabolic role in most organisms connecting glycolysis, the citric acid cycle and fatty acid anabolism. As protein structure dictates function [92-94], there is a need for high-resolution structural data of the full complex and its individual subunits to elucidate their substrate interactions and reaction intermediates. The following section will highlight structural tools to elucidate enzymatic reaction mechanisms.

1.7 Structural tools to study the pyruvate dehydrogenase complex

The first protein structure, sperm whale myoglobin, was elucidated by Kendrew in 1958 via X-ray crystallography [95]. Today, structural biologists have many techniques at hand to elucidate the three-dimensional structure of protein molecules. Solution nuclear magnetic resonance (NMR) is one method, which relies on the quantum mechanical property of nuclear spins to derive protein structure and dynamics. However, NMR is usually limited to proteins smaller than 35 kDa [96]. Single particle cryo-EM is another method to elucidate protein structures. A thin frozen protein layer is shot by electrons and the resulting images are used to reconstruct the three-dimensional structure of the protein. Recently, first atomic resolutions have been achieved by cryo-EM [97]. High-resolution structures obtained by cryo-EM, however, are currently limited to highly symmetric, rigid particles such as apoferritin. X-ray protein crystallography, which relies on the diffraction of photons by electrons inside a crystal, is a reliable tool to determine protein structures at high resolution. While protein crystallization certainly is a major bottleneck of X-ray crystallography, careful biochemical treatment, and data collection can elucidate structural details of even large macromolecular protein complexes bigger than 750 kDa, such as the proteasome or the fatty acid synthase [98-100].

1.7.1 X-ray crystallography in enzymology

X-ray crystallography is based on the diffraction of X-ray photons by the electrons of protein molecules inside the crystalline lattice, which results in a diffraction pattern. Structure factors enable the computation of the electron density of the protein atoms. The structure factor amplitudes can be determined from the intensity of reflections of the measured diffraction patterns. The corresponding phases of the reflections are missing. However, they can be recovered from homologous protein models or experimental phasing techniques. Biochemical and technical advancements have led to the elucidation of many crystal structures over the last 60 years. Some of the recent improvements include high brilliance third generation synchrotron sources, with a fourth generation source with even higher brilliance being underway [101]. Other improvements are monochromatic collimated beams with a top-hat beam profiles at synchrotron beamlines, such as PETRA III, P14 at DESY, Hamburg. New CdTe detectors offer higher quantum efficiency at energies up to 100 keV. Crystallization facilities offer high-throughput crystallization screening, and therefore help overcome the bottleneck of crystallography, that is the growth of diffraction quality crystals [102].

1.7.2 Populating reaction intermediates *in crystallo*

In protein crystallography, protein molecules are confined to a crystalline lattice, but enzymes and proteins are still functionally active *in crystallo* [103]. It has been shown, that the crystal structure is (close to) identical to its structure in solution [104,105]. This enables the observation of ground states and reaction intermediates inside the crystal. One drawback is the potential restriction of large movements in the crystalline lattice. However, sometimes even large movements can be observed due to rearrangement of molecules in the crystal [106]. Furthermore, lattice constraints might help isolate protein conformations, which are less populated in solution [107]. X-ray crystallography provides a snapshot of a molecule, which is an average of all the molecules inside the crystal. Therefore, reaction intermediates need to be populated to be observed. To understand the reaction mechanism of enzymes, observation of just the ground state is not sufficient, but multiple intermediates along the reaction path need to be visualized. The following section will show, how conventional cryo-crystallography has been applied to trap and isolate enzymatic reaction intermediates.

1.7.2.1 Cryo trapping

The “average” enzyme catalyzes one reaction per 100 ms [108]. Protein crystals can be frozen at different timepoints during the enzymatic reaction to capture reaction intermediates. However, reaction intermediates are typically short-lived. Should the reaction be too fast to be captured by manual flash freezing, the reaction can be slowed down by lowering the reaction temperature. Lowering the temperature below the glass transition temperature in crystals soaked with mixed solvents like methanol trapped an enzyme-substrate complex of lysozyme [109]. Recent advances have decreased the flash-freezing time in a cryo-trapping experiment. For example, an automatic and fast robotic plunger has been developed, which has helped elucidate reaction intermediates and conformational changes in the tryptophane synthase [110]. The population of reaction intermediates can also be manipulated by changing other parameters, like the pH, especially if the reaction is facilitated by general acid-base catalysis [111].

1.7.2.2 Protein mutagenesis

Apart from modifying reaction parameters, the amino acid composition of the protein can be changed to slow or inhibit the enzyme. Often times catalytic residues are substituted by site-directed mutagenesis to trap enzyme-substrate complexes and reaction intermediates. For example, site directed mutagenesis of a catalytic serine residue was a successful strategy to trap tetrahedral intermediates in the alkaline phosphatase, and a phenylalanine to

tryptophane substitution in the active site lead to accumulation of an pre-decarboxylation intermediate in the pyruvate oxidase of *L. plantarum* [112,113].

1.7.2.3 Substrate and cofactor analogues

Native enzymes soaked with substrate or cofactor analogues provide valuable structural information. Often times, inhibitors mimic enzymatic intermediate or transition states. For example, substrate analogues with poor leaving groups can slow the reaction down enough to be observed as Michaelis complex in the crystal [114]. Base analogues were used to trap covalent intermediates in the tRNA guanine trans-glycosylase [115]. In addition, ThDP analogues were soaked into a variety of thiamine dependent enzymes and trapped pre-reaction and Michaelis complexes [32,116].

1.7.3 Time-resolved crystallography

Conventional cryo-crystallography obtains a comparatively static image of a dynamic molecule. Careful manipulation of enzyme, and reaction parameters can increase the live span of reaction intermediates, but the ultimate goal is to follow the enzyme as close to its native state possible, without altering catalytic residues, or utilizing unnatural temperatures and without the use of artificial substrates/cofactor analogues. To capture multiple snapshots in the course of a reaction, time-resolved crystallography (TRX) has emerged as a powerful technique. In TRX, usually crystals of wild-type protein and natural substrates are employed at room temperature under natural reaction conditions to mimic the native reaction as close as possible. Laue diffraction was employed first, which offers a short exposure time in the ps range. Laue diffraction utilizes a polychromatic X-ray beam, which samples the crystalline lattice of a single crystal in one shot without oscillation of the crystal [117]. Theoretically, one polychromatic exposure is sufficient to solve the crystal structure, but the use of polychromatic wavelengths makes indexing of the reflections more difficult, the energetic polychromatic beam might lead to radiation damage and the method is sensitive to crystal disorder [118,119]. As a consequence, serial X-ray crystallography has become more widely adopted. In serial X-ray crystallography, the protein structure is solved by exposing many, randomly oriented micro-crystals to an X-ray beam. Micro- and nano-crystals offer access to faster diffusion times than conventional crystals and the possibility for homogeneous activation by optical triggers [120,121]. Each micro-crystal is generally only exposed once or twice. XFEL sources present the most extreme case, where crystals diffract once before they are destroyed by the intense X-ray beam (diffraction before destruction principle) [122]. XFELs enable temporal resolutions in the femtosecond range, while serial synchrotron crystallography (SSX) offers time resolutions in the ps or ms range using

polychromatic or monochromatic radiation, respectively. Time-resolutions obtained in XFEL experiments cover early steps of the reaction such as bond breaking or side-chain rotations. SSX experiments cover slower processes in the µs-s range such as allosteric regulation, conformational transitions, protein breathing motions, ligand binding and domain movements [121,123–125]. Figure 1.10 illustrates a typical pump-probe setup in a time-resolved experiment. The reaction is first initiated by a pump, for example a laser, which is followed by a probe (X-ray) after a specific time delay.

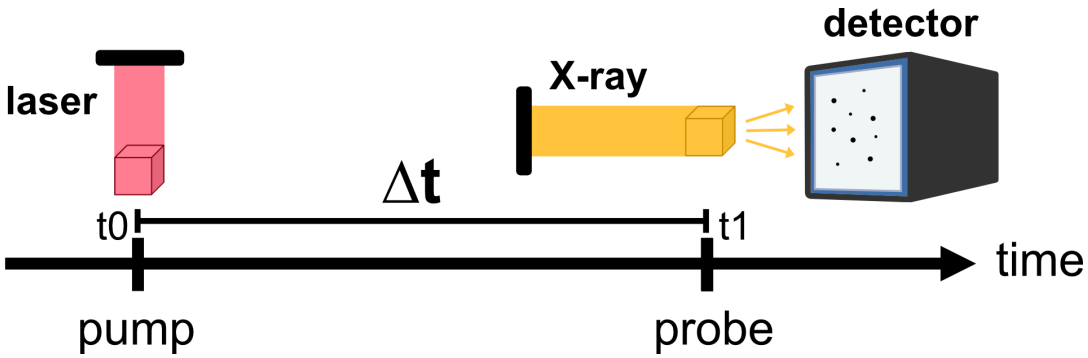

Figure 1.10: The pump-probe setup. A schematic of a typical pump-probe setup for time-resolved crystallography is shown. Reactions are initiated at t0 by a pump, for example a laser. After a specific time delay Δt the reaction is probed by the X-ray.

1.7.3.1 Sample application for serial crystallography

Several sample delivery methods for microcrystals have been applied successfully at synchrotron beamlines. One method is the tape-drive approach. A drop microcrystal suspension is applied on a tape, which is then translated through the X-ray beam [126]. Another method is the use of liquid jets, which were first employed at XFEL sources. A continuous stream of nano or microcrystals are delivered to the X-ray beam through a small capillary. This method consumes a lot of protein. Lipidic cubic phase (LPC) injectors were employed to reduce sample consumption due to a slower flow speed [127,128]. A system, which requires less sample than liquid jet approaches, are fixed-target delivery systems, such as silicon chips. These chips contain several thousand compartments. Microcrystals are applied to these compartments and raster-scanned through the X-ray beam [129,130]. For most sample delivery methods, reaction initiation by optical triggers or rapid mixing are possible. One exception is LCP, where rapid-mixing is not feasible due to the viscous media.

1.7.3.2 Reaction initiation

Synchronous reaction initiation for all molecules inside the crystal is crucial for SSX experiments, since structure factors are influenced by all atoms in the crystal. The reaction can

either be initiated by optical triggers, such as lasers, or rapid-mixing of a substrate solution. Naturally photosensitive proteins have been used for TRX experiments using optical activation [127,131,132]. However, less than 0.5 % of proteins are photosensitive [125]. Substrate or protein can be made photosensitive by attachment of a photolabile group (photocage). The photocage either inactivates the substrate or enzyme, and cleavage of the group results in catalysis. Caged compounds can be soaked into the crystals to either occupy the solvent channels or bind non-productively to the active site. Examples of photocages used in time-resolved studies of macromolecules are para-hydroxyphenyl, caged nitric oxide and nitrobenzyl compounds [130,133,134]. The right photocage needs to be chosen carefully, depending on its chemical and physical properties, such as solubility, cleavage rate, absorption wavelength, extinction coefficient and quantum yield. The decaging time varies depending on the chemical group and ranges from ns to ms [125]. Initiation by rapid-mixing is feasible, if the catalytic rate of the studied enzyme is slower than the diffusion time of its substrate into the crystal. The diffusion time of a substrate depends on its diffusion coefficient, concentration, crystal volume, and crystal surface [135]. The diffusion time for microcrystals usually lies in the low ms range. In contrast, diffusion takes several seconds in larger crystals [136]. That is why microcrystals are preferred in time-resolved experiments that rely on reaction initiation via diffusion.

1.7.3.3 SSX experiments at P14 of beamline PETRA III, DESY

The T-REXX endstation (P14.EH2, PETRA III, DESY, Hamburg), is the world's first dedicated endstation for SSX experiments [137]. Its X-ray beam is refocused by compound refractive lenses (CRLs) to provide a 15x10 μm^2 beam with a flux of $2x10^{12}$ photons per s at energies of 12.7 keV. The endstation offers a fixed target sample delivery setup for time-resolved crystallography utilizing silicon photochips containing 25,600 compartments. A crystal suspension can be pipetted onto the silicon chip and crystals are sucked into the compartments by brief vacuum application. The reaction can be initiated either by an optical trigger (355 nm laser) or by the liquid application method (LAMA). LAMA utilizes a piezo-driven droplet injector, which shoots a small 75 pl droplet of substrate solution at the crystals [136]. A statistical approach called hit and return (HARE) system decreases the time of the experiment. In HARE, the chip translation time determines the time delay of the time-resolved experiment. The HARE approach allows time resolutions from ms to s and therefore allows tracking of slower reactions using longer delay times, which would take much longer to achieve without the HARE approach [130].

1.8 Aims of the thesis

The pyruvate dehydrogenase complex (PDHc) is one of the largest macromolecular enzyme complexes and serves an universally important metabolic function by converting pyruvate into acetyl-CoA. Acetyl-CoA can either enter the citric acid cycle to generate reducing equivalents for oxidative phosphorylation, or be used as starting point in fatty acid synthesis. Hence, the PDHc links glycolysis, the citric acid cycle, and fatty acid anabolism. This large protein complex plays an important role in most organisms and humans. PDHc malfunction in humans leads to neurological and lethal complications [14,15]. The PDHc is furthermore involved in type 2 diabetes, and could also be a potential antibiotics target [16]. The protein complex consists of three different enzymes E1, E2, and E3, which catalyze pyruvate decarboxylation, acetyl transfer and re-oxidation of the lipoyl moiety, sequentially. Substrates are channeled between different reaction centers via a small flexible domain, called lipoyl domain. The PDHc E1 of gram-positive bacteria and humans is a 155 kDa thiamine diphosphate dependent heterotetrametric protein containing two active sites, which decarboxylate pyruvate. As do most thiamine diphosphate dependent enzymes, the E1 displays half-of-the-sites reactivity [59]. The PDHc has been subject to research for over 60 years, but several aspects of catalysis and protein interactions are not well understood. For example, detailed structural information about the interaction between the lipoyl domain and E1, E2, and E3 enzymes remains elusive. The structural basis for the half-of-the-sites reactivity of the E1 is still not fully understood. The decarboxylation reaction of the E1 has been analyzed extensively by spectroscopic methods, but intermediates of the decarboxylation reaction have not been observed by structural methods.

Time-resolved crystallography was adapted as a powerful technique to study natural reactions inside a crystal. TRX experiments have often been conducted on model enzymes, such as lysozyme, proteinase K or xylose isomerase. One aim of this thesis was to elucidate reaction intermediates of a more complex enzyme system at the new endstation for serial synchrotron crystallography in Hamburg. The PDH E1 of the model organism *Bacillus subtilis* was chosen for these experiments. The *B. subtilis* PDHc is similar to the human PDHc in terms of its overall icosahedral core and subunit architecture. Insights into pitfalls that arise during crystallization of microcrystals, sample application, reaction initiation and data collection should be gathered.

Several crystal structures of the E1, for example from human and *E. coli* sources, were elucidated so far. However, resolutions have so far been limited to 1.8-2.0 Å [42,61]. Therefore, another aim of this thesis was to elucidate high resolution structures of the *B. subtilis* PDH E1 using classical cryo X-ray cryo-crystallography. High resolution structures of the E1 should help elucidate the underlying inhibition mechanism of known E1 inhibitors such as fluoropyruvate and methyl acetyl phosphonate. Furthermore, high resolution information

of enzyme intermediates might complement data obtained by serial crystallography and help to elucidate the structural basis of half-of-the-sites reactivity of the E1 enzyme. Soaks with substrate of related 2-oxoacid dehydrogenase complexes should offer insights into the substrate specificity of the PDH E1.

The bovine BCDH E2 exhibits a gating mechanism, which regulates CoA and lipoamide binding [86]. A high resolution structure of the E2 catalytic domain of *B. subtilis* should decipher, whether a similar mechanisms is present in icosahedral E2 cores. Structural information of interactions of the lipoyl domain with the E1 or E3 have not yet been elucidated. The lipoamide has been observed in the E2 active site in a few crystal and cryo-EM structures, but either showed very low occupancies or low resolutions (2.6 Å – 4.4 Å) (PDB IDs: 7B9K, 6ZZK, 1EAE) [138]–[140]. There are several reasons for the absence of detailed structural information of this crucial prosthetic group. Firstly, it is naturally attached to the LD of 2-oxoacid complexes. Structures of E1-LD/E3-LD have so far evaded elucidation due to the inherent weak affinity of LD towards E1/E3 [141]. Secondly, free lipoamide is a very poor substrate for the E1 [142]. Thirdly, it is poorly soluble in polar crystallization conditions, which impedes soaks at higher lipoamide concentrations to overcome its poor affinity. Fourthly, there simply is a lack of E2CD crystals diffracting to high resolution. Therefore, strategies should be devised to trap lipoamide-E2 and lipoamide-E3 enzyme substrate complexes at high resolution.

2 Materials and Methods

2.1 Materials

2.1.1 Buffers and solutions

Buffer	Concentration	Content
Coomassie Destaining Solution	25% (v/v)	Isopropanol
	10% (v/v)	Acetic Acid
Coomassie Staining Solution	0.05% (w/v)	Coomassie G-250
	0.1% (w/v)	Coomassie R-250
	25% (v/v)	Isopropanol
	10% (v/v)	Acetic acid
DNA Loading Dye (6x)	30% (v/v)	Glycerol
	0.25% (w/v)	Bromophenol Blue
	0.25% (w/v)	Xylene Cyanol FF
E1 Buffer A	0.05 M	Imidazole pH 7.2
	0.1 M	KCl
	0.01 M	$MgCl_2$
	0.003 M	TCEP
E1 Buffer B	0.05 M	Imidazole pH 7.2
	1 M	KCl
	0.01 M	$MgCl_2$
	0.003 M	TCEP
E1 Cryo Solution A	0.1 M	Tris pH 8.0
	0.2 M	$MgCl_2$
	16% (w/v)	PEG 3350
	5/10/15/20% (v/v)	Ethylene glycol
	0.2 mM	ThDP
E1 Cryo Solution B	0.1 M	MMT pH 5.0
	0.2 M	$MgCl_2$
	16% (w/v)	PEG 3350
	5/10/15/20% (v/v)	Ethylene glycol
	0.2 mM	ThDP
E1 Elution Buffer	0.05 M	HEPES pH 7.2
	0.3 M	NaCl
	0.5 M	Imidazole
	0.01 M	$MgCl_2$
	0.05 M	KCl
	0.005 M	β-Mercaptoethanol

E1 Lysis Buffer	0.05 M	HEPES pH 7.2
	0.5 M	NaCl
	0.01 M	Imidazole
	0.01 M	$MgCl_2$
	0.05 M	$AmSO_4$
	0.005 M	β-Mercaptoethanol
E1 Stabilization Buffer	0.1 M	MMT pH 5.0
	0.2 M	$MgCl_2$
	16% (w/v)	PEG 3350
	5% (v/v)	Ethylene glycol
	0.2 mM	ThDP
E1-NB GF Buffer	0.05 M	Imidazole pH 6.8
	0.3 M	KCl
	0.01 M	$MgCl_2$
	0.003 M	TCEP
E2 Cryo Solution IA	0.1 M	Sodium citrate pH 5.2
	1.3 M	Ammonium sulfate
	1% (w/v)	PEG 400
	5/15/25% (v/v)	Ethylene glycol
E2 Cryo Solution IB	0.1 M	Sodium citrate pH 5.2
	1.3 M	Ammonium sulfate
	1% (w/v)	PEG 400
	5/15/25% (v/v)	Glycerol
E2 Cryo Solution II	0.1 M	Tris pH 8.0
	0.2 M	$CaCl_2$
	5% (v/v)	Isopropanol
	17% (w/v)	PEG 4000
	5/15 % (v/v)	Ethylene glycol
E2 Elution Buffer	0.05 M	Tris pH 7.2
	0.25 M	NaCl
	0.05 M	KCl
	0.5 M	Imidazole
	0.005 M	β-Mercaptoethanol
E2 GF Buffer	0.05 M	Tris pH 7.2
	0.1 M	NaCl
	0.1 M	KCl
	0.005 M	DTT
E2 Lysis Buffer	0.05 M	Tris pH 7.2
	0.5 M	NaCl
	0.01 M	Imidazole
	0.005 M	β-Mercaptoethanol

E2 Wash Buffer	0.05 M	Tris pH 7.2
	0.5 M	NaCl
	0.02 M	Imidazole
	0.005 M	β-Mercaptoethanol
E3 Cryo Solution	0.05 M	Imidazole malate pH 8.5
	2.2 M	Ammonium sulfate
	5/10/20 % (v/v)	Glycerol
ISO-Buffer (5x)	0.5 M	Tris pH 7.5
	0.05 M	$MgCl_2$
	1 mM	dNTPs
	0.05 M	DTT
	0.03 M	PEG 8000
	5 mM	NAD^+
Microcrystal Cryo Solution	0.1 M	Tris pH 8.0
	0.2 M	$MgCl_2$
	17 %(w/v)	PEG 3350
	25 % (v/v)	Ethylene glycol
MMT Buffer (10x) [143]	2.68 g	L-malic acid
	7.81 g	MES
	5.22 g	Tris (Adjust pH with 10M NaOH to 9.0 or 10M HCl to 4.0 in 0.1 l ddH_2O)
NB Elution Buffer	0.05 M	Tris pH 7.2
	0.5 M	Imidazole
	0.2 M	NaCl
	0.005 M	β-Mercaptoethanol
NB GF Buffer	0.05 M	Tris pH 7.2
	0.2 M	NaCl
	0.005 M	$MgCl_2$
	0.004 M	DTT
NB Lysis Buffer	0.05 M	Tris pH 7.2
	0.01 M	Imidazole
	0.5 M	NaCl
	0.003 M	β-Mercaptoethanol
SDS Loading Buffer (6x)	0.375 M	Tris pH 6.8
	60% (w/v)	Glycerol
	0.6% (w/v)	SDS
	0.65 M	DTT
	0.1% (w/v)	Bromophenol blue

SDS PAGE Running Buffer (10x)	0.25 M	Tris pH 8.3
	1.92 M	Glycine
	1% (w/v)	SDS
TAE Buffer	0.04 M	Tris pH 8.0
	0.02 M	Acetic acid
	1 mM	EDTA

2.1.2 Media and Agar

Medium	Amount	Content
LB Agar	15 g	Agar Agar
	100 mg	Ampicillin
	1 l	LB medium
LB Medium	10 g	Tryptone
	5 g	Yeast extract
	5 g	NaCl
		In 1l of ddH_2O
TB Medium	12 g	Tryptone
	24 g	Yeast extract
	9.4 g	K_2HPO_4
	2.2 g	KH_2PO_4
	4 ml	Glycerol
		In 1 l of ddH_2O

2.1.3 Chemicals

Chemicals	Supplier
2-oxoglutarate	Sigma-Aldrich
3-Methyl-2-oxovaleric acid sodium salt	Sigma-Aldrich
Acetic acid	Merck
Agar Agar	Roth
Agarose	SERVA
Ammonia	Sigma-Aldrich
Ammonium sulfate	Merck
Ampicillin	Sigma-Aldrich
Bradford Assay reagent	Bio-Rad
Bromophenol Blue sodium salt	SERVA
Calcium chloride	Merck
Citric acid	Sigma-Aldrich

Coenzyme A (CoA)	Applichem
Coomassie Brilliant Blue G-250	Merck
Coomassie Brilliant Blue R-250	Bio-Rad
Deoxynucleoside triphosphates (dNTPs)	NEB
Di-Potassium hydrogen phosphate	Merck
Dihydrogen potassium phosphate	Merck
Dithiothreitol (DTT)	Roth
DNA stain G	SERVA
Ethylene glycol	Sigma-Aldrich
Ethylenediaminetetraacetic acid (EDTA)	Merck
Fluoropyruvic acid sodium salt	Sigma-Aldrich
Glucose	Merck
Glycerol	Merck
HEPES	Sigma-Aldrich
Hydrochloric acid (HCl)	Merck
Imidazole	Sigma-Aldrich
Isopropanol	Merck
Isopropyl β-D-1-thiogalactopyranoside (IPTG)	Sigma-Aldrich
L-Malic acid	Sigma-Aldrich
Lipoamide-dPEG(4)-OMe	Iris Biotech
Lysogeny broth medium (LB)	Bioworld
Magnesium chloride ($MgCl_2$)	Merck
MES hydrate	Sigma-Aldrich
Methyl acetyl phosphonate (MAP)	Synthesized by Dr. Belov (MPINAT)
Paraffin oil	Hampton Research
Phenyl methane sulfonyl fluoride (PMSF)	Sigma-Aldrich
Polyethylene glycol (PEG) 3350	Sigma Aldrich
Polyethylene glycol 400	Sigma-Aldrich
Polyethylene glycol 4000	Sigma-Aldrich
Potassium chloride (KCl)	Merck
Sodium 4-methyl-2-oxovalerate	Sigma-Aldrich
Sodium chloride (NaCl)	Merck
Sodium citrate tribasic	Sigma-Aldrich
Sodium pyruvate	Applichem
Sucrose	Merck
Terrific broth medium (TB)	Melford
Thiamine diphosphate	Applichem
Tris(2-carboxyethyl)phosphine hydro-chloride (TCEP)	UBPBio
Tris(hydroxymethyl)aminomethane (Tris)	VWR
Tryptone	Roth
Yeast extract	Roth

β-Mercapto Ethanol	Sigma-Aldrich

2.1.4 Consumables

Consumables	Supplier
4-15 % Criterion™TGX™Gel	Bio-Rad
4-15 % Mini-PROTEAN® Gel	Bio-Rad
Amicon® Ultra-15 Centrifugal filter units	Merck
Amicon® Ultra-4 Centrifugal filter units	Merck
Any kD Criterion™TGX™Gel	Bio-Rad
Any kD Mini-PROTEAN® Gel	Bio-Rad
Cryschem M plate, 24-well	Hampton Research
Crystal Clear Sealing Tape	Jena Bioscience
Crystalgen Plate 24-well, pre-greased	Jena Bioscience
Falcon 15 ml	Sarstedt
Falcon 50 ml	Sarstedt
Glass fibre filter 47 mm	Hahnemühle
Ni-NTA Agarose Rapid Run	ABT
Nitrile gloves	Starlab
OMNIFIX® 20 ml syringe	B. Braun
Pipette tips 10 ml	Eppendorf
Pipette tips 20, 200, 1000 µl	Mettler Toledo
Reaction Tube 1.5 ml	Sarstedt
Reaction Tube 200 µl	Sarstedt
SDS-PAGE Running Buffer	Roth
Siliconized Glass Cover Slides	Hampton Research
Sterile 0.2 µm cellulose acetate filters	Sartorius
Sterile 0.45 µm hydrophilic filters	Sartorius
Polycarbonate Cover Slips	Molecular Dimensions
Spinal Needle	BD
Vapor batch plate	Douglas instruments

2.1.5 Kits and Standards

Kits and Standards	Supplier
1 kb DNA Ladder	NEB
NucleoSpin® Gel and PCR clean-up	Macherey-Nagel
NucleoSpin® Plasmid	Macherey-Nagel
Precision Plus Protein Unstained Standard	Bio-Rad

2.1.6 Enzymes

Enzymes	Supplier
DNaseI	Applichem
DpnI	NEB
Lysozyme (HEWL)	Thermo Fisher Scientific
Phusion High-Fidelity DNA Polymerase (+HF Buffer)	Thermo Fisher Scientific
T4 DNA ligase (+Buffer)	NEB
T4 polynucleotide kinase	NEB
T5 exonuclease	NEB
Taq ligase	NEB
TEV protease	Self-made

2.1.7 Bacterial strains

Bacterial strains	Supplier
BL21 (DE3) *Escherichia coli*	Invitrogen/Thermo Fisher Scientific
BL21 AI *Escherichia coli*	Invitrogen/Thermo Fisher Scientific
XL1blue *Escherichia coli*	Agilent

2.1.8 Plasmids and primers

Plasmids	Supplier
pET151-D-TOPO	Invitrogen/Thermo Fisher Scientific
pRSET A	Invitrogen/Thermo Fisher Scientific
Primers	**Sequence 5´-3´**
bsPDH E1 H128N Fw	CCGGAACTG**AAT**GCGGATAGCC
bsPDH E1 H128N Rv	TGTATGCACACCACCACCAAACG
bsPDH E1 H273N Fw	GTTATGGTCCG**AAT**ACAATGGCTGG
bsPDH E1 H273N Rv	GAAAGGTCAGGGTTTCAATCAGTGTC
bsPDH E2 202-433 trimer Fw	GTATTTTCAGGGAATTGATCCCTTCACCGCTGCAC-CGGCACCGGAAG
bsPDH E2 202-433 trimer Rv	CCTTCTCGAGTATATATACCTAGGTTATCAATTCAGC AGACGTTTAATATGATTCAGTGCATTC
pET151 linearization Fw	TGATAACCTAGGTATATATACTCGAGAAGG
pET151 linearization Rv	GGTGAAGGGATCAATTCCCTGAAAATAC
bsPDH E3 C52S Fw	CTGAATGTTGGT**AGC**ATTCCGAGC
bsPDH E3 C52S Rv	ACAAACACCACCTAAGGTTGCTTTTTCAAC

2.1.9 Software

Software	Source
AIMLESS [144]	https://www.ccp4.ac.uk/html/aimless.html
Affinity Designer	https://affinity.serif.com/de/designer/
AutoPROC [145]	https://www.globalphasing.com/autoproc/
Benchling	https://benchling.com/
BioRender	https://biorender.com
Buster	https://www.globalphasing.com/buster/
CCP4 [146]	http://www.ccp4.ac.uk
ChemDraw	http://www.perkinelmer.de/category/chemdraw
Coot [147]	https://www2.mrc-lmb.cam.ac.uk/personal/pemsley/coot
CrystFEL [148]	http://www.desy.de/~twhite/crystfel/
Grade2	https://www.globalphasing.com/buster/manual/grade2/manual/
Inkscape	https://inkscape.org
JLigand [149]	http://www.ysbl.york.ac.uk/mxstat/JLigand/
Mendeley	https://www.mendeley.com/
Microsoft Office	https://www.office.com/?omkt=de-de
Origin Pro	https://www.originlab.com/origin
POINTLESS [150]	https://www.ccp4.ac.uk/html/pointless.html
ProtParam [151]	https://web.expasy.org/protparam/
PyMOL	https://www.pymol.org/2/
Refmac5 [152]	https://www2.mrc-lmb.cam.ac.uk/groups/murshudov/content/refmac/refmac.html
SnapGene	https://www.snapgene.com
Staraniso Server	https://staraniso.globalphasing.org/cgi-bin/staraniso.cgi
UCSF ChimeraX	https://www.cgl.ucsf.edu/chimerax/
XDS [153]	https://xds.mr.mpg.de

2.1.10 Equipment

Equipment	Manufacturer
Äkta Pure 25M	Cytiva
Balances	Sartorius
Centrifugal Evaporator Unit	Eppendorf
Centrifuge LYNX 6000	Thermo Scientific
Centrifuge Multifuge X1R	Thermo Fisher Scientific
Counting chamber	Roth
Criterion™ cell	Bio-Rad
Dewars	Taylor-Wharton
Electro Supplier Power Pac 3000	Bio-Rad
Electro Supplier Power Pac Basic	Bio-Rad
HiLoad Superdex 200 26/600	Cytiva
HiLoad Superdex 75 26/600	Cytiva
HiTrap Q HP Anion Exchange column	Cytiva
Incubator Eco-Line E100	RUMED
Incubator Multitron Pro	InforsHT
Incubator New Brunswick™ Innova® 44	Eppendorf
Magnetic Stirrer	Heidolph Instruments
Magnetic Wands	MiTeGen
Microloops	MiTeGen
Mili-Q®	Merck
Mini-PROTEAN® Tetrasystem	Bio-Rad
NanoDropOne	Thermo Fisher Scientific
Orbital Shaker RS-OS20	Phoenix Instrument
PCR System ProFlex	Thermo Fisher Scientific
PerfectBlue Gel System Mini S	PEQLAB
pH meter	inolab
pH Meter Inolab 7110	WTW
Photo scanner Epson perfection V800	Epson
Photometer Genesys 10S UV-Vis	Thermo Fisher Scientific
Pipettes	Rainin, Eppendorf
Rotor Fiberlite F35L	Thermo Fisher Scientific
Rotor Fiberlite F9	Thermo Fisher Scientific
SDS Gel shaker	Rettberg
Sonicator	Elma
Stereo microscopes M125	Leica
Superdex 200 10/300 Increase GL	Cytiva
Table top centrifuges	Thermo scientific
Thermomixer	Eppendorf
Ultra-Centrifuge Wx+ Sorvall	Thermo Fisher Scientific
UV-transilluminator	BioMetra

2.2 Methods

2.2.1 Molecular Biology

2.2.1.1 Polymerase Chain Reaction (PCR)

E1 and E3 point mutations were introduced by site-directed mutagenesis. The bases coding for the mutations were located in the middle of the forward primer (section 2.1.8, highlighted in bold). The entire plasmid was amplified by PCR following the pipetting scheme in table 1. 50 µl reactions were set up and stored on ice before initiating the reaction following the PCR program in table 2. The DNA region coding for the E2 trimers (E2CDΔ9) was amplified from a vector containing the full E2 subunit. The C-terminal nine aminoacids were deleted to inhibit icosahedral core assembly. Both forward and reverse primers contained two segments, a 3´ region annealing to the E2 sequence, and a 5´ region matching the target vector sequence (underlined), to allow cloning by Gibson Assembly (chapter 2.2.1.5) [154].

Table 1: PCR pipetting scheme

Component	Volume [µl]	Concentration
Template DNA	1	100 pg/µl
dNTPs	1.2	240 µM
Phusion DNA Polymerase	0.5	0.02 U/µl
Forward primer	1.5	0.3 µM
Reverse primer	1.5	0.3 µM
5x HF buffer	10	1x
ddH_2O	34.3	

Table 2: PCR program

Temperature [°C]	Time	Number of cycles
98	30 s	1x
98	20 s	
55	30 s	25x
72	30s / kb	
72	10 min	1x

2.2.1.2 Agarose Gel Electrophoresis

PCR products were analyzed by DNA gel electrophoresis. 20 µl of a 6x DNA Loading Dye was added to 100 µl of PCR product and the samples were run on a 1 % (w/v) agarose gel in TAE Buffer. 0.75 µl of DNA stain G was added to 50 ml agarose to detect the DNA under ultraviolet (UV) light with an UV-transilluminator.

2.2.1.3 PCR purification

Gel regions containing the PCR product were excised with a scalpel. The PCR products were purified with the NucleoSpin® Gel and PCR Clean-up kit (Macherey-Nagel) following the manufacturer's instructions. The DNA was eluted from the columns with double-distilled water heated to 70 °C to improve the yield.

2.2.1.4 Measurement of DNA concentration

DNA concentrations were determined spectrophotometrically at 260 nm using a NanoDrop-One spectrophotometer.

2.2.1.5 Gibson Assembly

Gibson Assembly is a cloning method which allows the seamless ligation of multiple DNA fragments without the need for restriction enzymes [154]. The vector DNA was linearized following the PCR protocol described in 2.2.1.1. A 20 µl Gibson Assembly reaction was set up containing 100 ng of linearized vector DNA. The insert DNA was added in a 3:1 (insert:vector) molar ratio. 15 µl of an enzyme mix containing 1.25x ISO-Buffer, 80 U Taq ligase, 0.08 U T5 Exonuclease, 0.5 U Phusion polymerase, and 5 µg extreme thermostable single-stranded DNA binding protein (ET SSB), were added. The reaction was incubated for 1 h at 50 °C, and 5 µl of the reaction were then used to transform competent *E. coli* XL1blue cells (chapter 2.2.1.7).

2.2.1.6 DNA ligation

A 30 µl ligation reaction was set up containing 20-200 ng of linearized plasmid DNA and 2 µl of CutSmart Buffer (NEB). Methylated DNA was removed by addition of 1 µl DpnI and incubation at 37 °C for 30 min. 3 µl T4 Ligase Buffer containing ATP and 1 µl of T4 polynucleotide kinase were added to phosphorylate the blunt ends. The reaction was incubated for 5 min at room temperature. Ligation was started by addition of 1 µl T4 ligase. The reaction was incubated for 1 h at room temperature and continued overnight at 18 °C. The ligated vectors were transformed in competent *Escherichia coli* XL1blue cells (chapter 2.2.1.7). Cells were selected on 2% (w/v) LB Agar plates containing Ampicillin.

2.2.1.7 Transformation of competent *E. coli* cells

100 µl of competent *E. coli* cells were thawed on ice for 20 min. 200 ng of plasmid DNA was added and the cells were incubated for 30 min on ice. The cells were heat-shocked at 42 °C for 90 s and 700 µl LB medium was added. The cells were incubated at 37 °C for one hour while shaking. The cells were used to inoculate an LB overnight culture supplemented with 1% (w/v) glucose and ampicillin for protein expression (see 2.2.3) or plasmid isolation (see 2.2.1.8).

2.2.1.8 Plasmid DNA isolation

E. coli Xl1blue cells were pelleted at 4000 g for 10 minutes. The plasmid DNA was isolated with the NucleoSpin® Plasmid kit (Macherey-Nagel) following the manufacturer's instructions. The DNA was eluted from the columns with double-distilled water heated to 70 °C to improve the yield.

2.2.1.9 DNA sequencing

Isolated plasmid DNA was Sanger-sequenced by Microsynth Seqlab, Göttingen. The DNA was prepared following the company´s instructions. Primers binding to the T7 promoter / T7 terminator region were chosen from the company´s standard primer library. The sequencing results were analyzed using the molecular biology online suite Benchling and the software SnapGene.

2.2.2 Protein concentration measurement

The protein concentration was determined spectrophotometrically by measuring UV absorbance of the protein at 280 nm in a NanoDropOne spectrophotometer. Extinction coefficients were calculated using the online tool ProtParam. Protein concentrations were calculated according to Beer-Lambert´s law,

$c = A/\varepsilon * b$

where A is the measured absorbance at 280 nm, c is the concentration and b is the path length in centimeter [155]. The protein concentration of E3 was determined by the Bradford method using bovine serum albumin (BSA) as protein standard.

Table 3: Protein size and extinction coefficients

	E1	**E1-NB**	**E2 CD**	**NB**
Extinction coefficients [$M^{-1}cm^{-1}$]	111620	162750	30035	25565
Size [kDa]	155.2	181.9	75.1	13.4

2.2.3 Protein expression

All protein expressions were performed in 2l baffled Erlenmeyer flasks while shaking at 180 rpm. TB medium was pre-warmed to 37 °C before inoculation. All media were autoclaved before use. After expression, the cells were harvested by centrifugation at 5000 g for 20 minutes at 4 °C and stored at -80 °C.

2.2.3.1 Expression of *B. subtilis* PDH E1 complex

The genes encoding for the *B. subtilis* PDH E1 α- and β-subunits (Uniprot: P21881, P21882) were located on a bicistronic pET-151-D/TOPO expression vector under control of a T7 promoter. The α-subunit was N-terminally fused to a hexa-histidine tag followed by a TEV protease cleavage site to allow purification via affinity chromatography and to remove the tag afterwards. Competent *E. coli* BL21 (DE3) cells were transformed with the expression plasmid. An overnight culture was grown at 37 °C in 100 ml Luria-Bertani (LB) medium supplemented with 1 % (w/v) glucose and 100 µg/ml ampicillin. 500 ml of prewarmed Terrific Broth (TB) medium supplemented with 1 % (w/v) glucose and ampicillin was inoculated to an OD of 0.05. The cells were grown to an OD of 0.8 at 37 °C at 180 rpm. The temperature was reduced to 18 °C and the expression was induced by addition of 1 mM isopropyl β-D-1-thiogalactopyranoside (IPTG). The protein was expressed for 20 h at 18 °C. The expression of mutant E1 proteins was performed following the same protocol.

2.2.3.2 Expression of *B. subtilis* PDH E2 CDΔ9 trimers

The gene encoding the *B. subtilis* PDH E2CDΔ9 with nine amino acids deleted from the C-terminus (202-433)(Uniprot:P21883) was located on an pET-151-D/TOPO expression vector under control of a T7 promoter. The CD was N-terminally fused to a hexa-histidine tag followed by a TEV cleavage site. The expression followed the same protocol as for the E1 (see 2.2.3.1), but 1 % (v/v) ethanol was added before reduction of the temperature to 18 °C. The cells were induced by addition of 0.5 mM IPTG and expressed for 20 h at 18 °C.

2.2.3.3 Expression of *Vicugna pacos* nanobody (NB)

Anti-PDH nanobodies were derived from alpacas immunized with the native *B. subtilis* PDH complex in the department of Dirk Görlich, MPINAT, Göttingen. The nanobodies were cloned by of Dr. Ai Woon Yee (former postdoc in our group) and Dr. Sabin Prajapati (group of Kai Tittmann, University of Göttingen). The gene encoding the *V. pacos* nanobody NB was located on an expression vector under control of a lac promoter. The NB was N-terminally fused to a 14xhistidine-NEDD8 tag, which allows for tag removal by the Nedp1 protease. The plasmid was transformed into competent BL21-AI cells and grown overnight

at 37 °C in LB supplemented with 3 % glucose and kanamycin. TB medium containing 0.1 % glucose was inoculated to an OD of 0.075 and the cells were grown to an OD of 0.8 at 37 °C. 1 % ethanol was added and the temperature was reduced to 18 °C. The expression was induced by addition of 0.5 mM IPTG and the cells were grown for 20 h at 18 °C.

2.2.3.4 Expression of *B. subtilis* PDH E3 dimer

The gene encoding for the *B. subtilis* E3 (Uniprot: P21882) was located on a pET-151-D/TOPO expression vector under control of a T7 promoter. The E3 was N-terminally fused to a hexa-histidine tag followed by a TEV protease cleavage site to allow purification via affinity chromatography and to remove the tag afterwards. Competent *E. coli* BL21 (DE3) cells were transformed with the expression vector. An overnight culture was grown at 37 °C in 100 ml Luria-Bertani (LB) medium supplemented with 1 % (w/v) glucose and 100 µg/ml ampicillin. 500 ml of pre-warmed Terrific Broth (TB) medium supplemented with 1 % (w/v) glucose and ampicillin was inoculated to an OD of 0.05. The cells were grown to an OD of 0.6 at 37 °C at 180 rpm. The temperature was reduced to 18 °C and 0.5 mM riboflavin was added. The expression was induced by addition of 0.5 mM IPTG. The protein was expressed for 20 h at 18 °C. The expression of $E3_{C52S}$ was performed following the same protocol.

2.2.4 Protein purification

The protocol “Cell lysis and Ni-NTA chromatography” (chapter 2.2.4.1) is included in the first steps of all purifications. All Buffers were filtered through 0.2 µm sterile filters, de-gassed, and stored at 4 °C before use.

2.2.4.1 Cell lysis and Ni-NTA chromatography

The cells were resuspended in 7.5 ml/g cells Lysis Buffer (pre-cooled to 4 °C) for 20 minutes. 1 mM PMSF, 0.5 mg/ml hen egg white lysozyme and a spatula tip of DNaseI were added. The cells were lysed via sonication with 10 x 60 s on/off cycles. The lysate was cleared for 1 h at 100,000 g. The supernatant was filtered through a 47 mm glass fiber filter and subjected to purification via a nickel-nitrilotriacetic acid (Ni-NTA) gravity flow chromatography column. The lysate was loaded two times the Ni-NTA column equilibrated in Lysis Buffer. The column was washed four times with 2.5 column volume (CV) Lysis Buffer. The protein was eluted in three fractions with 2.5 CV Elution Buffer each. 2 mM EDTA was added to the elution fractions to complex nickel ions. Fractions containing the protein of interest were analyzed via SDS-PAGE (chapter 2.2.5).

2.2.4.2 Purification of the *B. subtilis* PDH E1 complex

The E1 was purified via Ni-NTA chromatography (chapter 2.2.4.1). Tobacco Etch Virus (TEV) protease was added in a 1:200 (w/w) ratio to remove the histidine tag. 3 mM TCEP and 0.2 mM ThDP were added, and the protein was dialyzed against E1 Dialysis Buffer overnight at 4 °C. The protein was further purified by a 5 ml HiTrapQ HP anion exchange column equilibrated in E1 Buffer A, and eluted utilizing a linear gradient from E1 Buffer A to E1 Buffer B (100 mM to 1000 mM potassium chloride) over 15 CV. Fractions containing the E1 were pooled and concentrated to 40 mg/ml using a 100 kDa cutoff centrifugal concentrator. 0.2 mM of ThDP was added before flash-freezing in liquid nitrogen and storage at -80 °C.

2.2.4.3 Purification of the *B. subtilis* PDH E2 CDΔ9 trimers

The protein was purified via Ni-NTA chromatography (chapter 2.2.4.1). TEV protease was added in a ratio of 1:200 (w/w) to remove the tag and the protein was dialyzed against E2 Dialysis Buffer overnight at 4 °C. The trimers were further purified with a Superdex 200 HiLoad 26/600 gel filtration column equilibrated in E2 GF Buffer. Fractions containing the protein were identified via SDS-PAGE. The protein was concentrated to 30 mg/ml using a 50 kDa cutoff centrifugal concentrator before flash-freezing in liquid nitrogen and storage at -80 °C.

2.2.4.4 Purification of the *B. subtilis* PDH E3

The E3 was purified following the same protocol as for the E1, but without the addition of ThDP. The E3 was concentrated to 25 mg/ml using a 50 kDa cutoff centrifugal concentrator before flash-freezing in liquid nitrogen and storage at -80 °C.

2.2.4.5 Purification of *V. pacos* NB

The nanobody was purified via Ni-NTA chromatography (chapter 2.2.4.1). Nedp1 protease was kindly provided by Dr. Trevor Huyton (department of Dirk Görlich, MPINAT, Göttingen) [156]. Nedp1 protease was added in a ratio of 1:2000 (w/w) to cleave the tag and the protein was dialyzed against NB Gel Filtration Buffer overnight at 4 °C. The NB was further purified with a Superdex 75 HiLoad 26/600 gel filtration column. Fractions containing the protein were identified via SDS-PAGE. The protein was concentrated to 15 mg/ml using a 3 kDa cutoff centrifugal concentrator before flash-freezing in liquid nitrogen and storage at -80 °C.

2.2.4.6 Preparation of the E1-NB complex

Stock solutions of both E1 and NB were thawed and stored on ice. The nanobody was added to the E1 in a 3x molar excess (280 µM E1 and 840 µM NB) and equilibrated on ice

for 15 min. The protein complex was then loaded on a Superdex 200 HiLoad 26/600 gel filtration column equilibrated in E1-NB GF Buffer and eluted over 1.5 CV. Fractions containing the E1-NB complex were pooled, concentrated to 11 mg/ml using a 50 kDa cutoff centrifugal concentrator and supplemented with 0.2 mM ThDP before crystallization.

2.2.5 SDS-Polyacrylamide gel electrophoresis (SDS-PAGE)

Different fractions were analyzed by SDS-PAGE during protein purification to check the homogeneity of the sample. The protein samples were either analyzed on pre-cast 4-15% polyacrylamide gradient gels or pre-cast “anykD” gels, both purchased from Bio-Rad. 6 µl of a 6x SDS Loading Dye was added to 20 µl of sample solution and mixed. 6 µl of the solution was loaded on the gel. The gel was run at 200 V for 34 minutes and stained in Coomassie Staining Solution for 30 minutes. The excess of dye was removed by incubation in Coomassie Destaining Solution for 20 minutes before visual inspection.

2.2.6 Crystallization

2.2.6.1 Crystallization of the E1

The E1 was crystallized at 18 °C in 24-well sitting drop vapor diffusion plates by mixing 1 µl of protein solution (5 mg/ml) with 1 µl of reservoir solution containing 19% (w/v) PEG 400, 0.01 M sodium acetate pH 4.7, 0.44 M ammonium chloride, and 16 % MPD. Initial crystallization trials were performed by Dr. Ai Woon Yee (former postdoc in our group). Crystals appeared overnight and grew to a final size of 100 x 100 x 100 μm^3 in 2 days. The E1 crystallized in the space group P1 with unit cell parameters a=80.8 Å, b=84.4 Å, c=98.4 Å, α=93.2°, β=93.8°, γ=92.2°. The asymmetric unit contained two E1 hetero-tetramers.

2.2.6.2 Crystallization of the E1-NB complex

Native E1-NB and mutants ($E1_{H128N}$-NB, $E1_{H273N}$-NB) were crystallized at 18 °C in 24-well sitting drop vapor diffusion plates by mixing 1 µl of protein solution (11 mg/ml) with 1 µl of reservoir solution containing 16% (w/v) PEG 3350, 0.1 M Tris or MMT pH 8.0, 0.275 M $MgCl_2$ and 0.5 %(v/v) ethylene glycol. Crystals appeared overnight and grew to a final size of 300 x 300 x 300 μm^3 in 3 days. E1-NB crystallized in space group $P2_12_12$ with unit cell parameters a=185.9 Å, b=101.8 Å, c=86.7 Å, α=90°, β=90°, γ=90°. The asymmetric unit contained one E1 hetero-tetramer bound to two nanobodies.

2.2.6.3 Preparation of E1-NB microcrystals

The crystallization condition for E1-NB was adapted to yield microcrystals. The microcrystal suspension was prepared in 1.5 ml Eppendorf tubes by mixing 200 µl of protein solution (11 mg/ml) into 200 µl of precipitant solution containing 0.1 M Tris 8.0, 0.4 M $MgCl_2$ and 25 % PEG 3350. The crystals were resuspended every 30 minutes by pipetting for a total duration of 3 h. This prevented crystals sticking to the sides of the tube. The microcrystals grew to a final size of 40 x 40 x 20 μm^3 in 5 h at 18 °C and collected at the bottom of the tube. The crystals were stored at 18 °C.

2.2.6.4 Crystallization of E2 CD trimer

The E2 CD crystallized in two different crystallization conditions. Crystallization condition I: E2CD was crystallized at 18 °C in 96-well vapor batch plates by mixing 1 µl of protein solution (12 mg/ml) with 1 µl of reservoir solution containing 2.6 M ammonium sulfate, 0.1 M sodium citrate pH 5.2 and 1 % (w/v) PEG400. The drops were covered by 10 µl paraffin oil to prevent diffusion. Cubic crystals appeared overnight and grew to a final size of 300 x 300 x 300 μm^3 in 5 days. E2 CD crystallized in space group I23 with unit cell parameters a=117.7 Å, b=117.7 Å, c=117.7 Å, α=90°, β=90°, γ=90°. The asymmetric unit contained a single monomer of the trimer.

Crystallization condition II: E2CD was crystallized at 18 °C in 24-well sitting drop vapor diffusion plates by mixing 1 µl of protein solution (12 mg/ml) with 1 µl of reservoir solution containing 17% PEG 4000, 0.1 M Tris 8.0 and 0.2 M $CaCl_2$. Crystals appeared overnight and grew to a final size of 100 x 100 x 100 μm^3 in 3 days. E2 CD crystallized in space group $P2_1$ with unit cell parameters a=72.1 Å, b=164.0 Å, c=73.1 Å, α=90.0°, β=118.2°, γ=90.0°. The asymmetric unit contained two trimers.

2.2.6.5 Crystallization of E3

The native E3 and $E3_{C52S}$ were both crystallized at 18 °C in 24-well hanging drop vapor diffusion plates using glass or polycarbonate cover slides. The E3 crystallized by mixing 1 µl protein solution (14 mg/ml) and 1 µl reservoir solution containing 0.15 M imidazole malate pH 8.5, 1% (v/v) glycerol and 2.2 M ammonium sulfate. Tetragonal crystals appeared overnight and grew to a final size of 300 x 300 x 300 μm_3 in 3 days. E3 and $E3_{C52S}$ crystallized in space group $I4_1$ with unit cell parameters a=132.2 Å, b=132.2 Å, c=63.3 Å, α=90°, β=90°, γ=90°. The asymmetric unit contained one monomer of the dimer.

2.2.7 Preparation of stock solutions

All stock solutions were stored at -80 °C. A stock solution of 20 mM ThDP was prepared in 50 mM MES pH 5.0 and 50 mM $MgCl_2$. A 100 mM stock solution of methyl acetyl phosphonate (MAP) was prepared in H_2O. A 200 mM stock solution of lipoamide-dPEG-(4)-OMe was prepared in ethylene glycol. 500 mM stock solutions of sodium pyruvate, α-keto-methylvalerate (MVA), α-keto-isocaproate (CAP), and fluoropyruvate were prepared in H_2O. 200 mM stock solutions of 6-(acetylthio)hexanoic acid (6AH) and 8-(acetamido)octanoic acid (8AO) were prepared in dimethyl sulfoxide (DMSO). A 500 mM stock solution of Tris-(2-carboxyethyl)phosphine (TCEP) was prepared in H_2O and adjusted to pH 7.0 with NaOH. A 50 mM Coenzyme A (CoA) stock was prepared in H_2O.

2.2.8 Post-crystallization treatment and soaks

2.2.8.1 E1-NB soaks

E1-NB crystals were cryoprotected in E1 Cryo Solution A by a slow drop exchange at 18 °C. The ethylene glycol (EDO) concentration was gradually increased from 0.5 - 5 - 10 - 15 - 20 % (v/v). To capture the post-decarboxylation intermediate carbanion/enamine-ThDP, cryoprotected E1-NB crystals were incubated in E1 Cryo Solution A containing 50 mM of sodium pyruvate for 5 minutes before flash freezing in liquid nitrogen. To capture the HEP-ThDP inhibitor complex, cryo-protected E1-NB crystals were incubated in E1 Cryo Solution containing 20 mM methyl-acetyl phosphonate (MAP) for 5 minutes before flash-freezing. MAP was kindly synthesized by Vladimir Belov (Synthetic Chemistry Facility, MPINAT, Göttingen). To capture the tricyclic ThDP structure, cryo-protected E1-NB crystals were soaked with 80 mM fluoropyruvate for 2 minutes before flash-freezing. To capture the post-decarboxylation intermediates with BCDHc substrates, cryoprotected E1-NB crystals were either incubated in E1 Cryo Solution A containing 50 mM MVA for 5 minutes or 50 mM CAP for 10 minutes before flash-freezing. $E1_{H128N}$-NB and $E1_{H273N}$-NB crystals were cryo-protected in E1 Cryo Solution A and incubated in E1 Cryo Solution containing 50 mM sodium pyruvate for 5 minutes before flash-freezing. To trap the pre-decarboxylation intermediate lactyl-ThDP, the crystal drop was gradually exchanged with E1 Stabilization Solution at pH 5.0 and the crystals were subjected to a temperature gradient from 18 to 4 °C over 12 h. The crystals were then cryo-protected in E1 Cryo Solution B at pH 5.0 by a slow drop exchange and then transferred to E1 Cryo solution B containing 100 mM sodium pyruvate for 50 s. The crystals were then flash-frozen in liquid nitrogen.

2.2.8.2 E2CD substrate soaks

The lipoamide was reduced by incubation with TCEP (100 mM lipoamide-dPEG-(4)-OMe, 200 mM TCEP) for 30 minutes at 37 °C. Crystallization condition I: The paraffin oil was removed from the batch, and the crystals were cryo-protected in the 96-well batch plate with E2 Cryo Solution IA or IB, and transferred to a vapor diffusion plate. The crystals were soaked with E2 Cryo Solution IA or IB containing 7.5 mM reduced lipoamide-dPEG-(4)-OMe for 24h at 18 °C. Crystallization condition II: The crystals were cryo-protected in E2 Cryo Solution II containing 10 mM CoA and incubated for 10 minutes before flash-freezing in liquid nitrogen.

2.2.8.3 E3 substrate soaks

Crystals of native E3 and $E3_{C52S}$ were both cryo-protected in E3 Cryo Solution by a slow drop exchange. To trap the mixed disulfide the $E3_{C52S}$ crystals were then incubated in E3 Cryo Solution containing 3 mM lipoamide-dPEG-(4)-OMe (from a 200 mM stock solution in ethylene glycol), and 5 mM NAD^+ (from a 50 mM stock solution in H_2O) for 16 h at 18 °C. The crystals were shortly washed in E3 Cryo Solution to remove precipitated lipoamide before flash-freezing.

2.2.8.4 E1-NB microcrystals

Shortly before the time-resolved experiments, the supernatant in the 1.5 ml reaction tube containing the microcrystal suspension was carefully removed, and exchanged with Micro-crystal Cryo Solution to protect the crystals from dehydration by the vacuum suction.

2.2.9 Diffraction data collection and processing

The crystals were harvested in Mitegen MicroLoops at either 18 °C or 4 °C and vitrified in liquid nitrogen. Diffraction data were collected under a nitrogen stream at 100 K. Diffraction data were collected at the beamline P14 at the PETRA III storage ring (DESY, Hamburg) using a MD3 vertical-spindle diffractometer and a EIGER CdTe detector (DECTRIS). The beam is focused by a compound refractive lens (CRL) transfocator located upstream of the sample. This generates a “top-hat” beam-profile with a flux up to 4 x 10^{12} photons per second. The beam size was adjusted to fit the crystal size (300 x 300 μm^2) to illuminate the full crystal. The data was collected either at 26.7 keV (0.47 Å), or 18.0 keV (0.69 Å), or 12.7 keV (0.97 Å). The data was collected using a workflow developed by Global Phasing. The workflow first obtains 60 diffraction images to index the crystal. Based on crystal symmetry and rotation, the workflow calculates an optimal data collection strategy, which results in high multiplicity and avoids cusps. The E1-NB datasets were collected in three

sweeps with a 360° rotation each accumulating a total dose of 1.5 mega Gray (MGy). The E2CD data was collected in three sweeps with a 360° rotation each, accumulating a total dose of 1.0 MGy. The E3 was collected in three sweeps with one 360° rotation and two 199° rotations, with a total dose of 1.5 MGy. The data was processed using the autoPROC program package, which includes, among other things, indexing and integration by XDS and POINTLESS, scaling by AIMLESS, and analysis of anisotropy by STARANISO.

2.2.10 Structure determination and refinement

The E1 structure was solved by molecular replacement using the *Geobacillus stearothermophilus* PDH E1 structure (PDB ID:1W85) as search model. The nanobody structure was built in automatically by the program BUCANEER and several manual refinement in coot using its protein sequence. Initial phases for the E2CD were determined by molecular replacement using a monomer of the *G. Stearothermophilus* PDH core structure (PDB ID:1B5S) as search model. The E3 structure was solved using the *G. Stearothermophilus* PDH E3 as search model (PDB ID:1EBD). All the models listed above were built by several cycles of manual model building in COOT and reciprocal space refinement in refmac or BUSTER. Stereo-chemical descriptions of ligands were created using the program JLigand and grade2. The restraints of both ThDP and lactyl-ThDP ligands were relaxed by increasing bond distance and bond angle sigma values and removing planar restraints. Table 4 lists the refinement strategies applied for the different datasets.

Table 4: Refinement strategies

E1	E1-NB	E2CD	E3
rigid body refinement + NCS refinement + anisotropic refinement	Alternating ADP + occupancy refinement	rigid body refinement + NCS refinement + anisotropic refinement	TLS refinement + NCS refinement

2.2.11 Time-resolved serial crystallography

2.2.11.1 HARE time-resolved experiment

The microcrystal concentration was assayed by visual inspection in a counting chamber under a microscope, and adjusted to yield optimal hit rates. A 200 µl suspension of cryoprotected E1-NB microcrystal was applied to an silicon chip in a humidity controlled chamber at 90% relative humidity (r.H.) at room temperature. The crystals were driven into the

compartments of the chip by moderate vacuum suction for 1-3 s. The microcrystals were protected against dehydration from one site by a mylar foil and the chip was transferred to the experimental hutch. The chip, the vacuum pump, and the general experimental layout is described by Schulz, Mehrabi, and Stetten et al [130], [136], [157]. The relative humidity was kept constant at 90% during data collection. The crystals were exposed for 5 ms by a 15 µm beam with a flux of $2*10^{12}$ photons/s, which corresponded to a dose of 20 kGy. First, a dark state was recorded. The reaction was then initiated by the liquid application method for time-resolved analyses (LAMA) [136]. Small droplets of Microcrystal Cryo Solution containing 100 mM sodium pyruvate were applied on the crystals, and the reaction was probed after 0.2, 0.4, 1.1, 1.9, 4.8, 7.7 and 38.1 s, which correspond to HARE numbers 5, 10, 20, 40, 100, 200, and 800, respectively. The serial data was kindly processed by Dr. David von Stetten (EMBL, Hamburg) using the software package CrystFEL.

2.2.11.2 Dehydration experiments

The chip was loaded as described above and transferred to the experimental hutch. The relative humidity was adjusted to 60, 75, or 90 %, and the crystals were equilibrated for 10 minutes before data collection.

2.2.11.3 Sample application via centrifugation

200 µl of E1-NB microcrystal suspension was applied onto a silicon chip in a humidity controlled chamber at 90% relative humidity (r.H.) at room temperature. The chip was placed into a 3D printed on-chip crystallization box with Microcrystal Cryo Solution in the reservoir and sealed by crystal tape. The box layout is described by Norton-Baker et al [158]. The box was placed into a centrifugal evaporator unit (Eppendorf) with an A-2-VC plate rotor and gently centrifuged for 1 min before data collection at 90% r.H. at room temperature.

2.2.11.4 Cryo-protection analysis via helical mesh scan

E1-NB microcrystals incubated in Microcrystal Cryo Solution containing different EDO concentrations were fished with MiTeGen mesh loops and mounted at room temperature under a humidity controlled stream. A helical mesh scan was performed at different relative humidity values to analyze the influence of cryo protection and humidity on resolution and hit rate. The crystals were incubated at specified humidity levels for 5 minutes before data collection. A description of the helical scan can be found here [159]. Dr. Gleb Bourenkov (Schneider group, EMBL, Hamburg) kindly performed the helical mesh scan.

2.2.12 Alignments

Structural alignments of E1 against E1-NB were performed in PyMol using the “align” command, which included no outlier rejection cutoff for the all-atoms RMS of the E1/E1-NB active site alignment, and default values for the outlier rejection cutoff in RMS (2.0 Å) and 5 outlier rejection cycles during the alignment of Cα atoms of the full protein. Residues within 6 Å distance to ThDP were chosen for the active site alignment.

Multiple protein sequence alignment was performed using the Clustal Omega webserver (https://www.ebi.ac.uk/Tools/msa/clustalo/). The alignment was visualized with JalView. The sequences were colored according to the BLOSUM62 score using the 30% conservation coloring threshold.

The N-terminal methionine was not included in numbering of the *B. subtilis* PDH E1 residues in the figures.

3 Results

The pyruvate dehydrogenase complex (PDHc) of *Bacillus subtilis* is a large multiprotein complex consisting of multiple copies of three different enzymes, E1, E2 and E3. This macromolecular machine has been subject to studies for over 60 years, but structures have not yet resolved its detailed organization due to its large size, and dynamics. The E1 enzyme is a thiamine diphosphate (ThDP)-dependent enzyme, which catalyzes two successive reactions: the oxidative decarboxylation of pyruvate, and the reductive trans-acetylation onto the lipoic acid prosthetic group of the E2-LD. Structural details of reaction intermediates of the decarboxylation reaction have been elucidated for other ThDP-dependent enzymes, but not for the pyruvate dehydrogenase E1 [32,113,160]. X-ray crystallography, and time-resolved serial crystallography at synchrotron light sources (SSX), in recent years, are suited to collect multiple snapshots in the course of substrate turnover by enzymes [161]. To gain insights into the detailed reaction mechanism of the E1 enzyme catalyzed reaction and protein dynamics, experiments were performed at the new endstation for time-resolved serial crystallography, T-REXX at PETRA III, Hamburg.

3.1 Microcrystallization for time-resolved crystallography

Hundreds of microliters of crystal suspension are needed to fill the compartments of the chip used in the SSX experiment at the T-REXX [130]. Therefore, efficient protein purification and crystallization protocols are crucial. The *B. subtilis* E1 subunit was expressed recombinantly in *Escherichia coli* and purified via Ni-NTA chromatography, and anion exchange chromatography. Fractions of the different purification steps were analyzed by SDS-PAGE (figure 3.1A and B). The E1 enzyme eluted from the anion exchange column in one clean peak, which contained both α- and β-subunits. The purification procedure yielded approximately 700 mg protein. The E1 was crystallized in 19% (w/v) PEG 400, 0.01 M sodium acetate pH 4.7, 0.44 M ammonium chloride and 16% MPD. The crystals grew in space group P1 and diffracted to 1.5-1.9 Å. To elucidate the decarboxylation of pyruvate, three-atom changes in a 6-atom molecule need to be resolved spatially, which requires higher resolution. Therefore, new crystallization conditions were sought to improve the resolution. Nanobodies have been used as crystallization chaperones for proteins which are hard to crystallize, for example membrane proteins [162] or to improve crystal diffraction. Nanobody binding can reduce the conformational heterogeneity of the sample or simply provide areas for crystal contacts [163]. The E1 enzyme was therefore purified and crystallized in the presence of a nanobody (NB). The nanobody was raised by immunizing alpacas with the full *B. subtilis* PDH complex in the department of Dirk Görlich, MPINAT, Göttingen [164]. Its purification is depicted in Appendix figure 2.

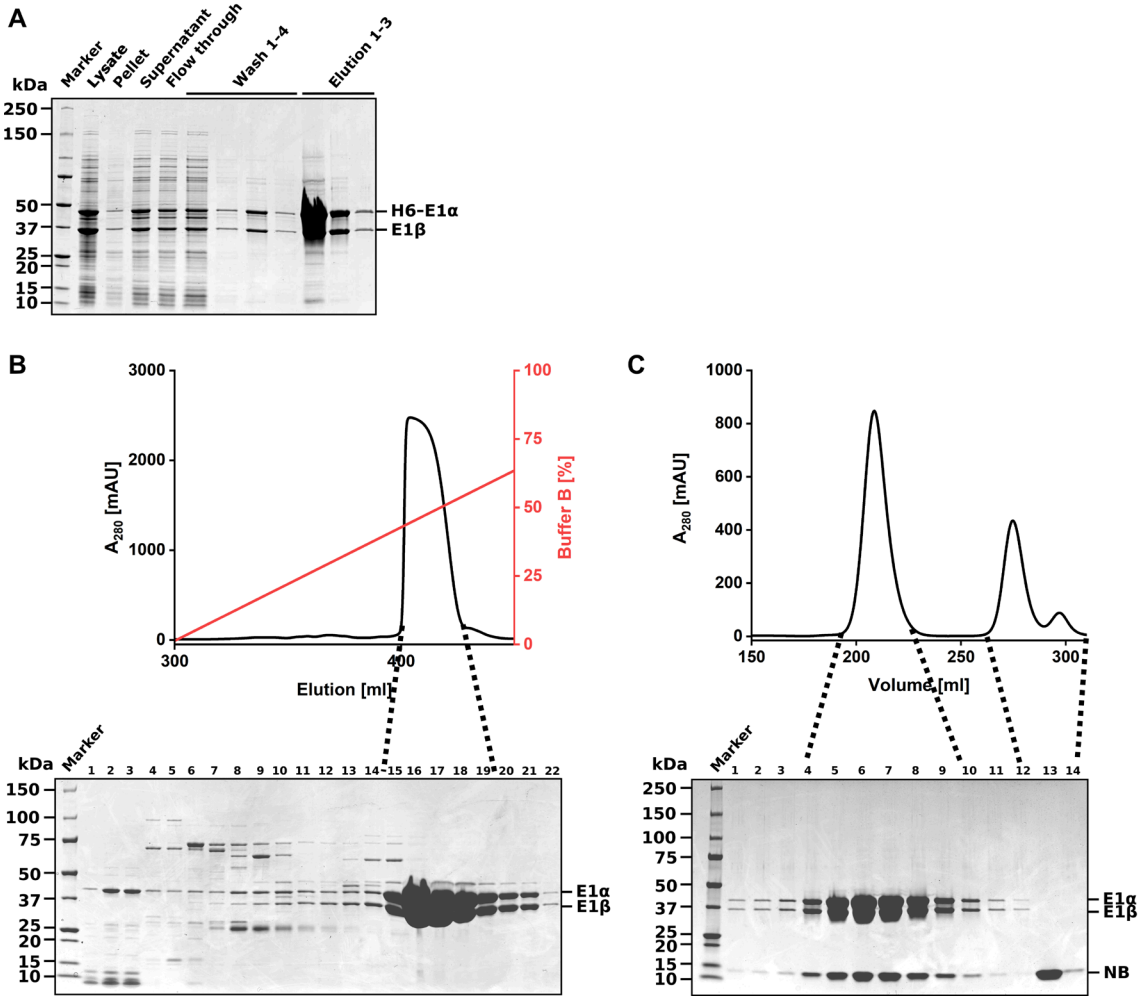

Figure 3.1: SDS-PAGE analysis of the PDH E1 and E1-NB purification. The *B. subtilis* PDH E1 was purified by Ni-NTA chromatography (A) followed by anion exchange chromatography (B). The E1-NB complex was purified by size exclusion chromatography (C). E1 α- and β-subunits run at 40 kDa and 35 kDa, respectively. The nanobody runs at 15 kDa. Fractions of the chromatogram analyzed via SDS-PAGE are indicated by dotted lines.

Initial biochemical characterization was performed by Dr. Prajapati (group of Kai Tittmann, University of Göttingen) and Dr. Ai Woon Yee (former postdoc in our group). The E1-NB complex was purified by gel filtration (figure 3.1C), which showed two peaks. One peak contained the E1 bound to NB, which was indicated by an additional band running at 15 kDa in the SDS-gel corresponding to the NB. The other peak contained the excess of NB. The E1-NB complex was crystallized in a condition containing 0.1 M Tris 8.0, 0.2 M $MgCl_2$ and 16 % (w/v) PEG 3350. The space group was $P2_12_12$ and initial crystals diffracted to 1.4 Å resolution. Structures of both *B. subtilis* E1 and E1-NB were solved by molecular replacement using the *Geobacillus stearothermophilus* E1 structure as search model (PDB ID:1W85). The asymmetric unit contained two E1 molecules in the E1 crystals and one E1 molecule binding two nanobodies in the E1-NB crystals. The nanobodies bind to a cleft

formed between helix 2 and 9 of the E1 α-subunit, the binding site is 25 Å away from the active site (figure 3.2A). Figure 3.2B shows the E1-NB binding interface which is characterized by hydrogen bonds between residues Ser52 and Thr57, with Glu326 of the E1. NB Pro102 protrudes into a hydrophobic pocket formed by E1 Trp112, Leu117 and Phe57.

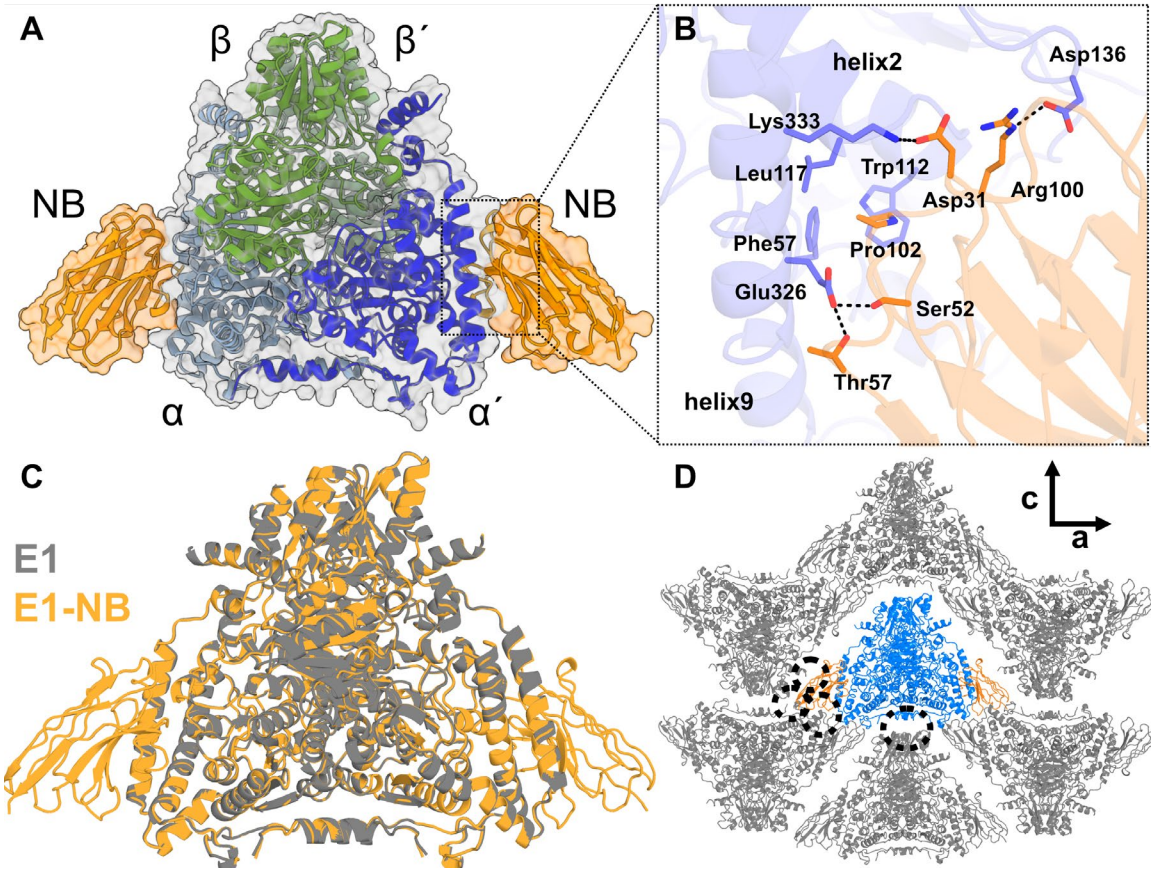

Figure 3.2: E1 nanobody interaction. A) Two copies of the nanobody (orange) each bind an α-subunit (blue and grey) in a cleft between helix 4 and 11. The β-subunits are depicted in green. B) Exemplary interactions of E1α and NB. Residues Ser52 and Thr57 of the nanobody form hydrogen bonds to glutamate Glu326. Pro102 resides in a hydrophobic pocket formed by residues Trp112, Leu117 and Phe58 of the α-subunit. Residues Asp31 and Arg100 form ionic interactions with Lys333 and Asp136. C) A structure alignment of E1 and E1-NB shows no major structural changes upon NB binding since the Cα RMSD is 0.23 Å. D) The a-c plane of the crystal lattice is shown. The asymmetric unit shows the E1 (blue) bound to two copies of nanobody (orange). Crystal contacts are marked by dotted circles. The C-terminus of E1α forms a crystal contact with E1β. The nanobody facilitates three crystal contacts.

The interaction is also characterized by multiple ionic interactions, such as the interaction between Asp31 and Arg100 with Lys333 and Asp136, respectively. A structural alignment of E1-NB against the E1 showed that nanobody binding induced no major structural changes (figure 3.2C), since the Cα root mean square deviation (RMSD) is 0.23 Å. The all-atoms RMSD of the active site residues is 0.16 Å. The nanobody facilitates three crystal contacts (figure 3.2D): The first contact is formed with the C-terminus of E1α, the second with another nanobody and the third crystal contact is formed with a helix of E1α. Both

active sites contained ThDP (figure 3.3). The active sites, like in the human E1, are formed at the interface of α- and β-subunits. The cofactors are separated by a 20 Å long channel. ThDP is bound at the active site through multiple hydrophobic and hydrophilic interactions. The diphosphate is coordinated by Arg105, Tyr104 and His273.

Table 5: Alignment of E1 and E1-NB

Cα RMSD [Å]	Active site residues (all-atoms RMSD) [Å]
0.23	0.16

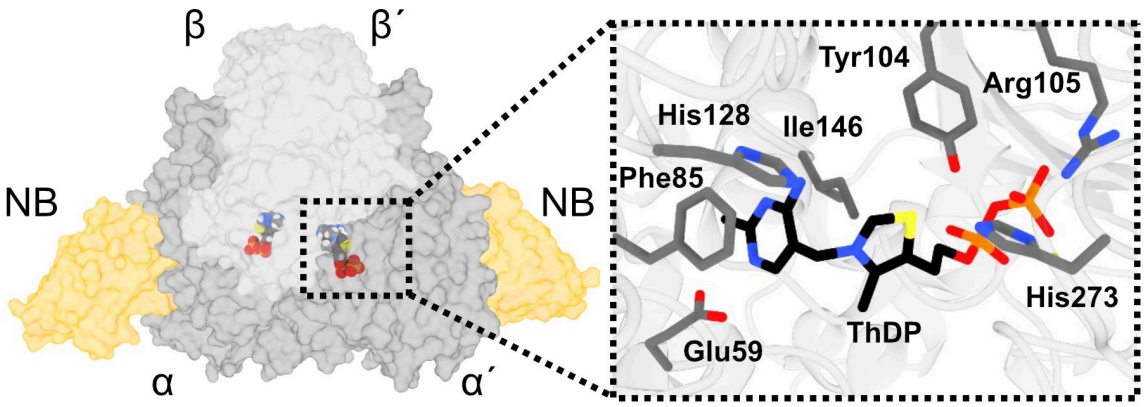

Figure 3.3: Surface representation of the E1-NB complex. The heterotetramer is bound by two nanobodies (orange). The enzyme contains two active sites formed at the E1α and E1β interface. Each site contains one thiamine diphosphate (ThDP) molecule. A closer look into the active sites shows that the diphosphate is surrounded by positively charged residues Arg105 and His273, as well as Tyr104. The aminopyrimidine ring is pi-stacked to Phe85. The conserved Glu59 is shown.

The aminopyrimidine (AP) ring is pi-stacked against Phe85. Glu59 forms a polar contact to N1´ of the aminopyrimidine ring. This interaction is conserved amongst all ThDP-dependent enzymes, as it accelerates the rate of cofactor activation [46].

Since the purification and crystallization protocol led to well diffracting crystals, a micro-crystallization protocol was established to grow microcrystals suitable for SSX experiments. Several micro-crystallization techniques have been reported, such as batch crystallization, free interface diffusion (FID) and FID centrifugation [165]. Other techniques include mechanical disruption of bigger crystals into micro- or nanocrystals [166]. Microcrystals of both E1 and E1-NB were grown by batch crystallization in 96-well plates by increasing the PEG concentration, which lead to a higher number of smaller crystals with a size of 20-40 µm (figure 3.4A and B). Microcrystals already appeared after 30 minutes and reached their full size after 6 h. Microcrystallization was scaled up to a final volume of 500 µl in 1.5 ml Eppendorf tubes (figure 3.4C). However, most of the crystals were stuck to the sites of the reaction tube. The solution to that problem was to resuspend the crystals every 30 minutes for 3 h, which prevented nucleation at the sides of the tube. Micro-crystallization

of the E1 caused precipitation, which collected at the bottom of the tube together with the microcrystals. E1-NB micro-crystallized without precipitation. The E1-NB microcrystals were chosen for the SSX experiments, because of little precipitation during crystallization, a more defined 3D shape, better resolution, and less anisotropic diffraction. The nanobody binds 25 Å away from the active site and structural alignment showed no changes upon binding. This observation also spoke for the E1-NB crystallization system.

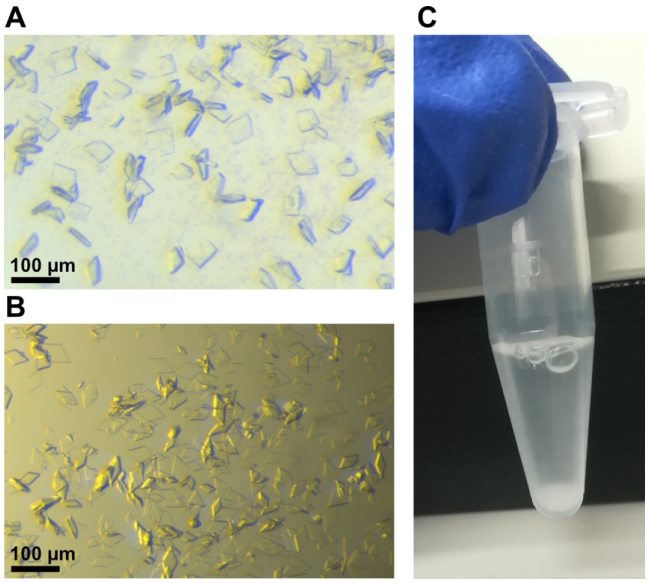

Figure 3.4: Microcrystallization of the E1. A) Microcrystals of E1 crystallize in space group P1 and grew to a size of 30-40 µm. Precipitate is formed during crystallization. B) Microcrystals of E1-NB crystallized in space group $P2_12_12$ and grew to a size of 20-40 µm. C) A 400 µl microcrystal suspension of the E1-NB in an Eppendorf reaction tube. The crystals collected at the bottom of the tube.

3.2 A new fixed-target setup for serial synchrotron crystallography

A new endstation for time-resolved synchrotron crystallography at PETRA III, DESY, termed T-REXX, has recently opened its doors to users. The setup utilizes a silicon chip with 25,600 compartments. Microcrystals can be applied to the compartments by via short vacuum suction, centrifugation, or on-chip crystallization. Both crystal application and data collection are humidity and temperature controlled. Reactions can be initiated via a 355 nm laser, or by application of small droplets of concentrated substrate solution, termed the LAMA approach. A hit-and-return approach termed HARE decreases total data collection time. In HARE, the geometry of the chip and speed of the translation system determine the delay time of the pump-probe experiment [130,136,137]. Figure 3.5 shows a typical pump-probe setup using the LAMA approach for reaction initiation. Each compartment is first probed by a single X-ray shot to determine the DARK state. The reaction is then initiated by substrate application from an injector nozzle, and the reaction is then probed again after

a specific delay time, Δt. Data collected from one chip correspond to one time-point in the reaction. Several chips are needed to cover the full span of the reaction. This setup offers time-resolutions in the ms to minute range. Substrate binding and protein motions of the model enzymes fluoroacetate dehalogenase and xylose isomerase were resolved at 1.8 Å using this setup [130,167].

In serial crystallography structures are solved from thousands of randomly oriented crystals instead of rotating one large crystal by 360°. Therefore, data completeness and redundancy depend on the number of diffracting crystals on the chip. The ratio of diffraction patterns to the number of X-ray probes is termed hit rate. Since E1-NB constituted a robust micro-crystallization system, different crystal application methods were tested to maximize the hit rate.

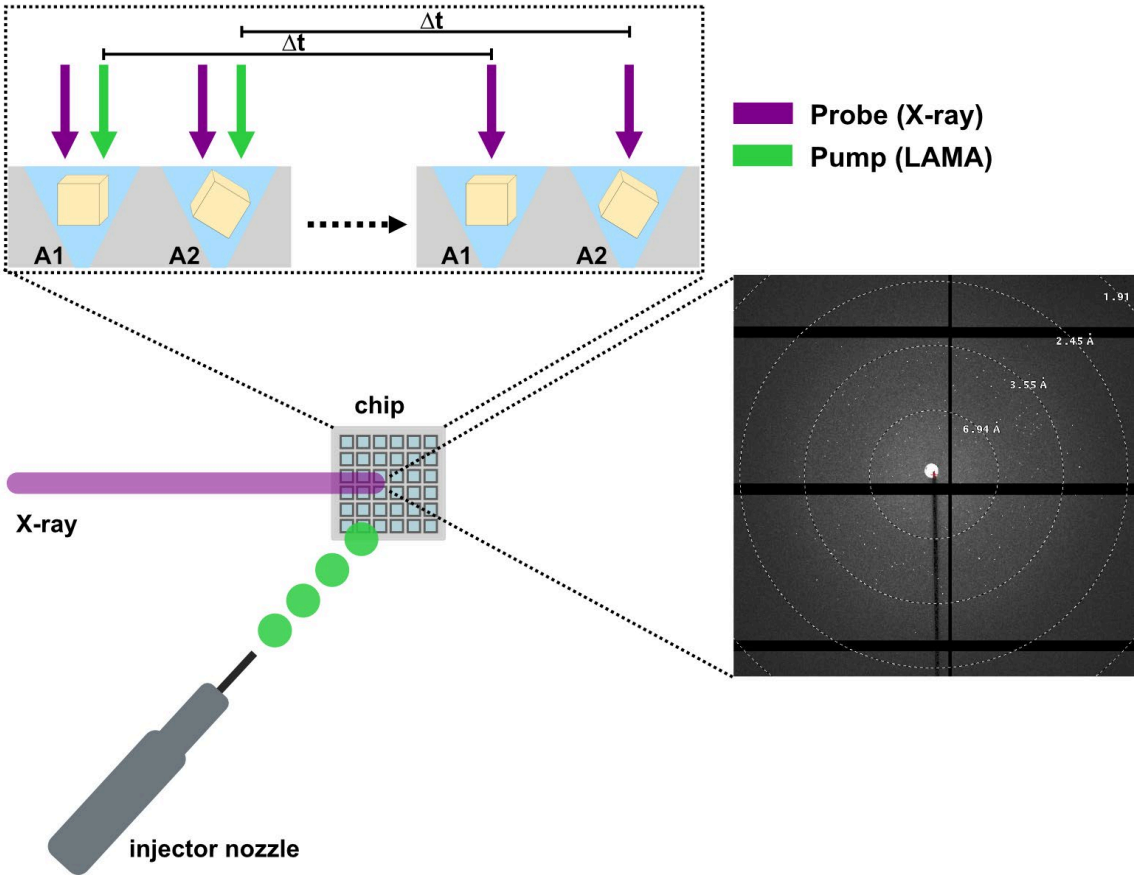

Figure 3.5: The setup for time-resolved serial crystallography at PETRAIII, DESY, Hamburg. An illustration of the setup for serial synchrotron X-ray crystallography is shown. Thousands of microcrystals are sitting in small compartments on a silicon chip. The reaction is first probed by the X-ray and the diffraction pattern are collected to solve the pre-reaction (DARK) structure. The reaction is initiated by application of small droplets of substrate solution by the injector nozzle. The crystals are probed again after a defined time delay.

3.3 Optimization of sample delivery and crystal diffraction

In other time-resolved experiments reported in the literature, ligands could be modelled correctly using only a subset of diffraction images (800-5000), which corresponds to a hit rate of 3-20% using silicon chips with 25,600 compartments [168]. However, the number of diffraction patterns which result in high-quality datasets depend on multiple factors, such as crystal symmetry, how populated reaction intermediates are, and whether crystals show preferential orientations on the chip. Two crystal application methods were tested: centrifugation and vacuum application. The E1-NB microcrystal suspension was pipetted on a silicon chip. The crystals were driven into the small compartments by either short centrifugation or vacuum application and then screened in a HARE experiment gathering two datasets per chip. The data was processed using the software package CrystFEL and the resulting hit rate was analyzed (figure 3.6A). Blue dots show diffraction spots from the first probe, red spots display diffraction images from the second probe. Grey spots show compartments, which did not contain a diffracting crystal. Sample application via vacuum suction showed a higher hit rate than centrifugation. Vacuum application showed a hit rate of 43.7 %, which corresponds to 11,187 diffraction images per run. Sample application via centrifugation showed a hit rate of 7.5 %, which corresponded to 1,920 diffraction images per run. However, crystals in both methods diffracted only to 3 Å and the diffraction quality varied strongly from chip to chip. To improve diffraction, the relative humidity (r.H.) during data collection was optimized. Crystals were applied onto chips via vacuum suction, and equilibrated for 10 minutes at different relative humidity values before data collection. The effect of the relative humidity of the chip environment on the distribution of unit cell lengths and resolution was analyzed (figure 3.6B). At 90% r.H. the crystals diffracted to 3.2 Å. The cell axis lengths were a=187 Å, b=102 Å, c=88 Å. A reduction of the r.H. to 75% improved the diffraction to 2.3 Å resolution. The unit cell axis changed to a=175 Å, b=99 Å, c=90 Å, which corresponded to a shrinkage of the a-axis by 12 Å, the b-axis by 3 Å, and an expansion of the c-axis by 3 Å. Reducing the r.H. further to 60% resulted in reduced diffraction and further shrinkage of the unit cell to a=174 Å, b=99 Å, c=89 Å. 75% r.H. is optimal for the E1-NB crystals. However, the diffraction quality still fluctuated greatly among different repeats, and resolutions of 2.3 Å could not be reproduced. This could be explained by crystal damage due to uncontrolled dehydration by the vacuum pressure during crystal application.

To solve this problem, the decisive idea was to protect the microcrystals against dehydration by a cryo-protectant. There is a correlation between the ability to cryo-protect and reduction of the relative humidity, therefore the effect of cryo-protection and dehydration on crystal diffraction is linked [169,170]. Cryo protection is a form of controlled dehydration, since the cryo-protectant creates a relative humidity environment, which is lower than the

original crystallization solution, and therefore dehydrates the crystal. Ethylene glycol (EDO) was initially tried, since it is a common cryo-protectant. To find the optimal EDO concentration, the microcrystals were incubated in different EDO concentrations ranging from 10-30 % and mounted on mesh loops in a humidity controlled environment at room temperature. Data was collected by a helical mesh scan and the influence of EDO concentration and relative humidity on resolution (figure 3.7A) and hit rate (figure 3.7B) was analyzed. Crystals incubated in 25% EDO measured at 90% r.H. showed the best diffraction. These crystals diffracted to 2.3 Å. Crystals incubated in 20 or 30% EDO measured at 90% r.H. diffracted to 2.6 and 2.5 Å, respectively. A similar observation could be made for the hit rate. Crystals incubated in 25% EDO measured at 90% r.H. also showed the highest hit rate. 25% EDO corresponds to a relative humidity of 90%, calculated using the European Synchrotron Radiation Facility (ESRF) relative humidity calculator (https://www.esrf.fr/UsersAndScience/Experiments/MX/How_to_use_our_beamlines/forms/equation-3).

The general trend was that if the relative humidity of the environment matches the calculated relative humidity of the respective EDO concentration, crystals diffracted best, and meshes showed the highest hit rates. For example, crystals in 25 % EDO showed worse diffraction and hit rates when measured at 80 or 85 % r.H. in comparison to 90% r.H.. The findings derived from helical mesh scans could be translated to the silicon chips. When microcrystals incubated in 25% EDO were applied onto the chip via vacuum suction and measured at 90% r.H., hit rates were reproducibly above 40% and crystals diffracted reproducibly to 2.3-2.5 Å.

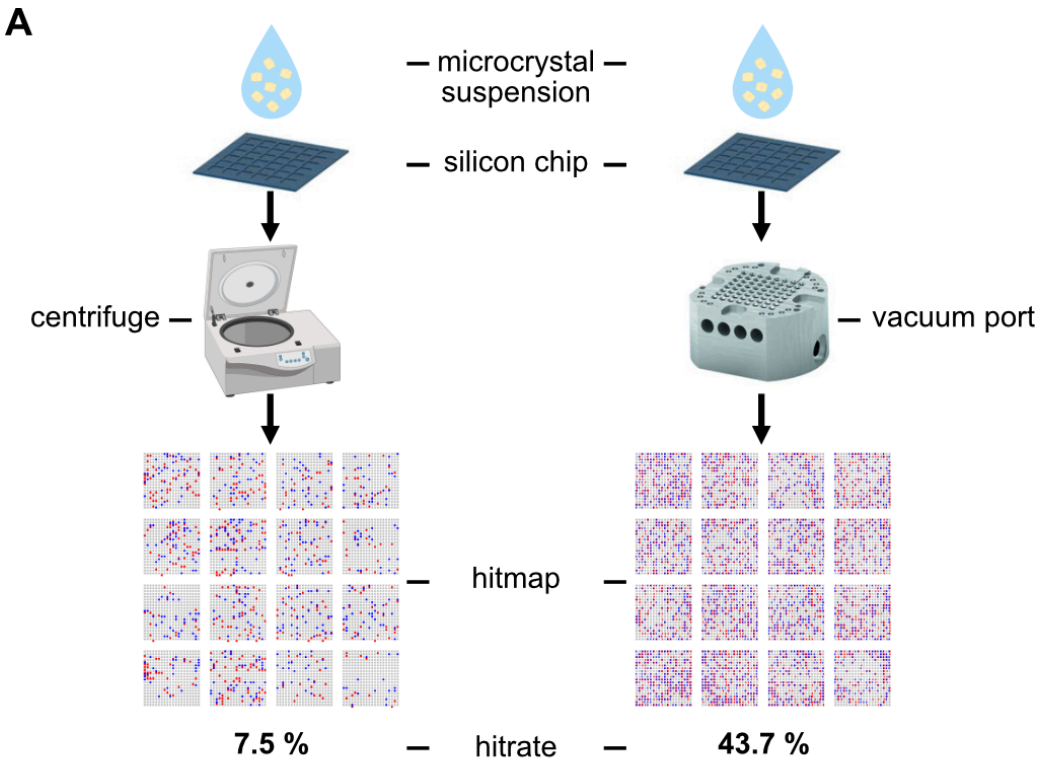

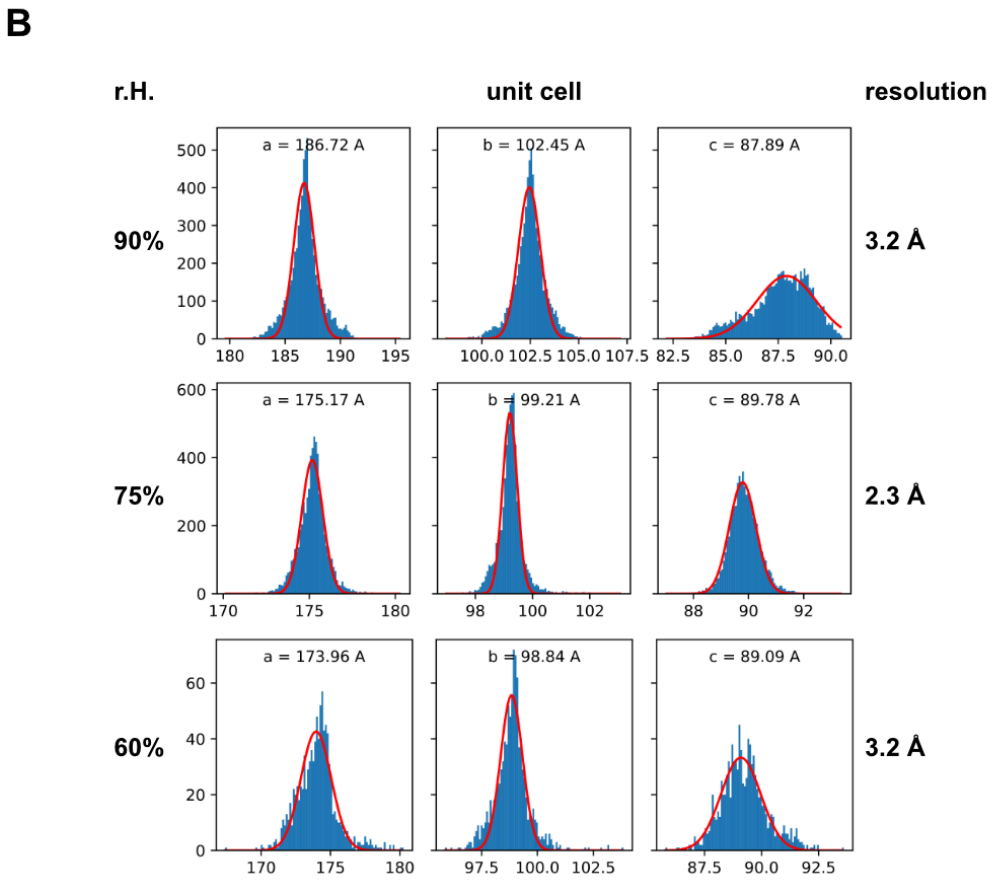

Figure 3.6: Optimization of sample application protocols. A) The E1-NB microcrystal suspension was applied onto silicon chips by either centrifugation or application of a short vacuum. Each compartment was exposed to X-rays and the resulting hitmaps were compared. Red dots correspond to the first dataset collected and blue dots correspond to the second dataset. Sample application via vacuum suction led to higher hit rates. B) Datasets were collected at different relative humidity values. The influence of the relative humidity on unit cell parameters and diffraction quality was analyzed. Crystals collected at 75% r.H. diffracted best. The image of the centrifuge was created with BioRender.com. The vacuum port and chip were modified and reproduced with permission from Mehrabi et al [190].

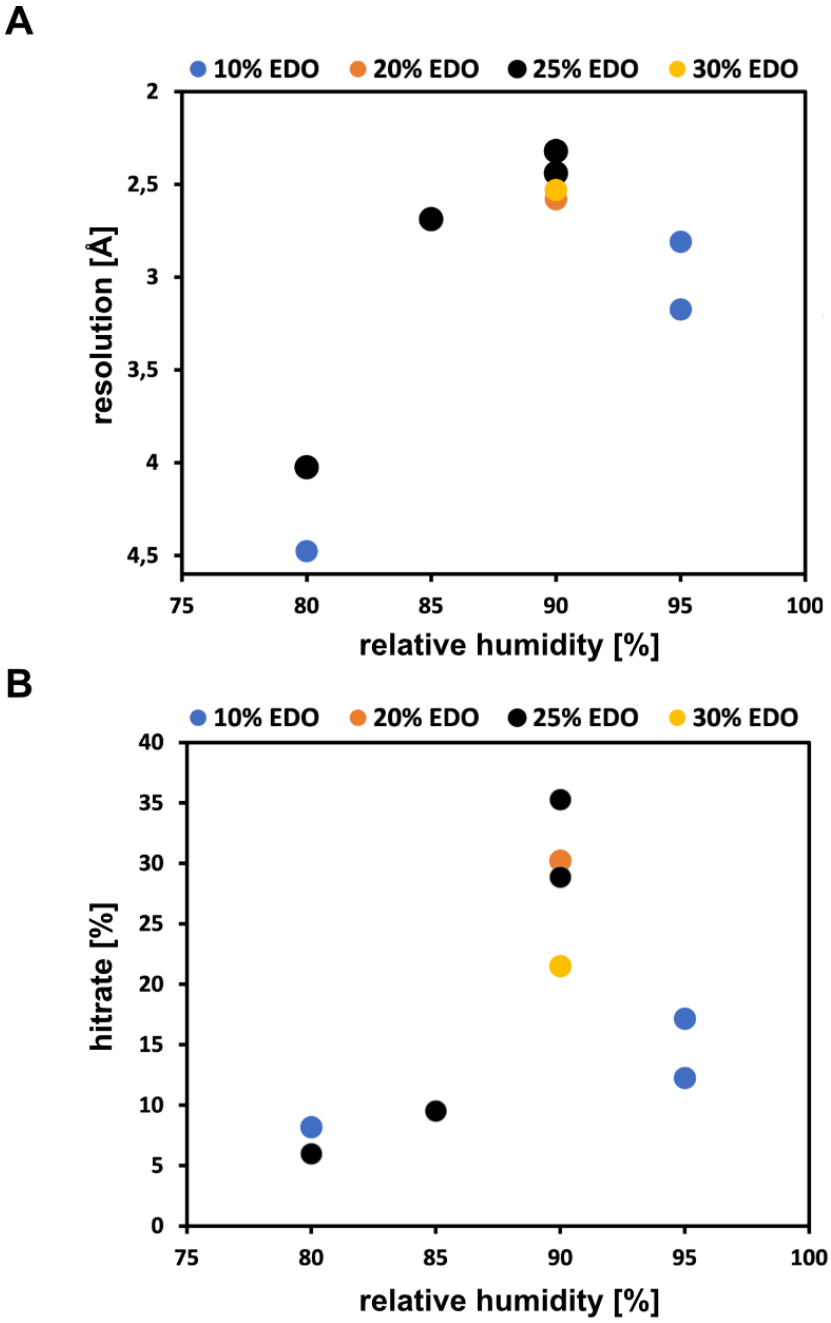

Figure 3.7: Room temperature helical mesh scan in different cryo concentrations. E1-NB microcrystals were incubated in different ethylene glycol (EDO) concentrations and fished with mesh loops. The influence of the amount of cryo and relative humidity of the environment on resolution (A) and hitrate (B) was analyzed by helical mesh scans. Best diffraction and hitrates were observed in crystals with 25 % EDO and 90 % r. H.

3.4 Time-resolved crystallography to visualize the E1 decarboxylation reaction

Optimization of cryo-protection, and humidity resulted in reproducible hit rates and diffraction. A suspension of microcrystals was applied to the chip using the optimized protocol described in the previous chapter. The reaction was initiated by the addition of 100 mM pyruvate using the LAMA approach. Several time points were collected using the HARE method. For each time point, first a dark state was collected. The reaction was initiated, and the crystals were sampled after 0.2, 0.4, 1.1, 1.9, 4.8, 7.7 and 38.1 s. Due to optimization in sample delivery and humidity, all chips diffracted to 2.3-2.5 Å and showed hit rates >40%, which resulted in datasets with 100% completeness. Figure 3.8 shows the two different active sites of the E1 (labelled site A and site B) during the time course. Each active site shows the ThDP cofactor surrounded by two catalytic histidine residues His128 and His273. The 2mFo-DFc electron density map (blue) and a mFo-DFc difference map (green) is shown. The dark state shows a positive difference density above the cofactor. This density corresponds to an ethylene glycol molecule from cryo protection, which had initially been observed in the first E1-NB structures obtained. Site A shows the formation of a covalent adduct of the ThDP at 1.9s. This was indicated by the 2mFo-DFc density, which is connected to C2 of ThDP (red arrow). The signal for this density increases at 4.8 s and 7.7 s and disappears after 38.1 s. Site B shows a similar density forming after 7.7s, which also disappears after 38.1 s. The temporal differences between the formation of the covalent adduct in site A vs site B shows the half-of-the-sites reactivity of the E1. This property of the enzyme has been observed spectrophotometrically, but not yet structurally using the natural substrate pyruvate. A similar behavior was also observed in the enzyme fluoroacetate dehalogenase which was studied in a similar experimental setup [130]. Apart from these changes in the active site, no major movements were observed when structures of all time points were aligned. The low resolution at 2.3 Å, unfortunately, did not allow direct chemical interpretation of the observed densities. Decarboxylation of pyruvate involves three-atom modifications of its cofactor. To visualize these small modifications and elucidate their chemical identity, resolutions higher than 1.7 Å are needed. The E1-NB crystals already provided a robust crystallization system diffracting to 1.4 Å by classical cryo crystallography. The macro-crystals were optimized to trap decarboxylation intermediates at high resolution. High-resolution structures of reaction intermediates should help the interpretation of the density changes observed during the time-resolved experiment.

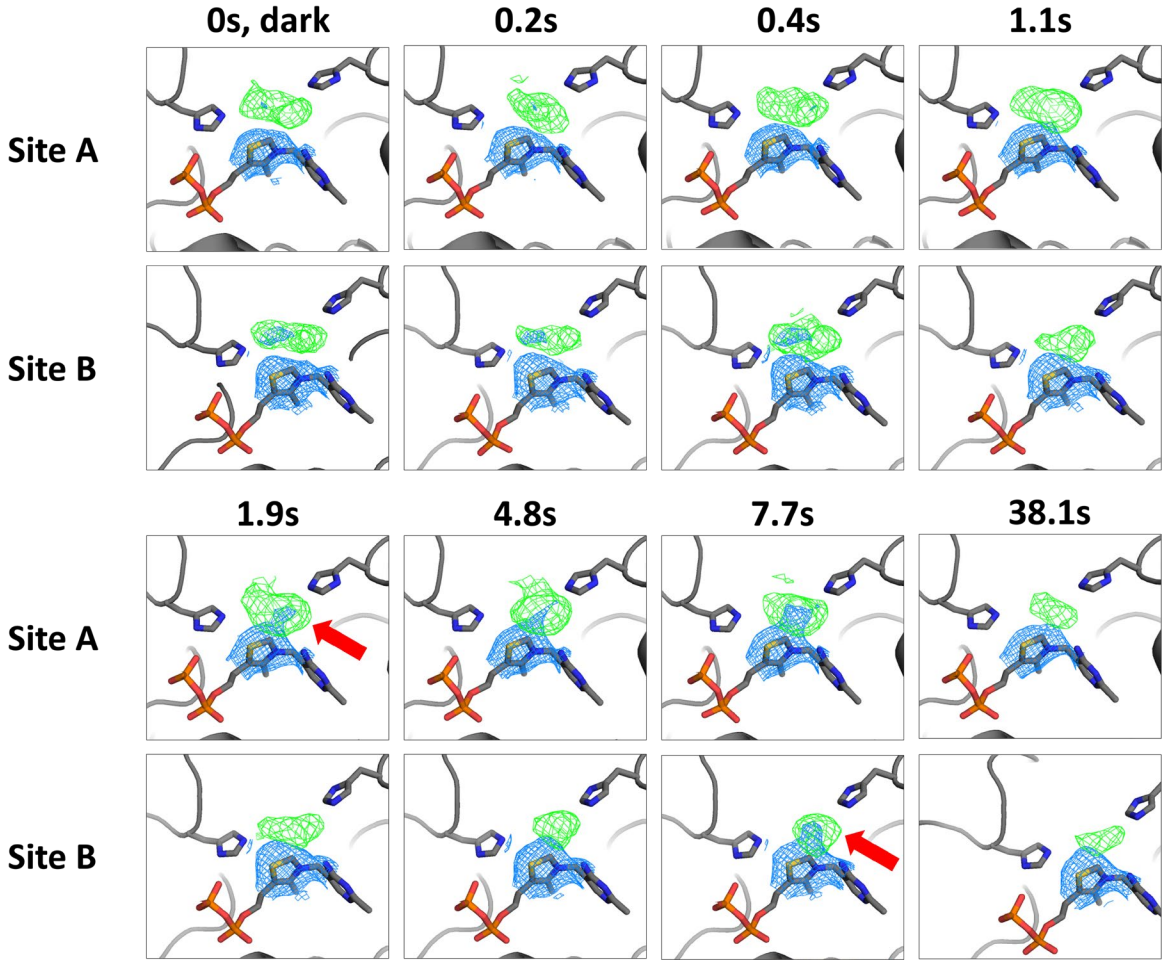

Figure 3.8: Time-resolved crystallography to visualize the E1-catalyzed decarboxylation of pyruvate. The 2mFo-DFc electron density is contoured at 1.0 rmsd, and the mFo-DFc difference map is contoured at 3 rmsd are shown for both active sites (A,B) of E1-NB over the time course of the experiment. The time delays of 0.2, 0.4, 1.1, 1.9, 4.8, 7.7 and 38.1 s are derived by the geometry of the chip according to the HARE method. A covalent intermediate forms at ThDP after 1.9 s in site A (red arrow). The density increased after 7.7 s and disappeared after 38.1 s. Active site B shows a covalent intermediate after 7.7 s, which also disappeared after 38.1 s. The resolution of the datasets ranged from 2.3-2.5 Å.

3.5 Improving crystal diffraction to high-resolution

Several methods to improve the diffraction quality of protein crystals have been reported in the literature. Simple examples are a change of cryo-protectant, and growing larger, more 3D shaped crystals [171]. Another technique to improve diffraction is crystal dehydration [172]. The effect of crystal dehydration on diffraction was evident by the microcrystal optimization described in chapter 3.3. Initially, the post-crystallization treatment was optimized by testing different cryo-protectants such as MPD, glucose and EDO (Appendix figure 3-4). Crystals cryo-protected with MPD and glucose showed anisotropic diffraction

of 0.3 Å and 0.7 Å difference amongst the different unit cell axes, respectively. In both cases, diffraction was limited to 1.6 Å. Crystals cryoprotected with EDO, on the other hand, displayed anisotropic diffraction of 0.2 Å, and resolutions higher than 1.4 Å were observed in the strongest direction. Ethylene glycol was therefore chosen as a cryo-protectant for further experiments. Next, the influence of crystal size on diffraction quality was analyzed (Appendix figure 5). Theoretically, larger crystals diffract better than smaller crystals due to a larger diffractive volume. However, the crystalline lattice is not perfect due to small long-range disorders, which are called mosaicity. Crystal mosaicity can be observed by a smear of diffraction spots. These long range disorders can be amplified by the size of the crystal [173]. Appendix figure 5 shows the diffraction patterns of a 300 µm and a 400 µm crystal cryoprotected in 20% EDO. The 300 µm crystal diffracted better and showed less mosaicity than the 400 µm crystals. This could be explained by the slower cooling rate of larger crystals in liquid nitrogen [174]. The cooling rate of crystals bigger than 300 µm is too slow, which leads to disorders in the crystalline lattice. The disorder can be observed by the mosaic spread of reflections of the 400 µm crystal. In the end, 300 µm crystals cryo-protected by a slow drop exchange from 0 to 20% ethylene glycol in 5 % steps at 18 °C diffracted to sub-Ångström resolutions. Figure 3.9A shows a 300 µm crystal grown in a sitting drop vapor diffusion plate. Figure 3.9B shows the dimensions of the X-ray beam, which fully immerses the crystal. An exemplary diffraction pattern is shown, which shows visible reflections at 1.07 Å (figure 3.9C). The high-resolution datasets were greatly facilitated by having access to large amounts of beamtime. Although the crystals reproducibly diffracted to resolutions better than 1.20 Å, a large number had to be screened to find crystals diffracting better than 1.05 Å. Other parameters contributing to the high resolution were the top-hat beam at P14, Petra III, and the new cadmium tellurite (CdTe) detector. A CdTe detector provides a high quantum efficiency at energies up to 100 keV [98]. The implementation of a data collection workflow by Global Phasing contributed to the high quality of the datasets as well. The workflow calculates the best data collection strategy based on crystal rotation and symmetry. Therefore, crystal “cusps” are avoided and datasets with high multiplicity are collected. Table 6 shows data collection statistics of a native E1-NB crystal diffracting to 0.95 Å. The high-resolution shell showed a multiplicity of 34, signal to noise ratio of 1.6 and $CC_{1/2}$ of 69.7%.

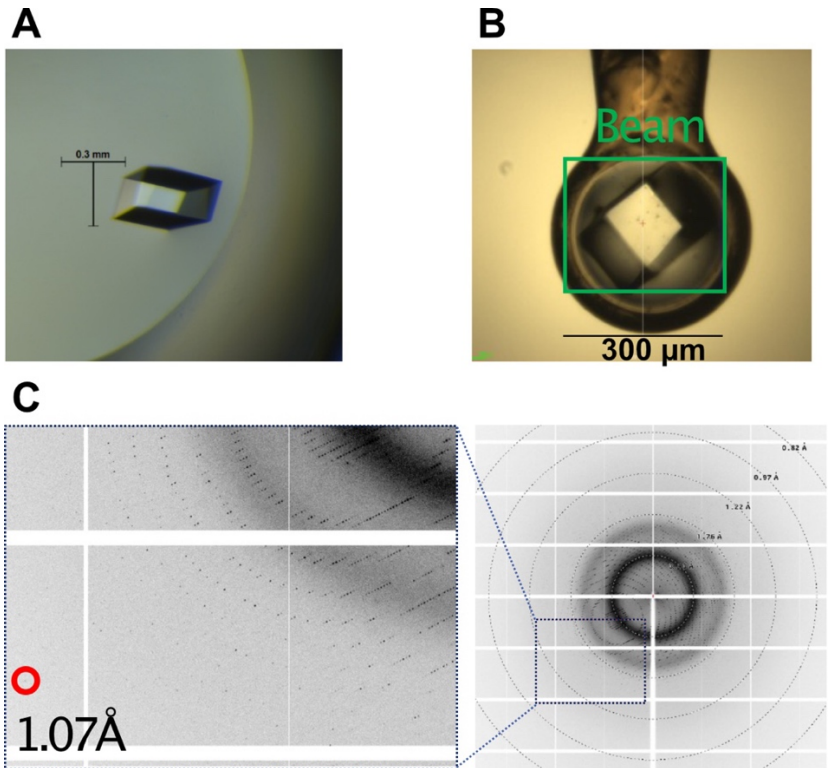

Figure 3.9: High resolution diffraction of E1-NB crystals. A) The E1-NB microcrystallization condition was modified to grow 300 µm crystals. B) The crystals are fully immersed in the X-ray beam. C) An exemplary diffraction pattern of an E1-NB crystal diffracting to high-resolution is shown. A high-resolution reflection is indicated by a red circle.

Table 6: Data collection statistics of a native E1-NB crystal

Structure	**E1-NB native**
Space group	$P2_12_12$
Unit cell	
a [Å]	185.9
b [Å]	101.8
c [Å]	86.7
α [°] β [°] γ [°]	90.0 90.0 90.0
Data collection	
Wavelength [Å]	0.465
Resolution range [Å]	50.42-0.95 (1.03-0.95)
Total reflections	29,359,087
Unique reflections	817,064
Multiplicity	35.9 (34.8)
Completeness (spherical)[%]	79.3 (18.2)
Completeness (ellipsoidal)[%]	97.3 (78.6)
Mean I/σ(I)	24.1 (1.6)
R_{pim}	0.015 (0.490)
$CC_{1/2}$	1.000 (0.697)
Refinement	
R_{work}	0.1060
R_{free}	0.1225

3.6 High-resolution structure shows geometric distortions

The native E1-NB complex diffracted to 0.95 Å, which represents the highest resolution of a PDHc E1 reported so far, and is the highest resolution attained for a 182 kDa molecule. Thus far, the highest resolved E1 structure in the PDB is the *E. coli* PDH E1 subunit in complex with the inhibitor methyl-acetyl-phosphonate (MAP)(PDB ID:2QTC) at 1.77 Å [42], and therefore the structure reported here represents an increase in resolution by 0.8 Å. The E1-NB active site showed a phenylalanine residue pi-stacked against the aminopyrimidine ring (AP) of ThDP, which keeps the cofactor in a V-shaped conformation (figure 3.10). This conformation has been observed in several thiamine diphosphate dependent enzymes [175]. The catalytic residues His128 and His273 are located near ThDP. His128 displays two alternative conformations, one conformation is in hydrogen bonding distance to a water molecule, which is located above C2 of the thiazole ring. An EDO molecule from the cryo-protection is present in the active site as well (figure 3.10A and B). The nature of the reactive state of ThDP has been proposed to be a carbanion. However, spectral and structural evidence for a stable carbene was reported in the pyruvate oxidase of *L. plantarum* [47]. As enabled by the resolution attained in this structure the E1-NB structure was refined with relaxed ThDP restraints to measure the bond lengths and angles of the cofactor. Insights into the chemical state of the cofactor could be deduced from these measurements (figure 3.10C). The bond lengths (bold numbers) and the bond lengths of the carbene form of ThDP, observed in the pyruvate oxidase crystal (PDB ID:4KGD), are shown. The C2-S1 bond is 1.73 Å long, which is comparable to 1.76 Å in the carbene. The C2-N3 bond distance, however, is 1.36 Å, which is shorter than 1.43 Å in the carbene. The shorter bond hints towards double bond character, which is evidence for the carbanion rather than the carbene form. Also, the S1-C2-N3 angle is 110.3°, which is bigger than the observed carbene angle of 107.6°. Interestingly, the C2 atom of the thiazole ring is distorted out of plane by 18° (figure 3.10D), which has so far not been reported for the E1 enzyme. Structural investigations into *Pichia stipitis* transketolase revealed similar geometries, which were explained by non-Kekulé diradicals. Some of these structures display similar out of plane distortions of the C2 atom of the thiazole ring [176]. Furthermore, The aminopyrimidine ring was distorted as well. The N4´ atom was out of plane by 6° (figure 3.10E). A similar out-of-plane distortion has previously been observed and was speculated to aid in catalysis [160].

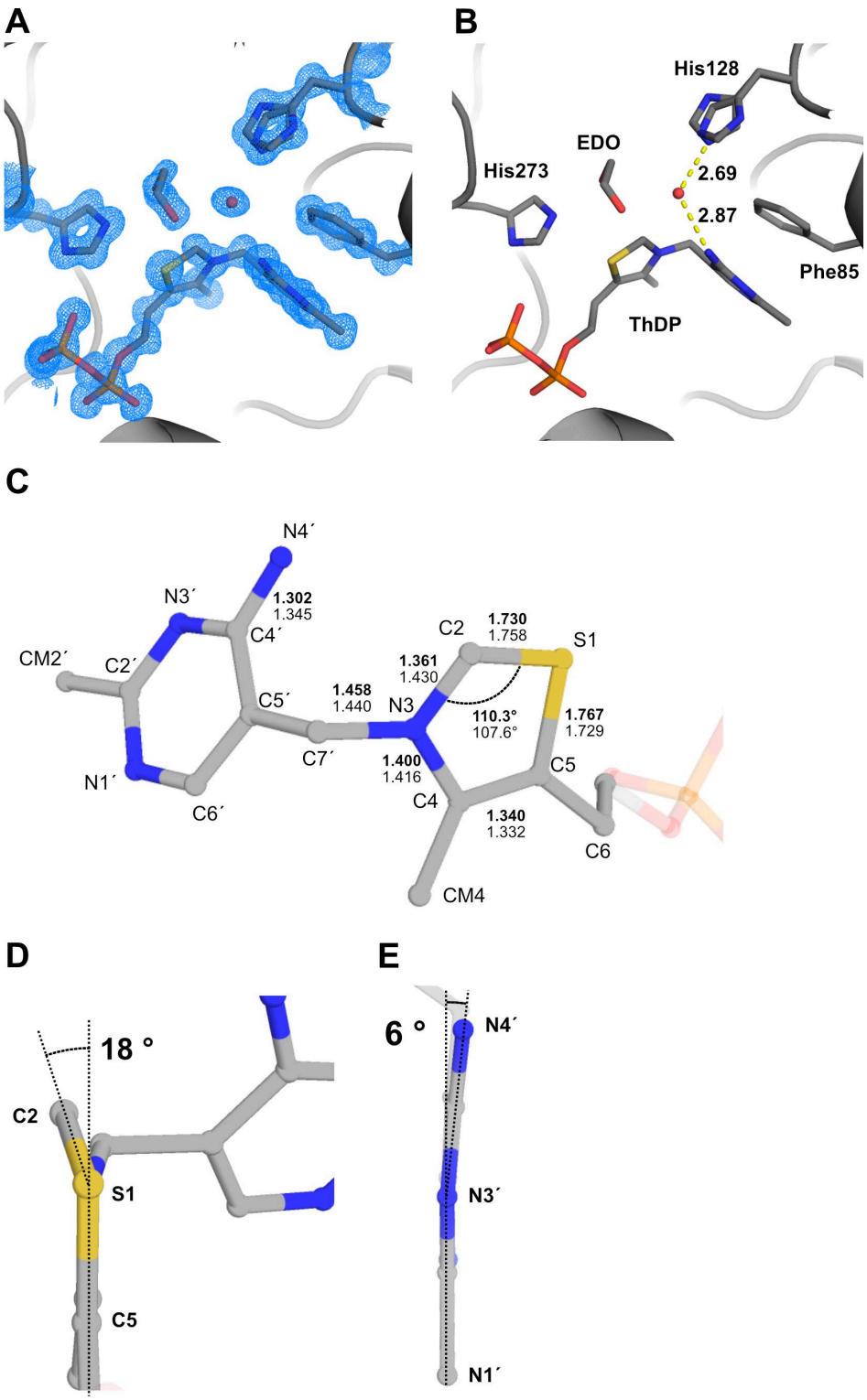

Figure 3.10: Structure of the E1 native state solved at 0.95 Å. A) The active site shows a ThDP molecule surrounded by the two catalytic histidine residues His128 and His273, a water molecule and an ethylene glycol molecule from the cryo protectant. The 2mFo-DFc electron density is contoured at 1.5 rms. B) The water molecule is coordinated by His128 and N4′ of the aminopyrimidine ring. Phe85 is pi-stacked against the aminopyrimidine ring, which keeps the cofactor in the catalytic V-conformation. C) ThDP was refined with relaxed restraints and bond distances (bold font) are compared to the bond distances of ThDP in the carbene form observed in the pyruvate oxidase (normal font). D) C2 of the thiazole ring shows an out-of-plane distortion by 18 °. E) N4′ of the aminopyrimidine ring is distorted out of plane by 6 °.

3.7 Observation of a post-decarboxylation intermediate

To capture reaction intermediates of pyruvate decarboxylation, E1-NB crystals were soaked with the substrate pyruvate. A high-resolution structure was obtained, which showed the post-decarboxylation intermediate 2-α-hydroxyethyl-ThDP at 1.03 Å resolution (figure 3.11A). The intermediate existed in two alternative conformations, evident by the spread-out electron density around the oxygen atom of the hydroxyethyl moiety. Both the enamine and carbanion form of the intermediate could be modelled. They were refined at 0.45 and 0.55 occupancy, respectively.

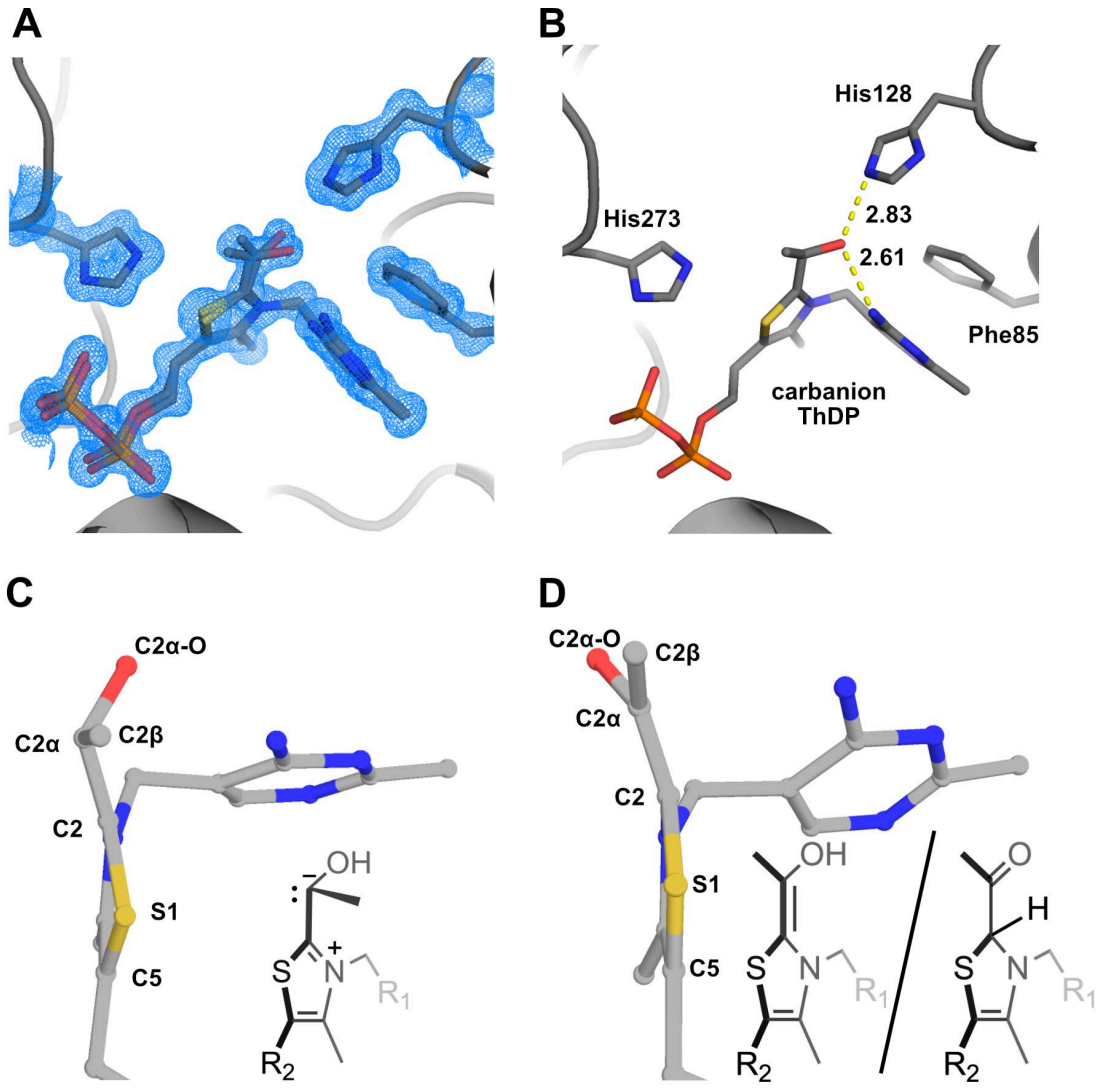

Figure 3.11: Structure of the E1 post-decarboxylation intermediate solved at 1.03 Å. A) The active site shows a covalent intermediate, which is framed by His128 and His273. The 2mFo-DFc electron density map is contoured at 1.5 rms. A mixture of two post-decarboxylation intermediates were modelled into the electron density, which are the enamine and the carbanion form. B) The hydroxyl group of the carbanion is 2.61 Å away from Nε2 of His128. It forms a hydrogen bond with N4′ of the aminopyrimidine ring. C) Side view and chemical interpretation of the suspected carbanion intermediate is shown. C2α displays a tetrahedral geometry. D) Side view and chemical interpretation of the suspected enamine is shown. The enamine and acetyl forms are shown as possible interpretations.

The hydroxyl group of the carbanion forms polar contacts with N4´ of the aminopyrimidine ring and His128. Compared to native E1, His128 exhibits only one conformation, which is flipped to orient the nitrogen towards the hydroxyl group. The methyl groups points towards the more hydrophobic region of the active site. A similar reaction intermediate has recently been reported in the pyruvate oxidase [160]. Here the covalent adduct showed a tetrahedral geometry at both C2 and C2α. In this structure, however, the electron density was interpreted as two alternative conformations of a planar enamine and tetrahedral carbanion. Figure 3.11C shows the tetrahedral geometry at C2α, which can be attributed to the carbanion or the protonated form of the carbanion. The enamine conformation (figure 3.11D) is slightly bent out of plane at C2, which contradicts the theoretical planar geometry of its double bond between C2 and C2α. The bend, and the small rotation of the 2-hydroxyethyl group with respect to the thiazole plane could hint towards the acetyl form of the post-decarboxylation intermediate, which is protonated at C2 and therefore sp3-hybridized. Chemical structures for both forms are displayed.

3.8 Trapping a pre-decarboxylation intermediate

Since short pyruvate soaks resulted in the post-decarboxylation intermediate, other ways to trap earlier reaction intermediates were devised. Conventional strategies to trap reaction intermediates in crystal structures involve sub-zero temperatures, the use of cofactor analogues or mutagenesis of catalytic residues [32,109]. The E1 contains two catalytic histidine residues: His128 and His273. His128 and His273 were substituted by asparagine, which partially mimics histidine´s geometry, but not its acid-base properties. Crystals of E1-NB, where one of the catalytic histidine residues were mutated (E1-NB_{H128N} and E1-NB_{H273N}) were soaked with pyruvate (figure 3.12).

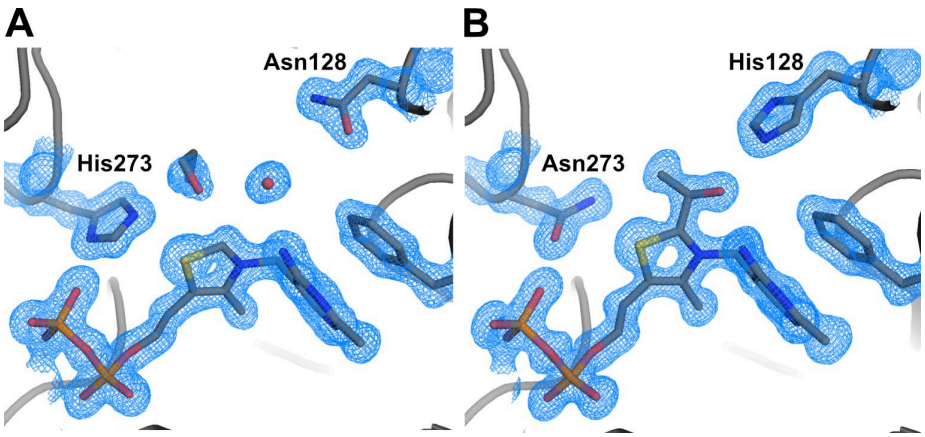

Figure 3.12: Pyruvate soaks in E1-NB_{H128N} and E1-NB_{H273N} crystals. A) Pyruvate was soaked into E1-NB crystals with H273N substitution. No covalent intermediates were observed. B) Pyruvate soak of the E1-NB H128N mutation. The structure shows the formation of the carbanion-ThDP intermediate. 2mFo-DFc electron density maps are contoured at 1.5 rms.

The resulting electron density shows that $E1_{H273N}$ can catalyze the decarboxylation reaction, since the carbanion-ThDP intermediate is visible in the active site (figure 3.12B). $E1_{H128N}$, however, does not show any covalent adduct at the C2 of ThDP. Instead, water and ethylene glycol molecules occupy the active site, just as in the native E1-NB structure. The pre-decarboxylation intermediate could not be detected in the structure. The results show that His273 is not essential for decarboxylation.

The decisive idea to trap a pre-decarboxylation intermediate was to lower both the pH, and temperature of the reaction. Acid-base catalysis is generally affected by pH changes [111]. To slow down the decarboxylation the pH was gradually lowered from 8.0 to 5.0, and the temperature was lowered to 4 °C. A short pyruvate soak successfully trapped the pre-decarboxylation intermediate lactyl-ThDP in the active site at 1.03 Å resolution (figure 3.13A). The carboxylate group is occupied at 60% in both sites and surrounded by His128 and His273. The hydroxyl group is in hydrogen bonding distance of N4´of the AP ring. The oxygen atoms of the carboxyl group form polar contacts to the nitrogen atoms of His128 and His273. His128 forms contacts to both the carboxylate and the hydroxyl group at 2.84 Å and 2.83 Å distance, respectively (figure 3.13B). The general structure of lactyl-ThDP is similar to the intermediate observed in the pyruvate oxidase from *Lactobacillus plantarum* observed at 2 Å resolution [113]. His273 and His128 are positively charged at pH 5.0, and therefore act as an electrostatic “clamp” populating the carboxylate in the active site. The structure was refined with relaxed lactyl-ThDP restraints to measure bond angles and bond lengths of the cofactor (figure 3.13C). The C2-C2α and C2α- C2β´ bond lengths are 1.51 Å, which indicates single bond character. The C2-N3 bond length is 1.39 Å. The S1-C2 bond length is 1.75 Å, indicating a single bond. The carboxyl group shows asymmetric bond lengths of the C-O bond. The bond lengths of C2β´ and O1´ and O2´ are 1.21 and 1.29 Å, respectively. This indicates protonation of O2´ by His128 (figure 3.13D). The intermediate shows several distortions. For example, lactyl-ThDP displays an out of plane distortion from the thiazole ring by 22° (figure 3.13E). Another observation is the deviation from the tetrahedral angle of 109.5° at the C2α chirality center (figure 3.13F). The C2β-C2α-C2β´ angle is 103.0°. The C2αO-C2α-C2β´ angle is 114.9°. This observation holds true for both active sites and is likely due to the electrostatic forces exerted by the positively charged histidine residues on the carboxyl group, which pulls/pushes the carboxylate towards His273. It might also indicate a strain on the C-C bond destabilizing the intermediate, since similar principles have been reported in the ThDP dependent enzyme transketolase, where a C-C bond elongation destabilizes the intermediate before C-C bond cleavage [69].

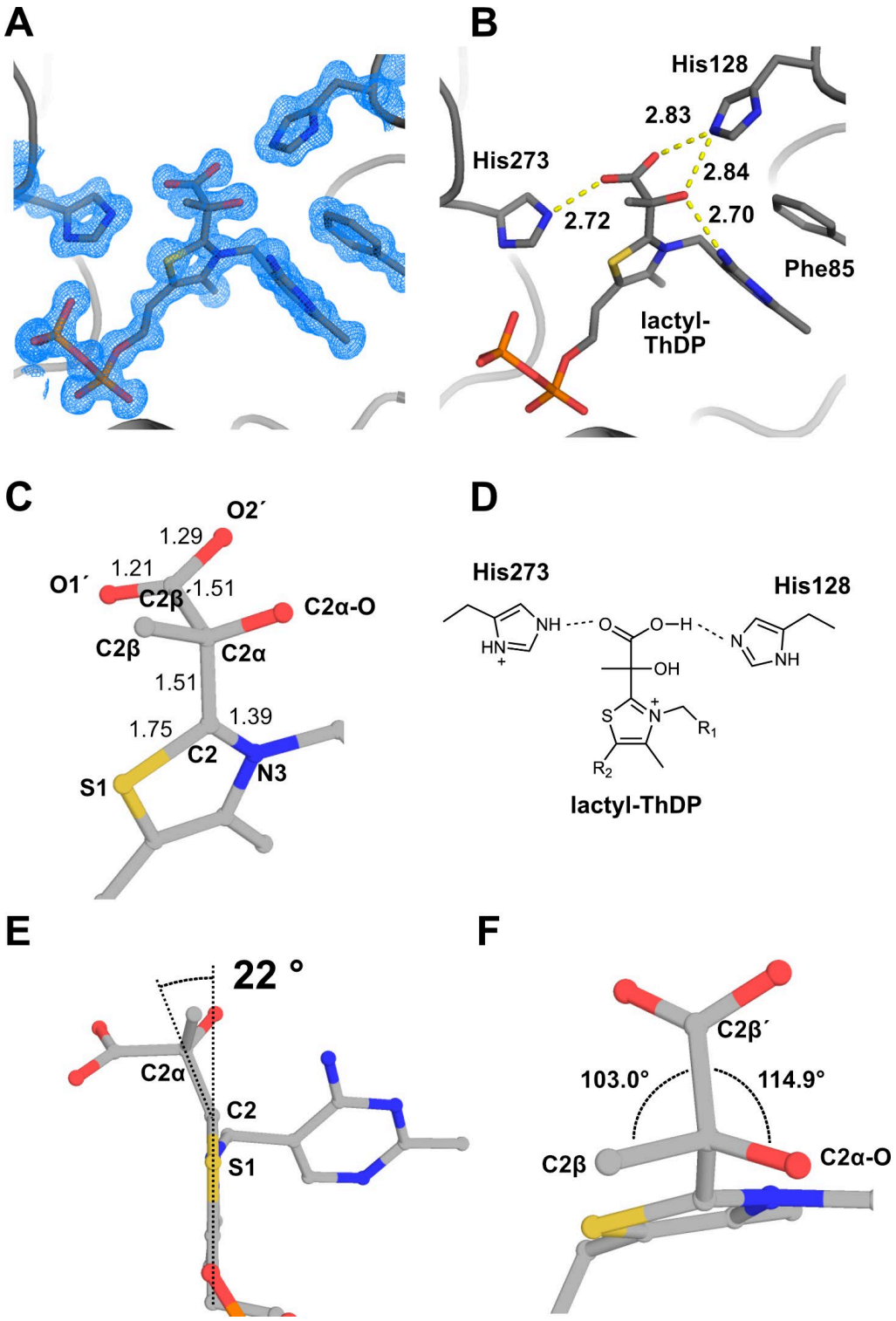

Figure 3.13: Structure of the E1 pre-decarboxylation intermediate solved at 1.03 Å. A) The active sites shows the pre-decarboxylation intermediate lactyl-ThDP. The 2mFo-DFc electron density map is contoured at 1.5 rms. Occupancy refinement showed 60% occupancy of the carboxylate group. B) The carboxyl group is framed by His128 and His273, forming polar contacts to the oxygen atoms with a distance of 2.83 Å and 2.72 Å, respectively. The hydroxyl group is in hydrogen bonding distance to N4′ of the aminopyrimidine ring. C) Bond lengths are shown after refinement with relaxed ligand restraints. D) Bond lengths of the carboxyl group indicate protonation on O2′. E) Side view of the lactyl-ThDP intermediate hightlights the out of plane distortion of the lactyl group in respect to the planar thiazole ring. F) The intermediate shows a deviation from tetrahedral geometry.

3.9 Interpretation of the time-resolved experiment

The native state, pre- and post-decarboxylation intermediates were captured at high resolution (chapter 3.6-3.8). These intermediates were refined against the time-resolved serial crystallographic data to interpret the observed densities (figure 3.14). The DARK structure shows the thiamine diphosphate cofactor in both sites. After 1.1 s, unreacted pyruvate could be modelled into active site A. At this resolution of 2.4 Å it was not possible to distinguish between pyruvate or ethylene glycol. Pyruvate is covalently bound by ThDP in active site A after 4.8 s, forming the pre-decarboxylation intermediate lactyl-ThDP. After 7.7 s, both sites show a covalent intermediate. Pyruvate was decarboxylated in site A, while site B shows the pre-decarboxylation intermediate. Both active sites are empty after 38.1 s. This could be due to hydrolysis of carbanion-ThDP at pH 8.0.

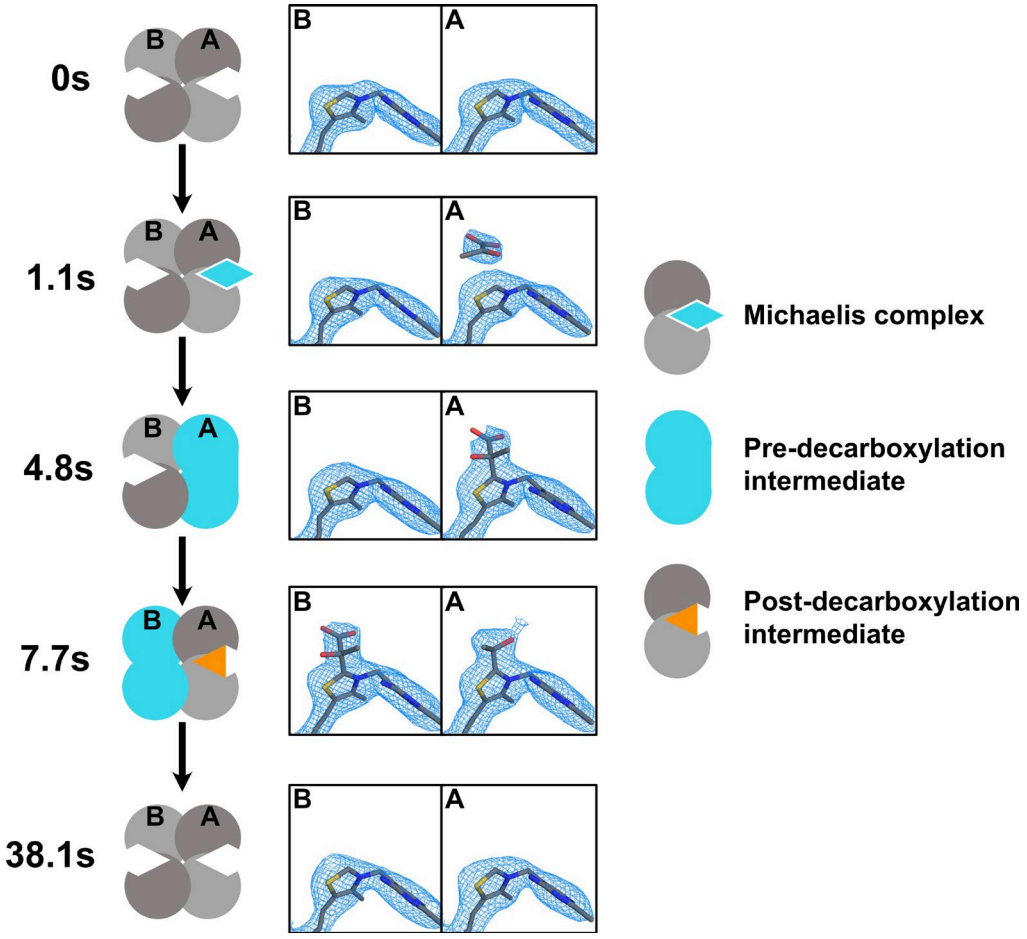

Figure 3.14: Modelling reaction intermediates into electron density maps obtained from T-REXX. Decarboxylation intermediates obtained by classical cryo crystallography were modelled into the electron density maps obtained by time-resolved serial crystallography. 2mFo-DFc maps are contoured at 1.0 rms. The reaction starts with pyruvate binding to active site A forming the pre-reaction or Michaelis complex at 1.1 s. At 4.8 s, active site A forms the lactyl-ThDP intermediate. At 7.7 s, both active sites show a covalent intermediate, which is carbanion-ThDP in site A and lactyl-ThDP in site B. After 38.1 s, no covalent intermediate can be observed, which hints at hydrolysis of the intermediates.

The TREXX experiment demonstrated the enzyme´s half-of-the-site reactivity. The same active site (A) is always one step ahead in the reaction compared to site B. Since no major structural movements could be observed, the communication is most likely mediated via the 20 Å water channel connecting both active sites. The water channel is framed by multiple acidic residues. It was shown that mutations of the acidic residues framing the channel have adverse effects on catalysis [62]. If the active sites communicate via a proton wire, evidence of protons could be found in high resolution structures. In protein X-ray crystallography, photons are diffracted by electrons of the atoms inside the crystal. Hydrogen atoms, however, contain only one electron. Therefore, high resolution structures are needed to detect hydrogens. High resolution structures were obtained for the native and lactyl-ThDP intermediate at 0.95 and 1.03 Å, which should allow the observation of hydrogen atoms in the water channel.

3.10 A proton wire connecting the active sites

To gain insights into the structural roots of half-of-the-sites reactivity, a hydrogen omit map was calculated for the E1 native enzyme, which showed the positions of hydrogen atoms for the most part of the 182 kDa enzyme complex (figure 3.15). The 2mFo-DFc map (grey) is contoured at 4.5 rms. The mFo-DFc hydrogen omit map (green) is contoured at 2.7 rms. The center of the channel is occupied by a magnesium ion, which is coordinated by six water molecules. A potential proton path is indicated by dotted lines. The path starts at N1´of site A or B, which shows a small green density indicating a protonated state. The protons follows the path via Glu59 and Gln180 to a water molecule (W1). It is not known, how the hexacoordinated magnesium affects proton transfer. Some green densities are observed between water molecules coordinating the magnesium ion, which might indicate hydrogen bonds. The proton then travels the same path over W1´, Gln180 and Glu59, which are symmetry related residues. A closer look into the ThDP–Glu59 interaction shows, that N1´atoms are protonated in both sites. Recently, indications for low barrier hydrogen bonds (LBHB) have been reported in the pyruvate oxidase and human transketolase [63]. There is no indication for LBHBs in the structures reported in this thesis, as the distances between Glu59, N´1 and Gln180 are longer than the LBHB threshold distance of 2.6 Å. In addition, the location of the green density is near the hydrogen bond donor, in this case N1´, and not equally shared between donor and acceptor as is the case for LBHBs [64]. Although the protonation of cofactors is observed in both sites, there is a difference between the N1´ proton signal in both sites. Interestingly, a closer look into the hydrogen omit map generated from the lactyl-ThDP structure contoured at 2.5 rms showed a proton asymmetry at N1´. In site B, N1´ does not show a hydrogen signal. N1´ in site A, however, displays a hydrogen signal.

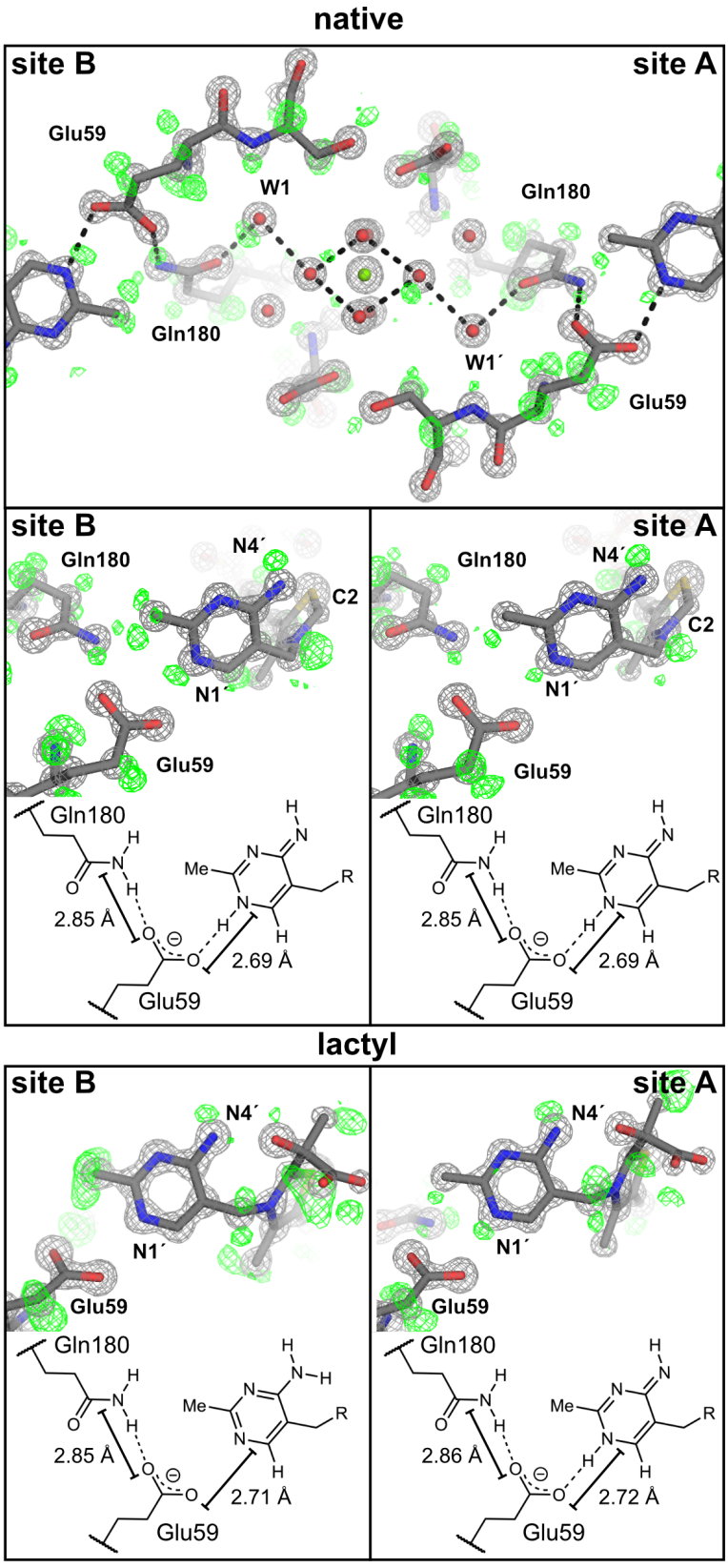

Figure 3.15: Hydrogen omit maps of the water channel. The figures show the 2mFo-DFc (grey) and the hydrogen omit difference maps (green) contoured at 4.5 and 2.7 rms, respectively. The water channel of the native E1 structure is shown. The active sites are connected by a water network with a hexacoordinated magnesium ion in the center. The water network is coordinated by mainly acidic residues such as glutamates and aspartates. A potential proton path is indicated by dotted lines, which trace the hydrogen signal of the hydrogen omit map from site A to site B. A zoom into both active sites shows the interaction of conserved residue Glu59 with N1´ of the aminopyrimidine. Both cofactors are protonated at N1´. The hydrogen omit map of the E1 lactyl-ThDP intermediate shows an asymmetric protonation of the cofactors at N1´.

N4´ in site A shows one hydrogen and is therefore in the imine form. N4´ in site B shows two densities indicating two hydrogen atoms, which can be interpreted as the amine form. These observations illustrate substrate mediated ThDP protonation asymmetry, which might be a driving factor in half-of-the-sites reactivity.

3.11 E1 inhibition mechanism

The previous section of this thesis has illustrated, how two powerful structural approaches, conventional cryo-crystallography and time-resolved serial crystallography, complement each other to resolve intermediates of pyruvate decarboxylation. The full reaction cycle of the E1, however, involves a second reaction, i.e., reductive trans-acetylation. Structural details of reaction intermediates of reductive trans-acetylation have not been elucidated so far. Several reaction mechanisms have been proposed. One of them involves a concomitant electrophilic and nucleophilic attack from the enamine on the disulfide of the dithiolane ring [54]. Another mechanism involves a two-step process with oxidation of the carbanion/enamine-ThDP tautomer to acetyl-ThDP and subsequent attack of a lipoamide thiolate at the ketone carbon of the acetyl group [52]. One argument for the two-step acetyl hypothesis is the observation that acetyl-ThDP can act as substrate in the *E. coli* PDHc. This was shown in enzymatic assays using the pyruvate analogue fluoropyruvate [177]. Fluoropyruvate resembles pyruvate but contains a fluorine atom attached to its methyl group (figure 3.16). The postulated mechanism of action is that departure of the fluorine leaving group leads to formation of acetyl-ThDP [177]. Another paper by the same group reports inactivation of the PDHc by fluoropyruvate [49]. To gain structural insights into the inhibition/reaction mechanism of E1 with fluoropyruvate, fluoropyruvate was soaked into E1-NB crystals and the structure was solved at 1.5 Å resolution (figure 3.17A). Unexpectedly, no acetyl-ThDP was visible. Instead, the active site showed the formation of a seven-membered ring connecting the five-membered thiazole ring with the six-membered aminopyrimidine ring (figure 3.17B). This tricyclic form (carbinol-ThDP) , also termed carbinolamine, has been observed by spectrophotometric methods and NMR, for example during chemical synthesis of acetyl-ThDP, but structural details have not yet been elucidated so far [178], [179].

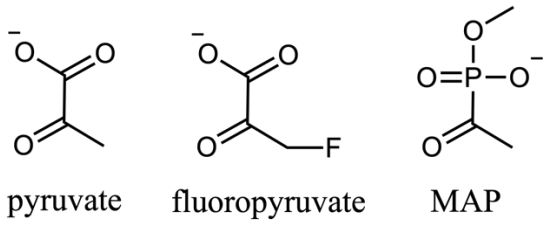

Figure 3.16: Structures of pyruvate and pyruvate analogues. The chemical structures of pyruvate and the PDH E1 inhibitors fluoropyruvate and methyl-acetyl phosphonate (MAP) are shown. Fluoropyruvate contains an additional fluorine atom at the methyl group. MAP contains a phosphonate group instead of the carboxyl group.

The only structural information about tricyclic ThDP stems from two crystal structures of other ThDP dependent enzymes, which all show the formation of a six membered ring [179,180]. Carbinol-ThDP still displays a V-shaped conformation. His128 is 3.3 Å away from the hydroxyl group. The bond lengths were measured to give evidence about the chemical nature of this intermediate (3.17C). N4´ of the AP ring formed a covalent bond with C2α of the hydroxyethyl group after decarboxylation. The fluorine atom is not observed in the structure signifying that it has undergone elimination. The N4´ - C2α bond length is 1.47 Å, and the C2 - C2α bond length is 1.50 Å, indicating single bond character. C2α is sp3 hybridized and therefore displays tetrahedral geometry. The C4´-N4´ bond length is 1.37 Å, which indicates a partial double bond character, probably due to resonance stabilization with the AP ring. Figure 3.17 D shows the chemical interpretation of tricyclic ThDP.

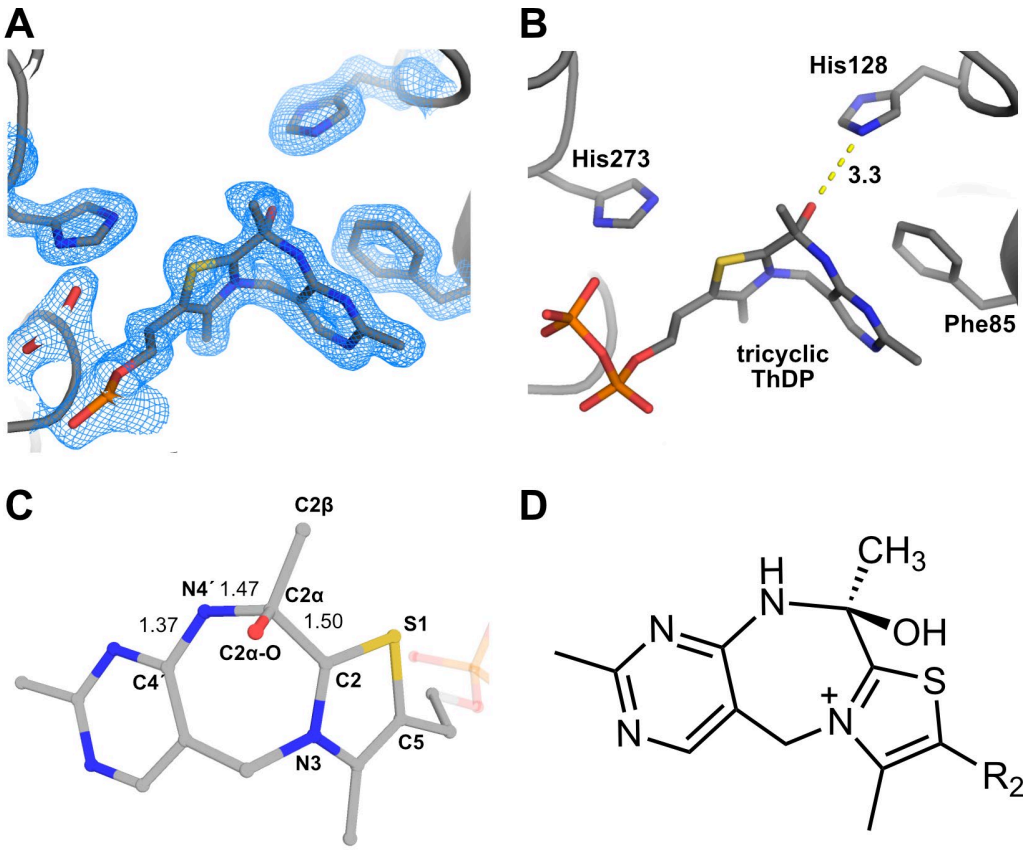

Figure 3.17: Structure of the E1-fluoropyruvate inhibition complex resolved at 1.5 Å. A) The 2mFo-DFc electron density map is contoured at 1.5 rms. The active site shows the formation of a tricyclic ThDP. B) Tricyclic ThDP is still present in the V-conformation. The hydroxyl group is 3.3 Å away from His128. C) The tricyclic structure consists of the six-membered amino pyrimidine ring and the five-membered thiazole ring, which are connected by a seven-membered ring formed by N4´ of the AP ring and C2α. Bond lengths indicate single bond character of N4´-C2α and C2-C2α (D).

Another potent inhibitor of the PDH E1 enzyme is methyl-acetyl-phosphonate (MAP) (figure 3.16). MAP is a pyruvate analogue, which mimics the pre-decarboxylation state. It contains a phosphonate group instead of the carboxyl group, which makes it unable to be decarboxylated. MAP was soaked into the crystals and the structure was solved at 1.2 Å resolution. The active site shows covalent hydroxyethyl phosphonate ThDP (HEP-ThDP) molecule (figure 3.18A). The phosphonate group points towards the exit of the active site and is coordinated by the two catalytic histidine residues His128 and His273, similar to the carboxylate in the lactyl-ThDP intermediate (figure 3.18B). MAP has been soaked into multiple ThDP dependent decarboxylases because it mimics a stable pre-decarboxylation intermediate. In *E. coli*, a MAP soak lead to structural rearrangement of an active site loop [42]. No movements were observed in the *B. subtilis* E1. The chemical interpretation of HEP-ThDP is shown in figure 3.18C.

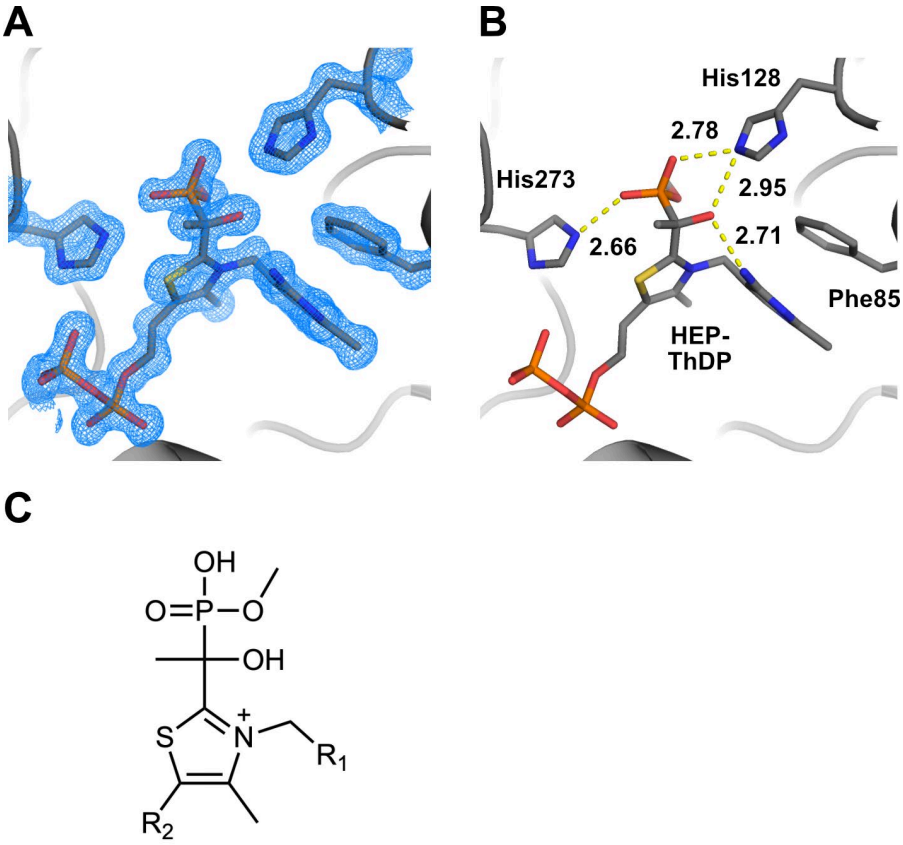

Figure 3.18: Structure of the E1-MAP inhibitor complex solved at 1.2 Å. A) The active site shows the formation of a covalent hydroxyethyl-phosphonate ThDP (HEP-ThDP) adduct. The 2mFo-DFc electron density map is contoured at 1.5 rms. B) The phosphonate group is in hydrogen bonding distance to both catalytic histidines. The hydroxyl group forms polar interactions with N4′ of the AP ring. C) Chemical interpretation of HEP-ThDP.

3.12 Substrate specificity in 2-oxoacid dehydrogenase complexes

E1 subunits from related dehydrogenase complexes, such as the branched-chain α-ketoacid dehydrogenase (E1b) and oxoglutarate dehydrogenase (E1o), catalyze the decarboxylation of larger α-ketoacids than the PDHc E1 (E1p) substrate pyruvate (figure 3.19). The substrates for E1b are α-keto-methylvalerate (MVA), α-keto-isovalerate and α-keto-isocaproate (CAP) [8]. The substrate for the E1o is 2-oxoglutarate (OXO) . While the E3 is shared amongst different dehydrogenase complexes, the respective E1 and E2 subunits are specific to their complex [17]. However, enzymatic assays showed that E1p of *B. stearothermophilus* can decarboxylate E1b and E1o substrates [181]. To gather structural information about PDH substrate specificity, MVA, CAP and OXO were soaked into E1-NB crystals and reaction intermediates were obtained at 1.1 Å (figure 3.20). Only the E1b substrates MVA and CAP showed a covalent adduct at ThDP C2 (figure 3.20A and B). A broadened density around the hydroxyl group is seen which corresponds to the same tautomeric enamine-carbanion equilibrium observed in the pyruvate post-decarboxylation intermediate.

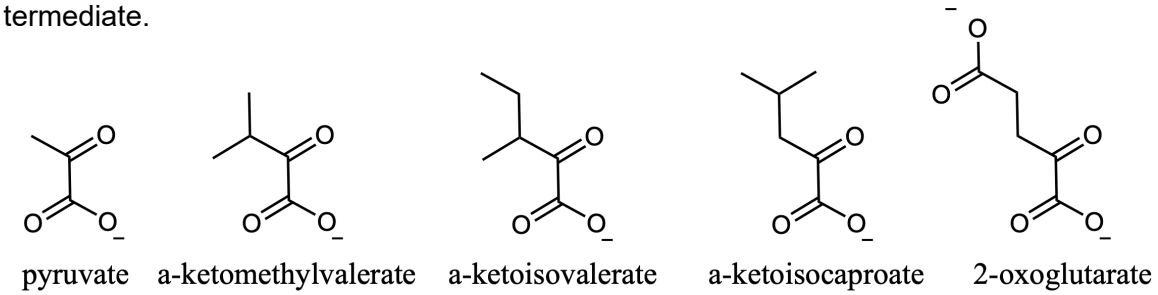

Figure 3.19: Substrates of different 2-oxoacid dehydrogenase complexes. The natural substrates of the PDHc, BCDHc and ODHc are shown. Similarities are a carboxyl group and the ketone group in α-position. BCDHc substrates contain hydrophobic substituents at the methyl group, while 2-oxoglutarate contains a carboxyl group.

The E1 incorporates these unnatural substrates by small movements of hydrophobic side chains surrounding the active site (figure 3.20C). The pyruvate post-decarboxylation intermediate carbanion-TPP (grey) is overlayed with the post-decarboxylation intermediates of the BCDH substrates (orange and blue). Two prominent residues display movements: Ile144 moves its side chain upwards in the MVA structure to incorporate the propylene group, keeping a distance of 3.59 Å. In the CAP structure, however, Ile144 does not move much compared to the pyruvate structure. Phe76 moves its benzene ring sideways to make room for the propylene group of the caproate group which results in a distance of 3.15 Å between the propylene group and Cε of Phe76. The soak with OXO does not show any covalent intermediate. The BCDHc substrates are similar to pyruvate in respect to their hydrophobic group which is accommodated in the hydrophobic pocket provided by the

PDHc E1 during catalysis. In contrast, 2-oxoglutarate contains a negatively charged carboxyl group, which probably hinders proper orientation of the substrate for catalysis. The carbanion-enamine tautomerism shows that this tautomeric equilibrium is still present for substrates other than pyruvate. It would be interesting to know whether the acyl-group of these intermediates can be transferred to the E2 by the lipoyl group of the PDHc. However, lipoamide soaks in the E1 were not successful. This was not surprising, since the lipoyl group is naturally covalently linked to the lipoyl domain of the E2, and free lipoamide is a very poor substrate for the E1 [141,182]. However, both E2 and E3 accept free lipoamide in enzymatic assays [183,184]. Thus far, there is no structural evidence of the lipoyl group in the active site of the E1 and E3, and lipoamide-E2 structures are poorly resolved.

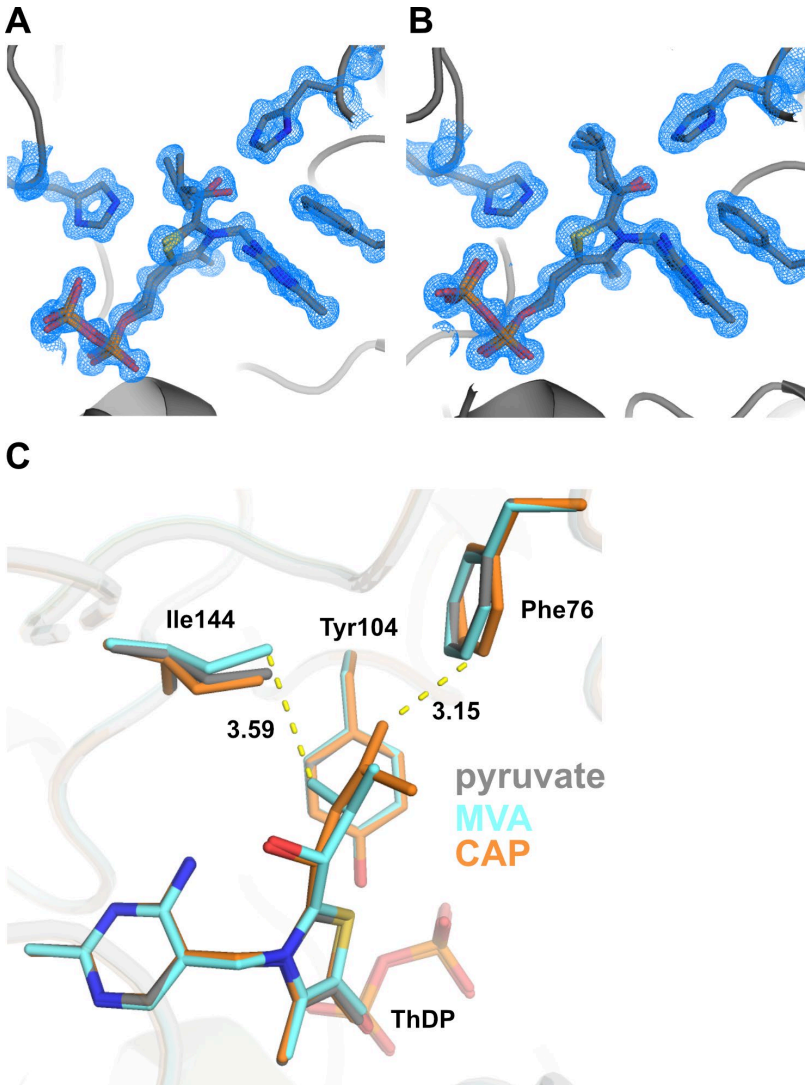

Figure 3.20: Structure of the E1 soaked with MVA and CAP solved at 1.05 and 1.2 Å. The active site shows a tautomeric equilibrium between the enamine and carbanion form of the post-decarboxylation intermediate of MVA (A) and CAP (B). The 2mFo-DFc maps are contoured at 1.5 rms. C) The carbanion form of the intermediates are overlayed with the carbanion form of pyruvate after decarboxylation. Binding of MVA and CAP led to small structural changes of surrounding residues such as Ile144 and Phe76.

3.13 Lipoamide binds a hydrophobic channel in the E2

The overall PDHc reaction is catalyzed by three different enzymes. The E1 enzyme decarboxylates pyruvate, and transfers the acetyl group to the lipoyl arm of the E2 subunit lipoyl domain. The lipoyl domain transfers the acetyl group to the E2 active site to convert CoA into acetyl-CoA. Insights into the decarboxylation reaction, and chemistry of the thiamine cofactor of the E1 enzyme have been gathered in the previous part of this thesis. Several E2 structures have been solved by X-ray crystallography and cryo-EM, but so far the resolution was limited to 2 Å for the catalytical domain, and 2.6 Å in structures of the full core [20,82,86,87]. The aim was to investigate the E2 catalytic domain trimers (E2CD) in isolation, and solve a high resolution structure in complex with lipoamide. The E2 polymerizes into either cubic, which consist of 24 subunit copies, or icosahedral assemblies of 60 subunits, respectively. To gather high resolution structural data of the E2 active site, the catalytic domain alone was cloned, and purified. A study showed that polymerization into the dodecahedral core is enabled by a C-terminal sequence and deletion of the sequence disrupted core assembly [20]. The C-terminal nine amino acids of the *B. subtilis* PDH E2 (AA202-442) were deleted, and the E2CDΔ9 was expressed recombinantly and purified via Ni-NTA chromatography and gel filtration (figure 3.21). The E2 eluted from the size exclusion column around 230 ml, which matches the expected 75 kDa weight of the E2 trimer and is therefore not polymerized into the full core. The band corresponding to E2 runs at around 25 kDa in the SDS-gel.

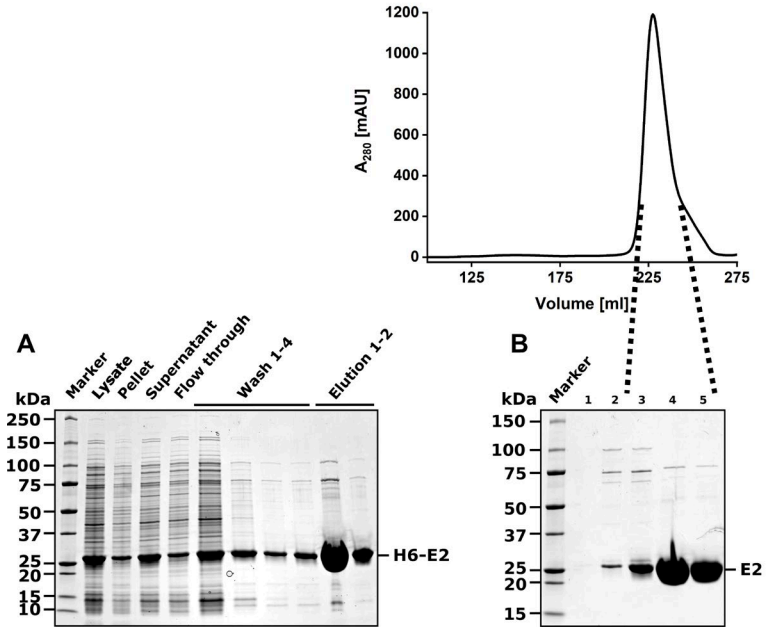

Figure 3.21: SDS-PAGE analysis of the E2 trimer purification. The E2 catalytic domain trimers where purified by Ni-NTA chromatography (A) followed by size exclusion chromatography (B). Fractions in the chromatogramm analyzed via SDS-PAGE are indicated with dotted lines. The E2 runs at around 25 kDa. The chromatogramm shows a peak with a small shoulder, which was excluded from the purification.

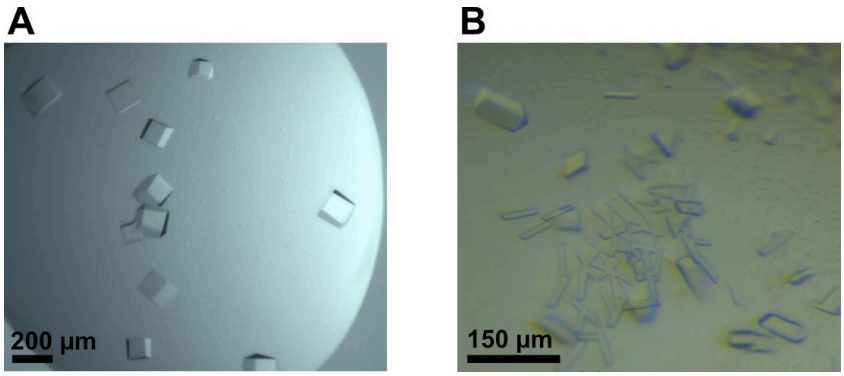

Figure 3.22: Crystals of the E2 catalytic domain trimers. Crystals of the E2 CD trimer were obtained in a salt-based (A) and PEG-based (B) crystallization condition.

E2CD was crystallized in a salt-based, and PEG-based crystallization condition (figure 3.22). In the salt-based condition they crystallized in space group I23 with unit cell parameters a=117.6 Å, b=117.6 Å, c=117.6 Å, α=90.0°, β=90.0°, γ=90.0°. The PEG-based crystals grew in space group $P2_1$ with unit cell parameters a=72.1 Å, b=164.0 Å, c=73.1 Å, α=90.0°, β=118.2°, γ=90.0°, and two trimers in the asymmetric unit. The salt-based crystals diffracted to resolutions up to 1.08 Å and the asymmetric unit contained one monomer. Initial substrate soaks with reduced lipoamide were not successful because of the low solubility in the high-salt crystallization condition. A pegylated lipoamide derivative (Lipoamide-dPEG-(4)-OMe) was utilized to increase the solubility in the polar crystallization condition (figure 3.23). The lipoamide derivative was reduced by TCEP to mimic the reduced state after reductive trans-acetylation and soaked into the crystal overnight. Two datasets were collected, with either ethylene glycol (EDO) or glycerol (GOL) as cryo protectant. In both soaks, each monomer was binding lipoamide in a channel, which is located near the three-fold axis of the trimer (figure 3.24A). The hydrophobic entry channel is formed by two valine, one isoleucine, and one methionine residue (figure 3.24B).

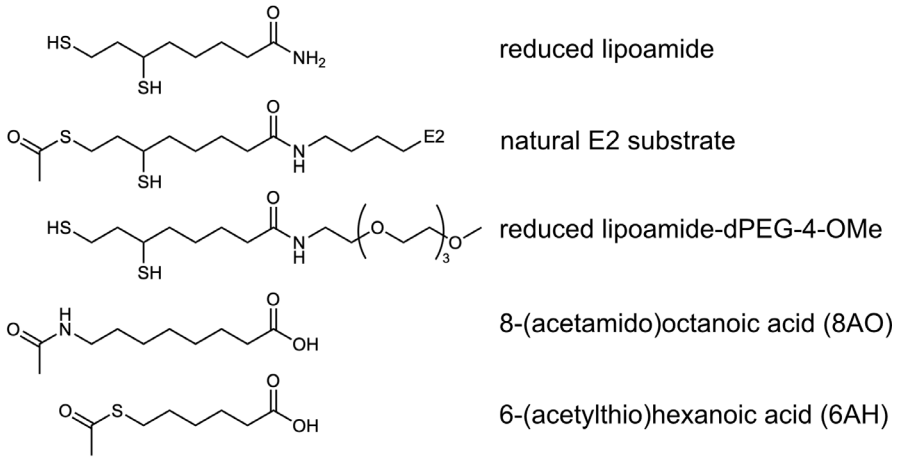

Figure 3.23: Chemical structures of lipoamide derivatives. The natural substrate of the E2 is acetylated lipoamide attached to a lysine residue of the LD. Lipoamide-dPEG-4-OMe is a soluble derivative, which mimics the reduced state after reductive acetylation. 8AO and 6AH are acetylated lipoic acid mimics.

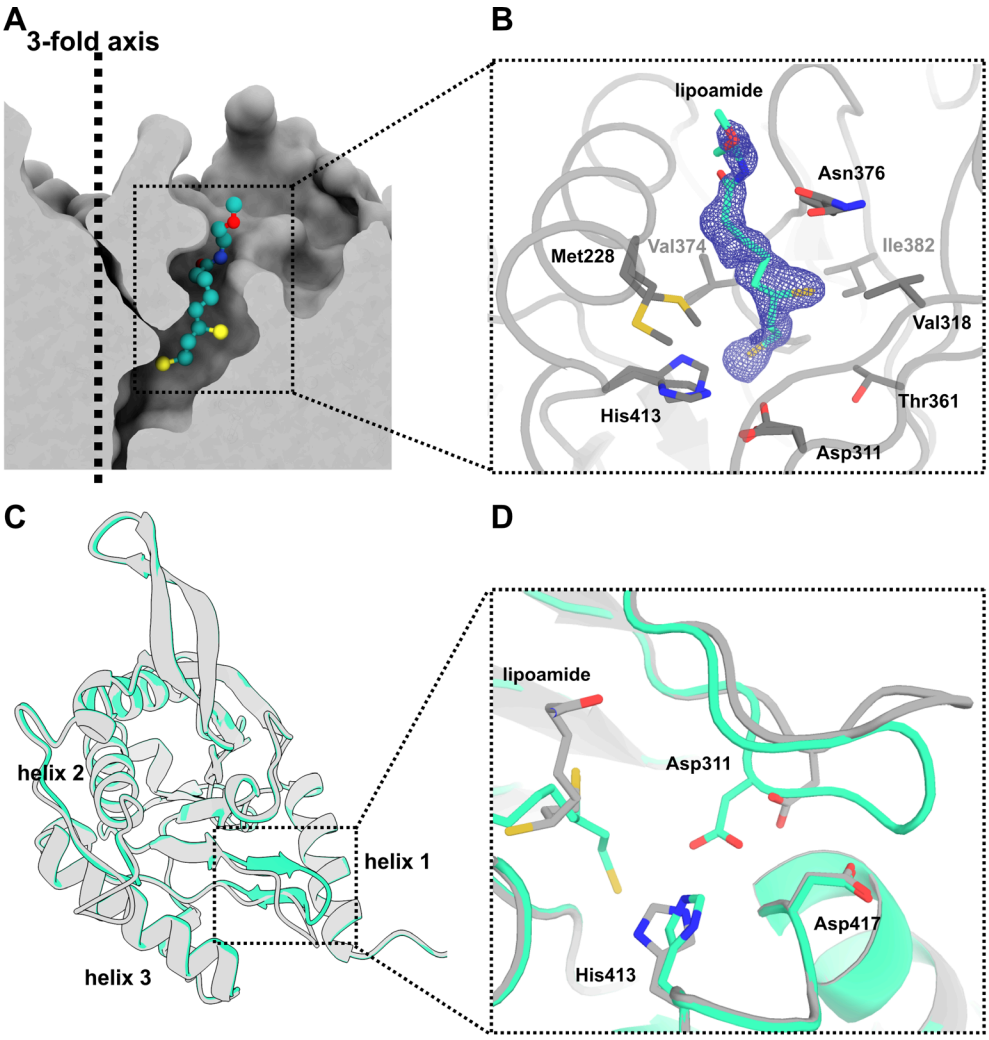

Figure 3.24: Structures of the E2 lipoamide complex solved at 1.08 Å. A) Lipoamide (green) resides in a hydrophobic channel formed by two monomers of the trimer. The channel is close to the trimeric threefold axis. B) The channel is formed by several hydrophobic residues. 2mFo-DFc electron density map is contoured at 1.0 rms. Lipoamide S6 points towards a hydrophobic gap formed by Ile382 and Val318. S8 points towards the catalytic His413. Lipoamide and several residues are present in two alternative conformations. Only the higher occupancy conformation of lipoamide is depicted here (60%). C) Two conformations of a loop can be observed for crystals cryo-protected with GOL (grey) and EDO (green). In crystals cryo-protected with EDO, the loop adapts a closed conformation, which brings an aspartate residue in proximity to the catalytic His413 (2.7 Å). The previously proposed catalytic residue Asp417 points away from the active site.

The active site is formed by the catalytic residues His413 and Thr316. PEGylated reduced lipoamide was present in multiple alternative conformations. The most occupied conformation (60%) is shown here. S6 of the reduced lipoamide points towards a pocket formed by Val318, Ile382 and Asn376. S8 is pointing

towards the catalytic His413, whereby the S-N distance is 3 Å. E2CD in crystals cryoprotected with ethylene glycol displayed rearrangement of a loop region, whereby E2CD crystals cryoprotected with glycerol did not (3.24C). The loop connects a β-sheet located in the middle of helix 1, 2 and 3 of one monomer. The ethylene glycol structure is displayed in

green; the glycerol structure is displayed in grey. The lipoamide show different conformation in the glycerol structure, where it is further away from the active site. S6 of the lipoamide in the EDO soak (green) and S8 in the GOL soak (grey) occupy the same position. In the EDO structure, the reduced lipoamide is located in proximity to His413. Loop closure brings an aspartate residue (Asp311) in proximity (2.7 Å) to the catalytic histidine His413 (figure 3.24D). The residue Asp417, which is suggested to take part in the catalytic dyad, is pointing away from His413 in both structures [140]. Reduced lipoamide is only a mimic of the natural E2 substrate, which is S8-acetylated lipoamide (figure 3.23). Therefore, the acetylated lipoamide analogues 6-(acetylthio)hexanoic acid (6AH) and 8-(acetamido)octanoic acid (8AO) were soaked into the salt-based E2 crystals to elucidate the interaction of the acetyl group with active site residues. 8AO was kindly synthesized and provided by Cromarte Rogers (group of Arwen Pearson, University of Hamburg). Unfortunately, 8AO was not observed in the structures. 6AH was observed binding to an unexpected site (figure 3.25). The thioester was located near catalytic His413, but was binding from the outside of the lipoamide channel. Arg221 adapts a different conformation in the 6AH structure, which sits in hydrogen bonding distance to the carbonyl oxygen of the thioester. 6AH is only partially occupied and shares its position near His413 with an ethylene glycol molecule depicted in black.

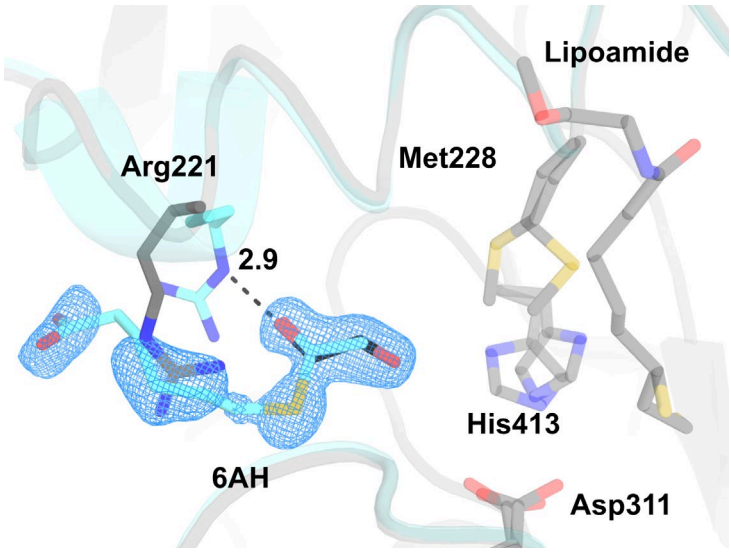

Figure 3.25: Structure of E2 complexed with 6AH solved at 1.13 Å. 6AH is binding to a pocket near His413 outside the lipoamide channel. The 2mFo-DFc electron density map is contoured at 0.9 rms. 6AH is present in 40% occupancy. A EDO molecule is occupying the site in 60 % occupancy. Arg221 is moving away upon binding of 6AH.

The full acetyl transfer reaction involves the cofactor CoA. Unfortunately, soaks with both reduced lipoamide and CoA were not successful since the CoA binding site was blocked by a crystal contact in the salt-based crystallization condition (figure 3.26). The long flexible N-terminus of a neighboring molecule extended into the CoA binding site.

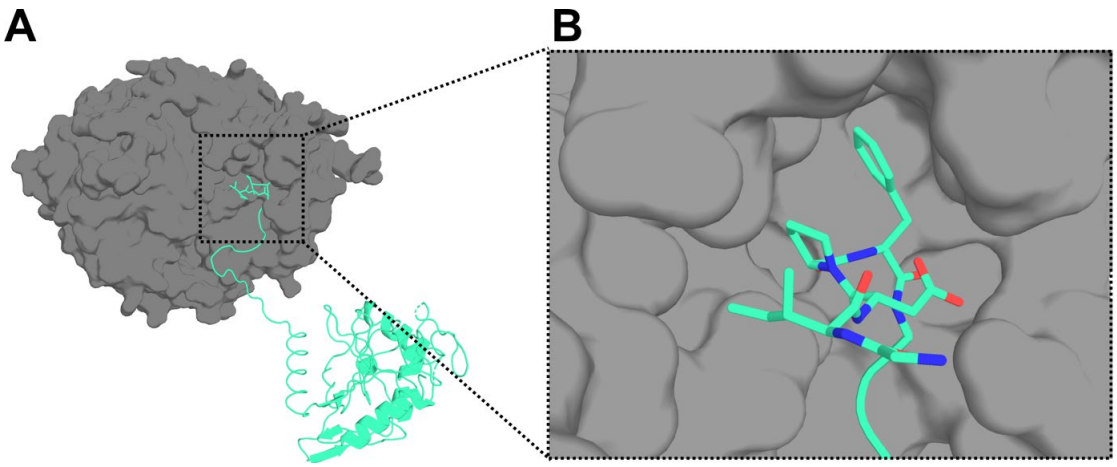

Figure 3.26: The CoA binding site is blocked by a crystal contact. A) The N-terminus of a neighbouring E2 monomer binds to the CoA binding site and therefore mediates a crystal contact. B) The N-terminal sequence GIDPFT forms a loop structure, which pushes a proline and phenylalanine residue into a hydrophobic pocket of the CoA binding site.

Binding is mediated by a secondary structure formed by the sequence GIDPFT, which places a phenylalanine and proline residue into the hydrophobic pocket. The sequence is not part of the E2, but part of a six amino acid long extension from the expression vector remaining at the N-terminus after cleavage of the hexahistidine-tag. Since the CoA binding site was blocked in the salt-based crystals, crystals of the PEG-based crystallization condition were soaked with CoA and crystals diffracted to 1.9 Å resolution. However, soaks with both reduced lipoamide and CoA resulted in dissolution of the crystals. CoA bound to all three monomers of the trimer (figure 3.27A). The adenine part of CoA forms two hydrogen bonds with Asn362. The 3´-phosphate forms polar contacts with Arg253. The β-mercaptoethylamine arm extends into the active site placing the sulfur atom in proximity to H413, termed “in-conformation”, which has been observed in other E2CDs [140]. Thr361 and Asp311 guide the arm towards His413 by forming hydrogen bonds with the backbone carbonyl and nitrogen of the β-mercaptoethylamine arm. The terminal sulfur atom is 4.5 Å away from His413. To analyze the position of the reduced lipoamide in relation to CoA, the position of CoA from the PEG-based crystals was modelled into the salt-based crystals soaked with reduced lipoamide and ethylene glycol. Both structures were aligned (figure 3.27 E). The sulfur atom of CoA is 3.8 Å away from the S8 of the reduced lipoamide. The aspartate residue in contact with His413 would be too close to the CoA arm. Therefore, the

loop would most likely have to reorder when CoA enters the active site. These data indicate, that a similar loop gating mechanism, as postulated for BCDHc E2, is also present in the icosahedral E2 of the PDHc [86].

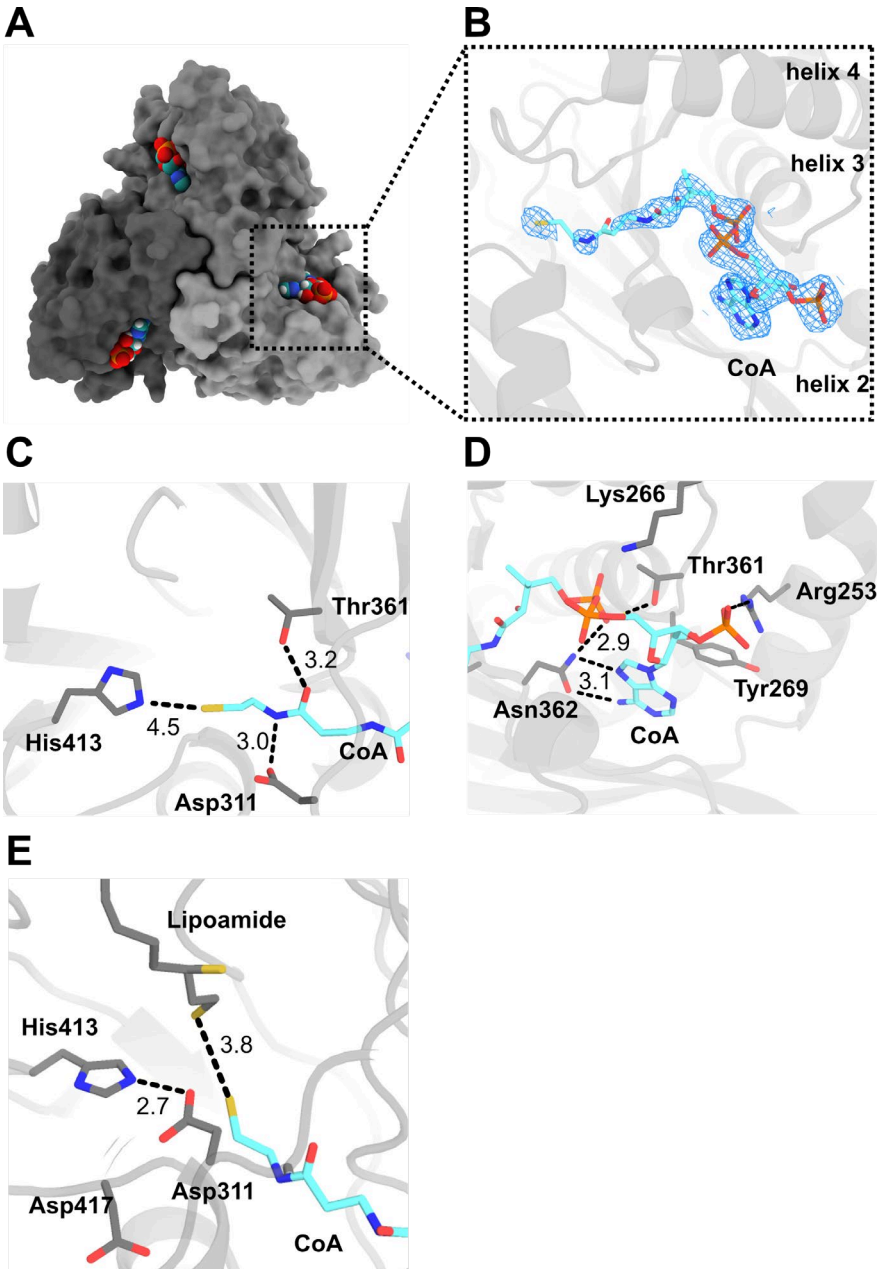

Figure 3.27: Structural details of CoA binding at 1.9 Å resolution. A) CoA binds all three subunits of the trimer close to the interface between two monomers. B) The binding site is located near helices 2,3 and 4 of one monomer. The 2mFo-DFc electron density map is contoured at 1.0 rms. C) The β-meracapto arm is positioned towards His413 by Thr361 and Asp311, which interact with the ketone oxygen and nitrogen atom of the backbone. The CoA-S-N-His distance is 4.5 Å. D) The adenine part of CoA is bound by ionic interactions of the phosphates with Arg253 and Lys266. The adenine base forms two hydrogen bonds with Asn362. E) The position of CoA (cyan) is overlayed with the salt-based crystal structure soaked with lipoamide. The CoA thiol is 3.8 Å away from lipoamide S8. The positioning of CoA would lead to clashes with Asp311 in the loop. Therefore, the loop is probably reordered upon CoA binding.

Furthermore, a new partner for the catalytic dyad is proposed (Asp311 instead of Asp417). Further kinetic data is needed to support this hypothesis. As soaking lipoamide was successful to probe the E2-lipoamide interaction, a similar strategy was pursued for the E3 subunit of the *B. subtilis* PDH complex.

3.14 Observation of a mixed lipoamide disulfide in the E3 active site

The E3 catalyzes the reversible oxidation of dihydrolipoamide under reduction of NAD^+. The reaction mechanism follows the general mechanism of FAD and NADH dependent reductases, such as the glutathione reductase, which is a thiolate-disulfide electron shuttle. The E3 contains two cysteine residues forming a disulfide bridge in the active site, which mediates the thiolate-disulfide exchange (Cys47 and Cys52) [185]. No structural information of the E3-lipoamide interaction has been elucidated so far. To trap the lipoamide in the active site, one of the catalytic cysteines was mutated to a serine residue ($E3_{C52S}$). The hypothesis was, that the mutation disrupts the thiolate-disulfide electron shuttle and traps the lipoamide in the active site via disulfide formation. Cys52 was chosen as the point of mutagenesis over Cys47, since Cys47 is closer to the putative lipoamide channel in the human E3 and is therefore more likely to take part in the interaction with lipoamide [89]. The native and mutated *B. subtilis* PDH E3 enzymes were purified as described for the E2 subunit (Appendix figure 1). Both crystallized in a condition containing 2.2 M ammonium sulfate, 0.15 M imidazole malate pH 8.5 and 1% (v/v) glycerol.

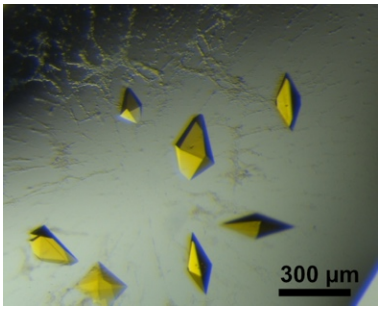

Figure 3.28: Crystals of the *B. subtilis* E3. The E3 crystallized in space group $I4_1$. Yellow crystals grew to a final size of 300-400 µm over 3 days.

The crystals grew to a size of 300 µm in 3 days (figure 3.28). Both proteins crystallized in space group $I4_1$ with unit cell parameters of a=132 Å, b=132 Å, c=60 Å, α=90°, β=90°, γ=90°, and crystals diffracted to 1.7 Å. The asymmetric unit contained one monomer of the dimer. Figure 3.29A shows an alignment of the native E3 and $E3_{C52S}$ structures. 2mFo-DFc maps are displayed for E3 and $E3_{C52S}$ in blue and orange, respectively. The active site shows the catalytic residue His447, the FAD cofactor and the disrupted disulfide bridge.

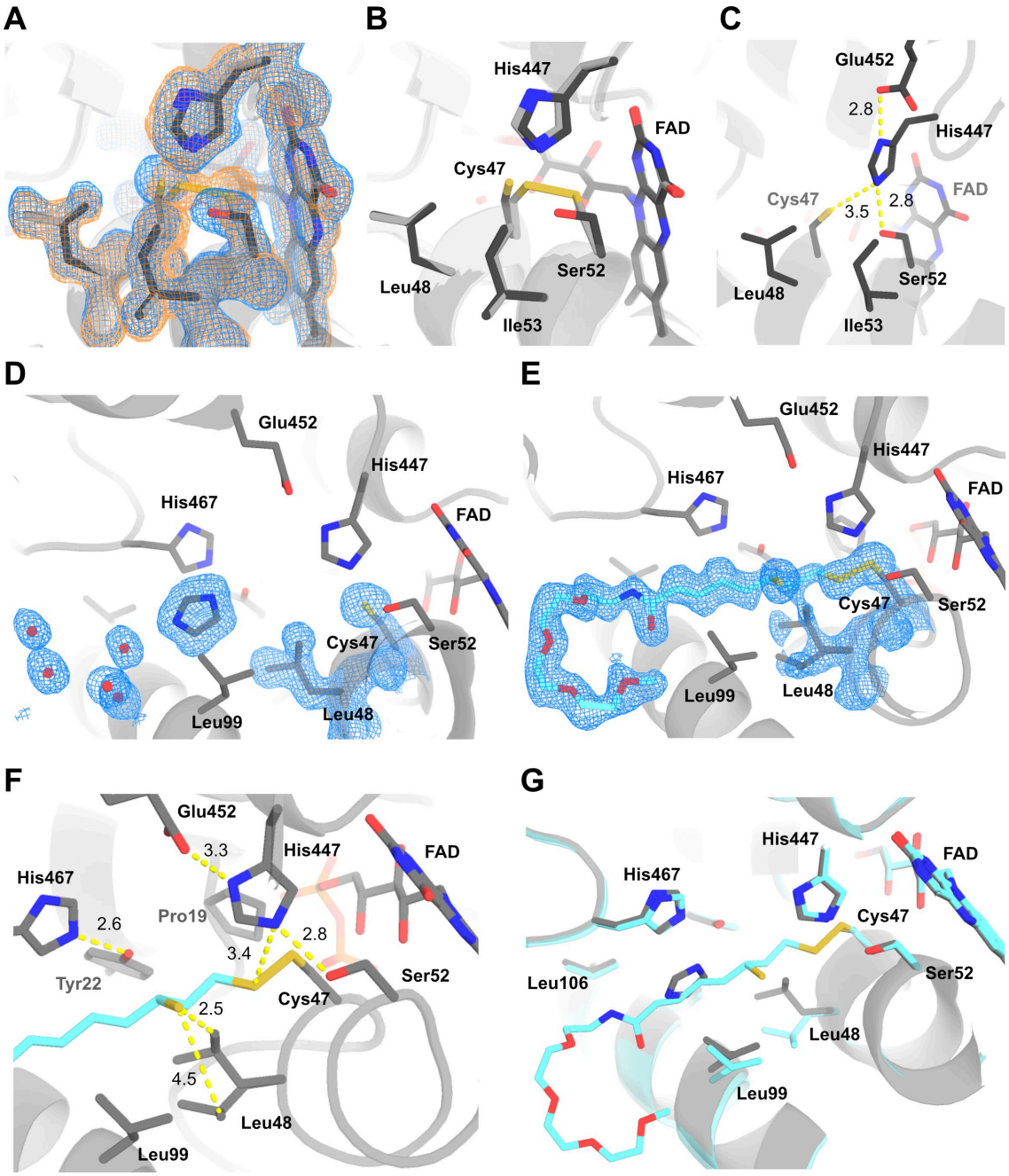

Figure 3.29: Structural details of the lipoamide-E3 interaction at 1.7 Å. A) The active site of native E3 (light grey) is overlayed with $E3_{C52S}$ (dark grey). 2mFo-DFc electron density maps, contoured at 1.5 rms, are shown in orange and blue for native and mutant E3, respectively. The active site shows the isoalloxazine ring system of FAD. B) The C52S mutation does not lead to major structural changes, except for the disruption of the disulfide bridge and a small reorientation of His447, which moves closer to S52 (2.8 Å). C) The catalytic dyad is shown, which consists of Glu452 and His447. D) The active site channel of $E3_{C52S}$ before and after the lipoamide soak are shown. Several water molecules and one imidazole molecule from the mother liquor reside in the channel, the 2mFo-DFc map (blue) is contoured at 1.0 rms. E) After the overnight lipoamide soak, the active channel shows a continuous density which is connected to Cys47. Pegylated lipoamide was modelled into the density and refined to 60 % occupancy. F) Leu48 shows an alternative conformation, which matches the occupancy of lipoamide. When the lipoamide enters the active site, Leu48 flips to avoid Van-der-Waals clashes. G) An overlay of the pre- (grey) and post (blue)-lipoamide soak structures display movements upon lipoamide binding. The residues Leu48 and Leu99 move to free the entrance to the active site.

The C52S mutation disrupts the disulfide bridge in the active site, as expected, but did not lead to major structural changes (figure 3.29A and B). One of the changes was a small movement of His413 closer to Ser52 in 2.8 Å distance (figure 3.29C). Glu452, which is part of the catalytic dyad, is at a distance of 2.8 Å to His447 [186]. Several water molecules and an imidazole molecule from the mother liquor occupy the active site channel (figure 3.29D). To trap lipoamide in the active site, the same soluble lipoamide derivative (lipoamide-dPEG-4-OMe), which has been used for the E2 substrate soaks, was soaked into $E3_{C52S}$ crystals overnight. Figure 3.29E shows the resulting density, which spanned the whole channel and was connected to Cys47. PEGylated lipoamide was modelled and refined at 60% occupancy. The extended density around Cys47 hints towards formation of a mixed disulfide bond with the lipoamide. A leucine residue (Leu48) is present in two alternate conformations, which matches the occupancy of the lipoamide. Detailed interactions are illustrated in figure 3.29F. The channel is formed by several hydrophobic residues, such as Leu48, Leu99 and Pro19. The backside of the channel is closed by His467 hydrogen bonding to Tyr22. The distance between catalytic His447 and S8 of the mixed disulfide is 3.4 Å. Lipoamide binding induced small changes in the channel, which are comprised of movements of Leu99 and Leu48, which block the entrance to the channel. The biggest movement is displayed by Leu48, which displays a side chain rotation of 180° upon lipoamide binding. This could be a gating mechanism to guard the active site disulfide, before the reduced lipoamide binds.

4 Discussion

The pyruvate dehydrogenase complex plays a central role in most living organisms connecting glycolysis, the citric acid cycle and fatty acid biosynthesis. Detailed structural information of this large, dynamic protein complex has not been elucidated as yet. Several cryo-EM structures have visualized its core structure, but have not resolved the outer layer consisting of E1 and E3 subunits [138,187-189]. Multiple crystal structures of its individual subunits, E1, E2 and E3, have been reported [41,61,71,87,89,140]. However, reported structures were generally limited to 1.7-2.6 Å resolution and little information is available about the interaction with the essential cofactor lipoamide. Structural information regarding reaction intermediates, especially for the E1 subunit, has not been visualized so far. Knowledge about its reaction mechanism has generally been adapted from studies of other thiamine diphosphate-dependent enzymes, and spectroscopic methods. Time-resolved serial crystallography has recently emerged as a powerful technique to elucidate reaction intermediates and dynamics [127,161,190]. However, mostly simple model enzymes have been analyzed by this method.

In this thesis, the full decarboxylation reaction of the *B. subtills* PDH E1, a 182 kD protein complex, was analyzed by time-resolved serial crystallography. Parameters such as purification, micro-crystallization, sample delivery and data collection were optimized (chapter 3.1-3.3). This led to the collection of complete datasets with reproducible diffraction to 2.3 Å resolution. Structures of multiple time points in the course of the reaction were elucidated. The time points showed a structural non-equivalence of the two active sites during the course of the reaction, which is called half-of-the-sites reactivity (chapter 3.4). The crystals were optimized for high resolution diffraction and multiple decarboxylation intermediates were elucidated at 0.95-1.03 Å, aiding the interpretation of the time-resolved data (chapter 3.5-3.9). In addition, the high resolution allowed the visualization of a proton network connecting both active sites (chapter 3.10). A substrate mediated proton asymmetry was observed, which could be a common mechanism for thiamine diphosphate-dependent enzymes and a driving force for half-of-the-sites reactivity. The inhibition mechanism of fluoropyruvate was analyzed, which led to the observation of a tricyclic ThDP form containing a seven-membered ring (chapter 3.11). Structural details of this form have not been reported thus far.

High resolution structures of E2CD and E3 were elucidated in complex with the essential cofactor lipoamide (chapter 3.13-3.14). These led to the proposal of a new catalytic residue in the reaction catalyzed by the E2. The interaction of E3 with lipoamide was elucidated for the first time, which showed how flavin-dependent oxidoreductases accommodate the sulfhydryl groups of their respective substrates.

4.1 Classical and time-resolved serial crystallography

4.1.1 Control of relative humidity in microcrystal sample delivery

In this thesis, a micro-crystallization protocol was established for the E1 enzyme of the *Bacillus subtilis* pyruvate dehydrogenase complex. Crystals were optimized by co-crystallization with a nanobody. The nanobody promoted several crystal contacts, which caused the crystals to diffract to higher resolution (figure 3.2, chapter 3.1). Nanobody binding did not affect the structure of the E1. The microcrystal delivery protocol was optimized by testing centrifugation, and vacuum application. This led to higher hit rates, but also led to dehydration effects, which were accompanied by reduced diffraction quality (chapter 3.3). Controlled crystal dehydration is often employed as a post-crystallization technique to increase diffraction in classical cryo-crystallography. However, uncontrolled, fast dehydration, for example upon exposure to air, can decrease crystal diffraction [170,172,191]. Microcrystal dehydration during vacuum application has been mentioned in the literature, but did not result in loss of diffraction quality [192,193]. However, these studies were mostly conducted on model enzymes, such as lysozyme or sperm whale myoglobin, which are smaller than 25 kDa. These dehydration effects showcase potential pitfalls that arise when established protocols are transferred to crystals of larger, multi-subunit enzyme complexes, such as the 182 kDa E1-NB complex. The observations show that sensitivity to dehydration depends on the crystal system, and protocols for micro-crystallization and sample application need to be optimized for individual proteins. Another parameter which can be adjusted is the duration of vacuum application. Too little vacuum suction leads to a low hit rate and an excess of mother liquor surrounding the crystal, which increases background scattering. Too much vacuum suction removes the mother liquor surrounding the crystal and therefore exposes the crystal to the air, which leads to crystal dehydration. In this thesis, the vacuum was applied manually for 1-3 s, until the mother liquor was sufficiently removed as assayed by visual inspection of the chip. An automatic application of vacuum pressure, where vacuum duration and pressure can be adapted to the crystal system, and the viscosity of the solution, could prevent uncontrolled microcrystal dehydration in future experiments.

In classical cryo-crystallography, protein crystals are cryo-cooled which reduces the diffusion of free radicals generated by the ionizing X-ray beam and therefore reduces radiation damage [194,195]. The use of cryoprotectants and the rapid cooling rates achieved by “flash-freezing” of crystals in liquid nitrogen prevent the formation of ice during cryo-cooling [196]. Cryo-protectants are usually not employed in serial crystallography, since the experiments are conducted at 20 °C or higher to follow the enzymatic reaction. In this thesis,

however, the cryo-protectant ethylene glycol was used to protect the E1-NB microcrystals against uncontrolled dehydration. This protection effect could be explained by the high viscosity of the cryo-protection solution, as well as polar interactions between ethylene glycol and water molecules in the solvent channels of the crystal.

4.1.2 Data quality in serial synchrotron crystallography (SSX)

In protein crystallography performed using the rotation method, data quality can be assessed by several data quality indicators such as completeness, R_{meas}, I/σ(I), and multiplicity, which give information about the precision of the data. Completeness represents the collected number of reflections as a proportion of all possible reflections characteristic for that crystal symmetry. R_{meas} measures the intensity spread of a reflection around the average intensity of all reflections. I/σ(I) is the signal divided by the standard deviation of the background intensity (i.e. noise from the detector). Multiplicity denotes, how often a unique reflection is measured [197]. In serial crystallography, R_{meas} is often exchanged with R_{split}. R_{split} represents the agreement of intensities between reflections distributed in two random and equal half sets [129]. Table 7 shows exemplarily the data quality of the 400 ms timepoint acquired in the time-resolved experiment (figure 3.8, chapter 3.4).

Table 7: Data quality of the 400 ms timepoint chip at 2.44 Å

Number of crystals (hit rate)	13,004 (50.8%)
Number of reflections	16,751,230
Reflections unique	111686
Multiplicity	150 (122.8)
Completeness [%]	100 (100)
R_{split} [%]	25.07 (127.66)
CC* [%]	98.9 (70.5)
SNR	2.34 (0.88)

The observed hit rates and data quality indicators were comparable to published datasets of the model enzyme xylose isomerase, which were acquired with the same setup. For example, a total of 13,004 crystals were present on the chip, which yielded close to 17 million reflections including 111,700 unique reflections. This amounts to an overall multiplicity of 150 and an overall R_{split} of 25%. In comparison, the overall R_{split} values ranged from 28 to 50% for the xylose isomerase datasets [198]. The overall completeness was 100%, in the high-resolution shell as well. This indicates that the crystals had no preferential orientation on the chip. The resolution, however, did not allow direct chemical interpretation of the reaction intermediates, which may have been due to several reasons. In crystallography, two types of errors affect the quality of the data: random errors, which affect

the precision of the data, and systematic errors which affect the accuracy. In classical cryo-crystallography, datasets are collected from single crystals rotated through the X-ray beam. In contrast, serial crystallographic diffraction images are collect from thousands of randomly oriented crystals, termed “stills”. Therefore, partial reflections are recorded with no oscillation information. Partial reflections on stills can be processed by software packages like CrystFEL, which uses the Monte Carlo method for estimating reflection intensities. This approach calculates an average of all intensities from symmetry related reflections [199]. However, determination of the crystal symmetry from stills can be difficult, as no systematic absences can be determined. Assumptions of unit cell parameters and crystal symmetry based on rotation datasets of large crystals could lead to systematic errors. Another contributor to systematic errors are crystal non-isomorphisms and subsets of larger crystals with better diffraction, which introduces systematic errors during scaling and merging. For example, some slight non-isomorphism could be observed in the c-axis during the dehydration experiment at 90% r.H., which showed two populations at 87.5 and 88.7 Å (figure 3.6B, chapter 3.3).

Another reason for the poor densities in the active site could be multiple populations of intermediate states. Time-resolved serial X-ray data contain a mixture of different states, because the structure represents an average of all molecules within the crystal. Timepoints containing a specific, populated reaction intermediate can be identified before the SSX experiment, which narrows down the time-range to be collected in the SSX experiment. The crystal structure of a protein is usually identical in solution, but the reaction kinetics could be altered *in crystallo*. Therefore, one way to track reaction intermediates is by following the spectral signature of potential reaction intermediates in the crystal. The reactions of hemoglobin, and PLP-dependent proteins were tracked by single-crystal optical spectroscopy, for example [200]. However, the spectral signature of the thiamine cofactor of the E1 is close to the UV absorption of the protein, which would complicate the measurement *in crystallo*.

Another factor influencing data quality in SSX experiments is radiation damage. Two types of radiation damage can be distinguished: global- and specific radiation damage. Global radiation damage is manifested as loss of diffraction power over time. For cryo-cooled crystals a 50% loss of diffraction intensity at 20 MGy was predicted [201]. Experimental determination in apo- and holoferritin crystals gave a dose limit of 43 MGy, at which 50% of the diffraction intensity was lost [202]. However, specific radiation damage can already occur at lower doses. This manifests as changes of the protein structure, such as decarboxylation of aspartate or glutamate residues, or disulfide bond breakage [203]. The global and specific radiation damage dose limits are lower at room temperature [204]. For example, a dose of 0.57 MGy caused a 50% drop in the diffraction intensity of lysozyme crystals,

and specific radiation damage already occurred below 0.08 MGy [204]. In addition, the rate of intensity loss is dependent on resolution [205], whereby the intensities of high resolution reflections decay faster than low resolution reflections. In the time-resolved experiments reported here, each crystal was probed twice for a total of 10 ms with a flux of $2x10^{12}$ photons/s. This corresponded to a dose of roughly 0.04 MGy, which corresponds to half of the value at which specific radiation damage was reported at room temperature [204]. A loss of diffraction quality after time was not observed. Therefore, radiation damage was unlikely to have been dominant in this experiment.

The E1-NB microcrystals showed nonuniform growth evidenced by the flat shape of the crystals. As the scattering power of a crystal is proportional to its volume [206], the microcrystals could be optimized to grow in a more 3D shape, which would improve crystal diffraction.

4.1.3 Classical cryo-crystallography complements SSX

Time-resolved serial crystallography is a powerful tool, which has allowed the observation of the half-of-the-sites reactivity in the E1 in “real time”. The time-resolved data, however, did not allow direct interpretation of intermediate states due to a low resolution and mixed intermediate populations. Oscillation data collected from single crystals in classical cryo-crystallography could complement the serial data, since time-resolved experiments benefit from some prior experimental knowledge; for example, the crystal structure can be elucidated prior to the time-resolved experiment. Prior knowledge about the crystal symmetry is important, since systematic absences cannot be determined from diffraction patterns without oscillation information. Substrate soaks can reveal whether the active site of the enzyme is accessible in the crystalline lattice, whether large movements or changes in the unit cell parameters occur, and whether the crystal is stable throughout the course of the reaction. A benefit of using large, cryo-cooled protein crystals is that sub-atomic resolutions can be achieved. Resolutions better than 1.1 Å allow the detection of hydrogen atoms in the protein. Knowledge of the positions of hydrogen atoms is important, as hydrogen bonds play vital roles in ligand binding and specificity, and general acid/base enzyme catalysis [207][68]. In this thesis, to interpret the electron densities observed in the time-resolved experiment, structures of decarboxylation reaction intermediates were elucidated by classical cryo X-ray crystallography. Due to the high resolution of the structures, a hydrogen wire connecting both active sites of the native E1 and lactyl-ThDP structure could be visualized.

4.2 Half-of-the-sites reactivity in the E1

The structures of native E1, the pre-decarboxylation intermediate lactyl-ThDP, and the post-decarboxylation intermediate carbanion-ThDP were elucidated at 0.95, 1.03, and 1.03 Å, respectively (chapter 3.6-3.8). The intermediates showed different occupancies in the different active sites which is evidence for the inherent half-of-the-sites reactivity of the E1 enzyme. The lactyl-ThDP structure revealed a protonation asymmetry at the active site, where N1´ of the aminopyrimidine ring was protonated in one active site, but deprotonated in the other (figure 3.15, chapter 3.10). In the native E1 structure, N1´ in active site B shows a stronger hydrogen signal than N1´ in active site A. In general, site B shows a stronger hydrogen signal than site A, which could be explained by differences in the ThDP B-factors. The B-factor (or atomic displacement factor) describes the attenuation of X-ray diffraction caused by dynamic disorder of atoms, such as thermal motion, or static disorder in the crystal lattice [208]. The mean ThDP B-factors of site A and B are 6.89 $Å^2$ and 6.42 $Å^2$, respectively. The lower B-factor in site B might increase the hydrogen signal leading to the observed differences between the sites in the native E1 structure, as visualized by the hydrogen omit difference map.

4.2.1 Substrate mediated protonation asymmetry

Several ThDP-dependent enzymes display half-of-the-sites reactivity, which is a form of negative cooperativity. In the PDH E1 for example, there is structural and kinetic evidence in support of half-of-the-sites reactivity [59,62]. In this thesis, further structural evidence for half-of-the-sites reactivity of the bacterial E1 was gathered by time-resolved crystallography. Structures of the E1 at different time-points of the reaction showed, that active site A was always one step ahead of active site B.

In the E1 enzyme, both active sites are connected by a water channel of 20 Å in length. A similar water channel was observed in the heptose isomerase, where a proton wire connecting both active sites modulates the acidity of two catalytic zinc ions [209]. In the E1, the proton wire modulates the reactivity of the cofactor ThDP. ThDP is activated by a conserved glutamate residue, which deprotonates a nitrogen of the aminopyrimidine ring. It was shown, that activation of ThDP involves the formation of low-barrier hydrogen bonds (LBHB) in the *Lactobacillus plantarum* pyruvate oxidase (LpPOX) and human transketolase (HsTK) [63]. In the human transketolase, the LBHB was observed between the conserved glutamate Glu366, which is the equivalent to Glu59 in the *B. subtilis* PDH E1, and a neighboring glutamate, Glu160, in the active site channel. The authors showed, that Glu160 substitution with glutamine disrupted the formation of the LBHB. Furthermore, the same substitution led to a loss of cooperativity, as illustrated by the Hill-coefficient. In the

pyruvate oxidase in complex with its substrate phosphate, two LBHBs were observed. One was located between the activating glutamate and N1´ of the aminopyrimidine ring and the other was observed between an adjacent histidine and another glutamate inside the channel [63]. The high resolution structures elucidated in this thesis allowed visualization of the proton wire connecting both active sites in the E1 enzyme. However, there were no indications for LBHBs in the E1 structures. The distances between the cofactor and residues in the proton channel were longer than the LBHB threshold distance of 2.65 Å and 2.55 Å for O-N and O-O distances, respectively. Furthermore, the E1 contains a glutamine residue, the equivalent to E160 in the transketolase, adjacent to the conserved glutamate. LBHBs are formed, when the pKa values of both groups match, which is not the case for the glutamate-glutamine pair [63]. However, an asymmetry was observed in the lactyl-ThDP structure with regards to the distribution of hydrogen atoms in the proton wire, which was not present in native E1. This is in agreement with observations in both the transketolase and pyruvate oxidase, where a proton asymmetry was present in the channel when the enzyme was complexed with cofactor and substrate. The asymmetry was absent without substrate or cofactor. LBHBs might therefore play a role in cooperativity of other thiamine-dependent enzymes, but might not be a fundamental requirement for active site communication. The general active site communication via a proton wire, however, seems to be a conserved mechanism. One difference between the E1 and LpPOX/HsTK water channel is the presence of a hexacoordinated magnesium ion in the E1, which is located at the two-fold symmetry axis between both active sites.

4.2.2 The communication cycle

Two models have tried to explain the underlying mechanism of active site communications. One was based on small subunit motions that affect the active sites, termed a flip-flop mechanism [61] and the other was based on a proton wire connecting the active sites [62]. The observed half of the sites reactivity and protonation asymmetry, together with the aforementioned LBHB reported in the literature, support the proton wire model. The back and forth proton shuttle was referred to as an “atomistic newton´s cradle” or “slinky cycle” [63,210]. Figure 4.1 illustrates an adaption of the slinky cycle based on the observations of the time-resolved experiments and high-resolution structures. It can be observed that in the native state, both cofactors are protonated at N1´. Active site A forms the lactyl-ThDP intermediate before active site B binds pyruvate. Active site A forms the carbanion-ThDP intermediate, while active site B generates the lactyl-ThDP intermediate. As a consequence, active site A remains one step ahead in the reaction course.

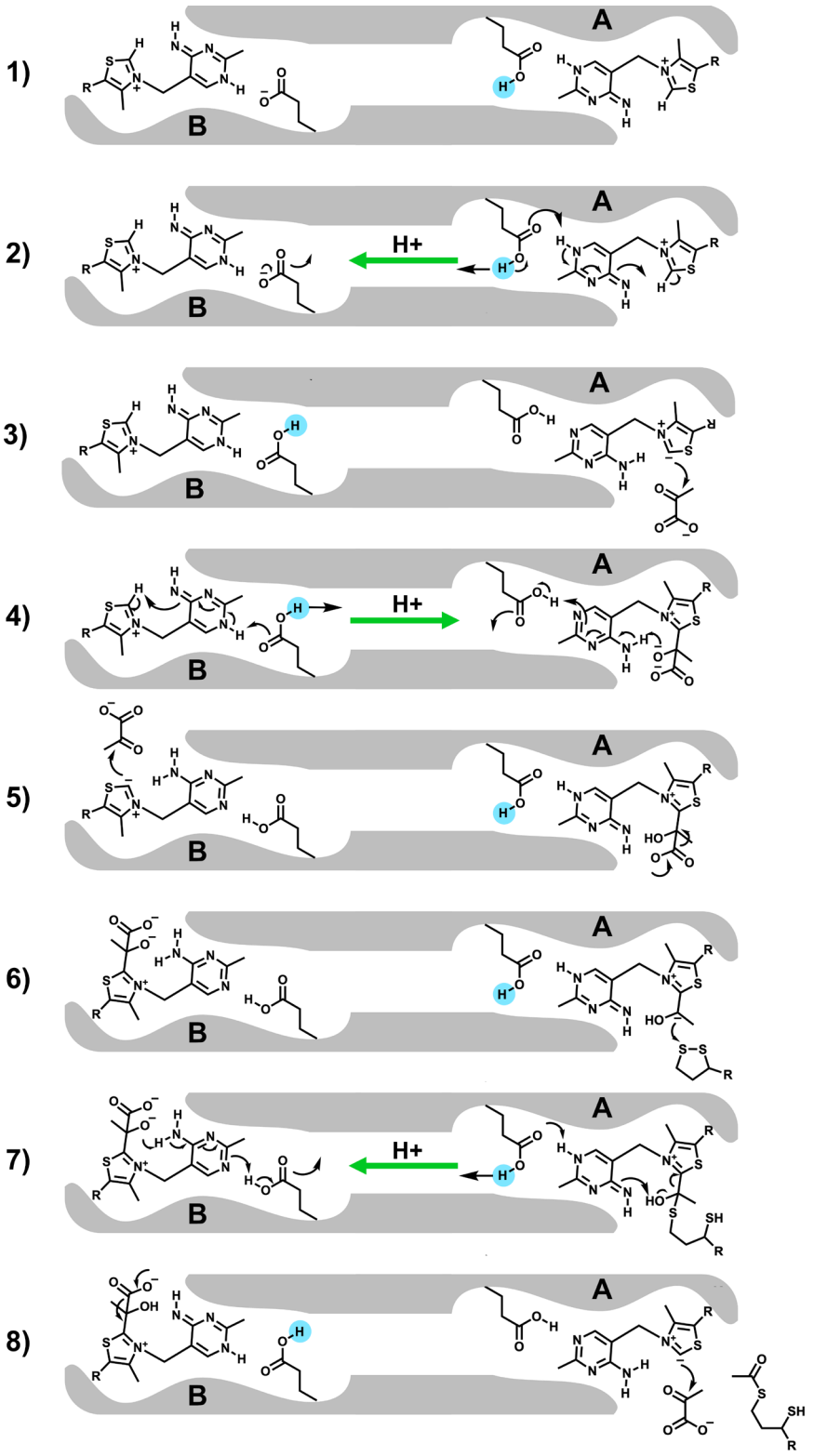

Figure 4.1: Active site communication via the proton wire in the E1 enzyme. A schematic of the proton shuttle between active sites A and B is shown. The shuttling proton is shown in blue 1) Both active sites are inactive. 2) Active site A is activated, which shuttles a proton to site B. 3) Site A reacts with pyruvate, generating lactyl-ThDP 4) Site B is activated, which shuttles a proton to site A. Lactyl-ThDP is protonated at the oxyanion. 5) Site B reacts with pyruvate to yield lactyl-ThDP. Site A decarboxylates lactyl-ThDP. 6) Site A undergoes reductive trans-acetylation. 7) The resulting tetrahedral intermediate collapses upon deprotonation. A proton is shuttled to site B, which protonates lactyl-ThDP. 8) Site A completes the reaction cycle, acetylated lipoamide leaves the active site. Site B decarboxyles lactyl-ThDP. The reaction can repeat indefinitely. The figure was adapted from the "slinky cycle" proposed by Frank et al [210].

The modified cycle proceeds as follows: first, both active sites are protonated at N1´ of the AP ring, but a proton asymmetry already exists in the channel (1). Active site A is activated first by deprotonation forming the reactive ylide. A proton is then shuttled to active site B (2). Pyruvate enters active site A, and lactyl-ThDP is formed (3). ThDP is activated in site B, which shuttles a proton to site A allowing N4´ of the AP ring to then protonate the oxyanion of lactyl-ThDP (4). Pyruvate in site B undergoes a nucleophilic attack by the ThDP ylide and lactyl-ThDP is decarboxylated in site A (5). Lactyl-ThDP is formed in site B. The carbanion in site A attacks the lipoamide (6). The resulting tetrahedral intermediate collapses upon deprotonation, which shuttles a proton to site B. The oxyanion of lactyl-ThDP is protonated (7). The reaction cycle is complete in site A and acetylated lipoamide leaves the active site. Lactyl-ThDP is decarboxylated in site B (8). Step 8 mirrors step 5, but with active sites A and B performing the opposite roles. The reaction cycle repeats indefinitely.

4.3 An unusual thiazole conformation

The ThDP cofactor in the native E1 structure elucidated at 0.95 Å resolution displayed an unusual conformation, whereby the C2 atom of the thiazole ring was distorted out of plane by 18° (figure 3.10, chapter 3.6). A search of structures containing thiamine diphosphate at resolutions below 1.2 Å in the protein data bank (PDB) revealed a structure of the *Pichia stipitis* transketolase at 0.97 Å with a similar thiazole conformation (PDB ID: 5XSA). An overlay of the thiazole ring shows the similarity with the conformation observed in the native E1 structure, although the out-of-plane distortion was more prominent in the transketolase (figure 4.2). The authors reported five structures with different thiazole conformations, which were attributed to non-kekulé mesomerism [176]. The conformation shown in figure 4.2 was attributed it to a diradical located at N3 and C2. Catalysis of neither the transketolase nor the E1 is suspected to follow a radical mechanism, thus the influence of this thiazole conformation on catalysis requires further investigation. It does, however, illustrate the conformational and electronic versatility of thiamine diphosphate.

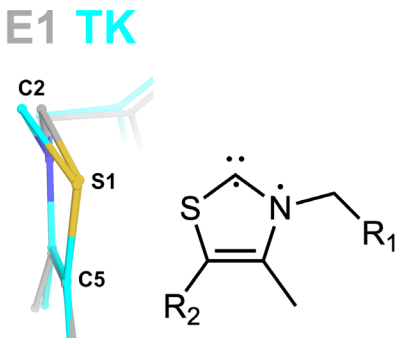

Figure 4.2: Alignment of the E1 and transketolase thiazole ring. The thiazole ring of ThDP of the E1 (grey) is aligned with thiazole of transketolase (blue) (PDB ID:5XSA). The authors attributed this conformation to non-kekulé diradical structures, shown on the right [176].

4.4 High resolution pre-decarboxylation intermediate

The pre-decarboxylation intermediate lactyl-ThDP was elucidated at 1.03 Å resolution by cryo-trapping and pH change (figure 3.13, chapter 3.8). Lactyl-ThDP has been previously observed in pyruvate oxidase from *L. plantarum* at 2.0 Å and figure 4.3 shows an overlay of both structures (PDB ID:2EZ8) [113]. In both structures, C2 of the thiazole ring is covalently connected to C2α of the pyruvate molecule. Both carboxylate groups point towards the channel exit and are located above the thiazole plane, which contributes to decarboxylation due to optimal conjugation with the thiazole ring [113]. One difference is the rotation of the carboxyl group, whereby in the LpPOX structure, the carboxyl moiety is oriented by interactions with Gln122 and Glu483, which rotates the carboxyl moiety clockwise. Conversely, in the lactyl-ThDP structure of the E1, the carboxyl group is surrounded by His128 and His273. It is rotated anti-clockwise due to the electrostatic forces and hydrogen-bonding exhibited by His128 and His273.

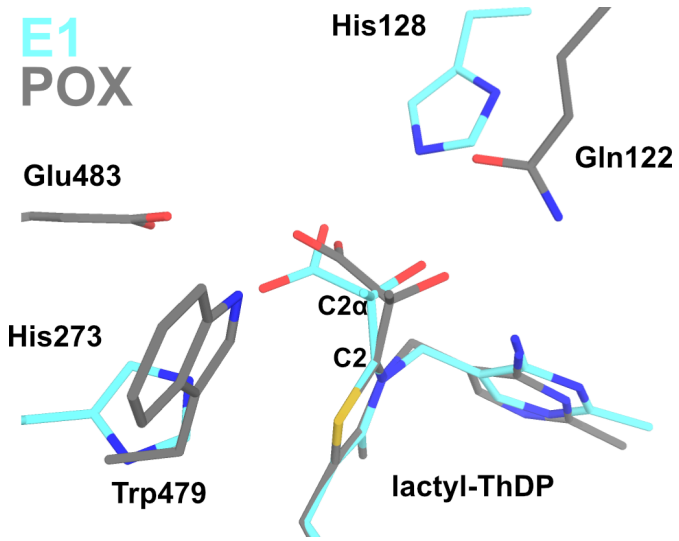

Figure 4.3: Overlay of lactyl-ThDP intermediate of the BsE1 enzyme and LpPOX. The structures of the active site of E1 enzyme (blue) and POX (grey) are shown containing the lactyl-ThDP decarboxylation intermediate. Differences between the structures are the carboxylate rotation, as well as the degree of out-of-plane distortion of the lactyl moiety with respect to the thiazole plane.

Another difference is the degree of out-of-plane distortion of the C2-C2α bond: the bond is distorted by 22° in the E1 enzyme and 6° in the LpPOX. Either the resolution of the LpPOX structure did not resolve this distortion, or the high distortion angle is a specific feature of the E1 enzyme. However, the same out-of-plane distortion was observed in the transketolase in complex with its substrate D-xylulose-5-phosphate. The distortion was accompanied by a C-C bond elongation of 0.1 Å, which destabilized the pre-cleavage intermediate [69]. A QM/MM calculation argued against the enzyme-mediated intermediate destabilization. According to the authors, the strain was derived from a intramolecular hydrogen bond

in the thiamine intermediate and not from the enzyme itself. The calculation indicated that the distortion only provides a small contribution to the high reaction rate of transketolase [211]. In the lactyl-ThDP structure reported here, no C-C bond elongation could be detected. However, a noticeable deviation of 6.5° from the optimal tetrahedral angle of 109.5° was observed at C2α, which pushed the carboxyl group towards His273. There is, at the time of writing this thesis, no small molecule structure of lactyl-ThDP available for comparison. A small molecule crystal structure of the lactyl-ThDP phosphonate analogue 2-hydroxy-2-(2-thiamin)ethylphosphonate has been elucidated. The lactyl-ThDP analogue showed tetrahedral angles of 109, 109, 109 and 110° about the C2α atom [212]. Therefore, the strained carboxylate conformation is likely a result of electrostatic forces of the positively charged histidine residues at pH 5.0. Whether and by which means this angle strain contributes to catalysis must be determined by chemical calculations.

4.5 The roles of His128 and His273 during decarboxylation

The E1 active site contains two conserved histidine residues, one is positioned near the thiazole ring and the other near the diphosphate group. These correspond to His128 and His273 in the *B. subtilis* PDH E1, respectively. An initial substitution of His128 or His273 with asparagine was carried out in order to trap reaction intermediates, and these substitutions did not result in any conformational changes. Assays of the formation of post-decarboxylation intermediates showed that substitution of His128 inhibited pyruvate decarboxylation, while $E1_{H273N}$ still retained pyruvate decarboxylation activity (figure 3.12, chapter 3.8). These results are in agreement with existing literature. In the human BCDHc, His291 corresponds to His273 in *B. subtilis* PDH E1. Substitutions of the His291 residue resulted in decreased decarboxylation and trans-acetylation activity, and reduced affinity towards ThDP, leading to the assignment of a rather structural role than catalytical role for His291 [213]. Mutations of the His128 equivalent abolished decarboxylation and trans-acetylation activity. The authors identified the His128 equivalent as the critical catalytic residue for decarboxylation [213]. Other literature reported, that substitutions of His128 for glutamine still retained decarboxylation activity, while substitutions for asparagine did not. His128 likely orients pyruvate in the active site for an optimal nucleophilic attack by ThDP [41]. A structural role of His273 can be confirmed in this thesis, since the H273N substitution retained decarboxylation activity, but lead to movement of the cofactor (figure 4.4). The overlay shows the carbanion-ThDP observed in both native E1 (grey) and $E1_{H273N}$ (blue). The phosphate moiety occupies the same position, but S1 of the thiazole ring moves in the direction of the channel entrance. This movement and the fact, that a higher ThDP concentration was needed to obtain full thiamine occupancy, verify the loss of affinity observed

in kinetic experiments. His273 appears to position the cofactor in the pocket via electrostatic interactions with the diphosphate, as well as simple Van-der-Waals interactions with the sulfur atom. Other authors hypothesized, that His273 modulates the cofactor electronically by close contacts to the thiazole sulfur atom [41]. Evidence for this hypothesis is shown by the observation, that mutation of H273 changed the equilibrium of post-decarboxylation intermediate. The only intermediate observed in $E1_{H273N}$ mutants was the tetrahedral carbanion-ThDP, while native E1 post-decarboxylation intermediates exhibited a tautomeric equilibrium of carbanion-ThDP and enamine/acetyl-ThDP. The roles of both His128 and His273 during the second reaction of the E1, the reductive trans-acetylation, are not entirely clear, since structural details of the lipoamide-E1 interaction have not yet been elucidated.

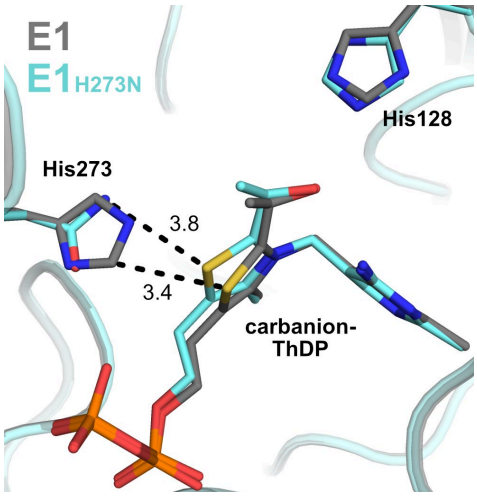

Figure 4.4: Movement of the carbanion-ThDP intermediate in $E1_{H273N}$. The post-decarboxylation intermediates of E1 (grey) and $E1_{H273N}$ (blue) are aligned. The thiazole ring moves in the direction of channel entry in the substituted structure keeping a distance of 3.8 Å.

4.6 The carbanion-enamine tautomerism

The chemical nature of the post-decarboxylation intermediate, which undergoes reductive trans-acetylation with the lipoamide arm, has been debated. Structural and spectral evidence exist for both an enamine-carbanion intermediate, as well as an acetyl-ThDP intermediate. The acetyl-ThDP could react as an electrophile with a thiolate nucleophile, or the nucleophilic carbanion/enamine could attack the lipoamide disulfide with concomitant protonation of the other disulfide sulfur [50-53]. In this thesis, the post-decarboxylation intermediate was elucidated at 1.03 Å (figure 3.11, chapter 3.7). A mixture of intermediates was observed, which were attributed to a tetrahedral carbanion- and a more planar enamine/acetyl-ThDP state. The mixture of states present made the refinement with relaxed cofactor restraints difficult. Therefore, the chemical identity of the more planar intermediate cannot

yet be assigned. However, a similar post-decarboxylation intermediate was observed in the LpPOX, which was interpreted as a mixture of a tetrahedral carbanion and a tetrahedral ketone moiety. The authors argue, that the carbanion-ketone tautomerism helps the interconversion between nucleophilic and electrophilic species [160]. The POX catalyzes its reaction via a radical mechanism that utilizes its cofactor flavin adenine dinucleotide (FAD). FAD undergoes a $1e^-$ reduction by the nucleophilic carbanion. The oxidized ketone group then reacts as electrophile with the nucleophilic phosphate group, yielding acetyl-phosphate. The E1, however, does not react with FAD, but with the lipoyl group. It was shown, that lipoic acid likely doesn´t undergo reduction via sequential one-electron transfer [214]. The post-decarboxylation intermediates obtained by soaking BCDH substrates into E1 crystals exhibited the same distribution of carbanion- and enamine/acetyl-ThDP intermediates. A carbanion form of these intermediates has been observed in the human BCDHc, but at lower resolution [215]. In conclusion, the E1 seems to stabilize a tautomeric equilibrium in the active site, even with bulkier BCDH substrates. This stabilization is partly mediated by His273, since substitutions changed the intermediate equilibrium in favor of carbanion-ThDP, as discussed in chapter 4.5.

The discovery of a similar carbanion-/ketone tautomerism, as observed in the POX, hints towards a conserved mechanism of intermediate stabilization and interconversion. The equilibrium may be a means of stabilizing the negative carbanion in the hydrophobic active site. Should the interconversion between an electrophilic and nucleophilic state be required for the E1 reaction, the carbanion could reduce the lipoamide and the resulting electrophilic carbonyl could undergo a nucleophilic attack by the thiolate. Structural information showing the lipoyl domain bound to the E1 might provide further information into the mechanism of reductive trans-acetylation.

4.7 The inhibition mechanism of fluoropyruvate

Fluoropyruvate inhibits the E1, as well as the full PDHc in *E. coli* [49], [177]. The underlying inhibition mechanism was reported to involve the alkylation of sulfhydryl groups present at the lipoamide or in the E1 active site [49]. However, the *E. coli* E1 contains only one cysteine residue per monomer, which is deeply buried and positioned far from the active site according to a crystal structure (PDB ID: 2IEA). This speaks for a different inhibition mechanism. It was also shown, that the reaction with fluoropyruvate creates acetyl-ThDP which can serve as a substrate during reductive trans-acetylation [177]. Figure 4.5A shows the postulated mechanism of acetyl-ThDP formation by fluoropyruvate, as reported by Leung et al [177]. The mechanism is identical to pyruvate decarboxylation until the formation of the post-decarboxylation intermediate. Then, fluoride is eliminated, which generates an

enol. Tautomerization of the enol forms the acetyl-ThDP intermediate. However, the structures of E1 crystals with fluoropyruvate reported in this thesis did not show acetyl-ThDP, but a tricyclic form of ThDP including the formation of a seven-membered ring (figure 3.17, chapter 3.11). The formation of this tricyclic form with a seven-membered ring, also termed a carbinolamine, has been observed by NMR during acetyl-ThDP synthesis [50]. Figure 4.5B shows a possible mechanism for the formation of the seven-membered ring. The electrophilic ketone of acetyl-ThDP is attacked by the nucleophilic N4´ amine, which leads to the formation of a tetrahedral product. The pKa of the N4´ nitrogen of the AP ring is around 7.5 [216] and the crystallization condition was at pH 8.0. As a consequence, N4´ in this structure is likely deprotonated and contains a free electron pair, which facilitates the nucleophilic attack. The proximity of the acetyl carbonyl and N4´ due to the V-conformation of ThDP favors the reaction. Another tricyclic form of ThDP was synthesized by incubation with a base. The resulting product, dihydrothiochrome diphosphate, forms a yellow color upon opening of its thiazole ring (figure 4.5C), and this method was used to measure thiamine concentrations [217]. However, dihydrothiochrome diphosphate contains two six-membered rings, which are formed by the base catalyzed reaction of N4´ and C2 of the thiazole ring and the aminopyrimidine ring [218]. A PDB search revealed two crystal structures containing tricyclic ThDP forms (PDB ID: 3AHG, 1OZH). Figure 4.6A shows tricyclic ThDP from the *Bifidobacterium breve* phosphoketolase. It contained two six-membered rings, which resemble the structure of dihydrothiochrome. Phosphoketolases catalyzes the conversion of different sugar phosphates into acetyl-phosphate [179].

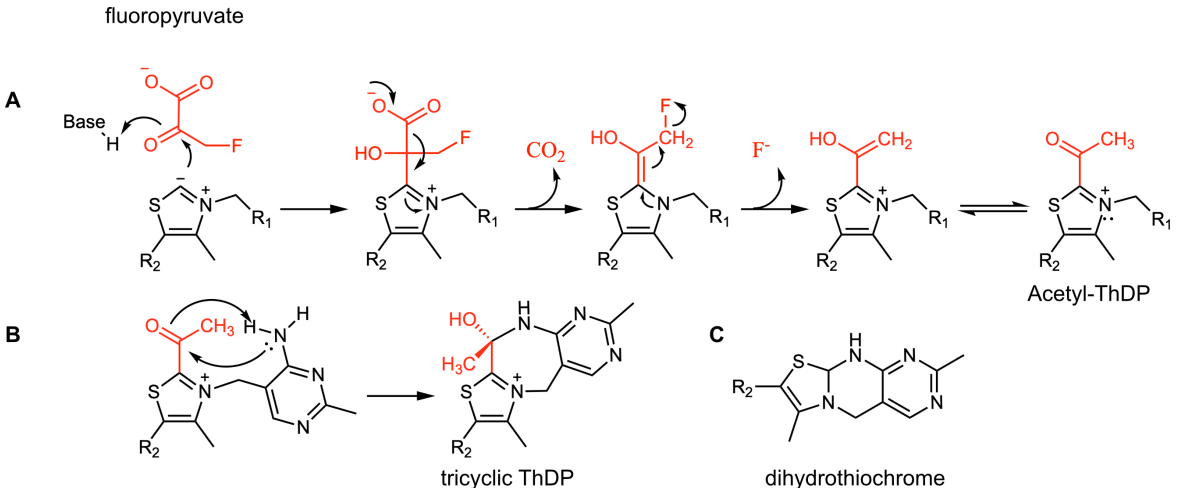

Figure 4.5: A potential mechanism of fluoropyruvate inhibition. A) The reaction of ThDP with fluoropyruvate is shown, which yields acetyl-ThDP. B) At pH 8.0, acetyl-ThDP undergoes intramolecular nucleophilic attack from the N4´ amine onto C2α of the acetyl group, which results in formation of a seven-membered ring connecting aminopyrimidine and thiazole rings.

The protein was crystallized at pH 9.0, which may explain the formation of this tricyclic form. Figure 4.6B shows a tricyclic ThDP intermediate of the *Klebsiella pneumoniae* acetolactate synthase. This enzyme catalyzes pyruvate decarboxylation and subsequent carboligation to yield acetolactate. The intermediate/off-pathway product shows a six-membered ring formed by N4´ and C2 of the thiazole ring. A hydroxyethyl moiety is connected to C2 as well. Structural details of a seven-membered tricyclic ThDP form have not been reported so far. However, this form likely represents an off-pathway product, formed by reaction with an unnatural substrate at pH 8.0. The reaction is likely to be reversible, but may explain the inhibition of the E1 observed in kinetic experiments. In summary, this form and the decarboxylation intermediates reported in previous chapters illustrate the chemical versatility of thiamine diphosphate.

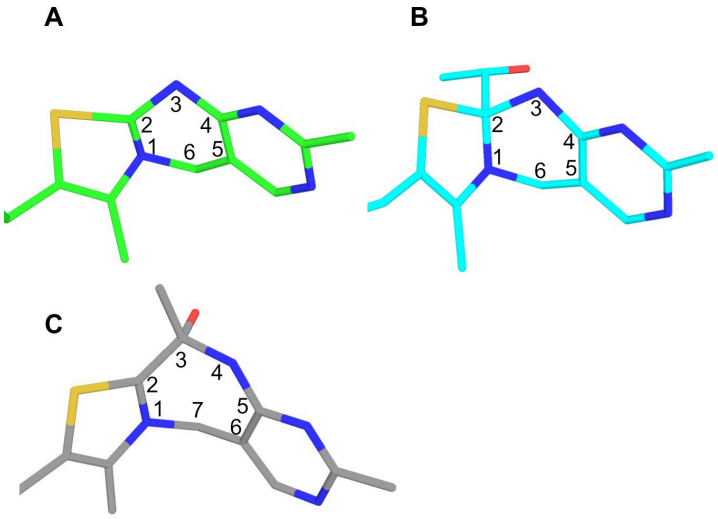

Figure 4.6: Comparison of different tricyclic thiamine diphosphate forms. A) Tricyclic ThDP from the phosphoketolase (green). B) A post-decarboxylation tricyclic ThDP intermediate from the acetolactate synthase (blue). C) Tricyclic ThDP with seven-membered ring of the E1 observed after reaction with fluoropyruvate (grey).

4.8 E2 gating mechanism

4.8.1 An allosteric signal leads to loop rearrangement

The icosahedral PDHc core consists of 60 E2 subunits. To elucidate the E2 structure at high resolution, constructs of the catalytic domain trimers (E2CD) were purified and crystallized. Five different E2CD structures were elucidated in this thesis (figure 3.24, chapter 3.13). Four crystallized in the salt based condition (E2salt), and one crystallized in the PEG based condition (E2peg). Of the four salt-based structures, two were cryo-protected in ethylene glycol (EDO) and two with glycerol (GOL). The CoA binding site was blocked by a crystal contact in the E2salt structures. The open and closed conformations of a loop region (AA309-317) were detected in some of these structures. Movement of a similar loop region has been observed in the bovine BCDH E2 core, which lead to opening and closing of the lipoamide channel. The authors postulated a gating mechanism, which connects CoA binding and opening of the lipoamide channel [86]. The E2CD structures reported here did not show significant movement of the lipoamide channel. However, loop movements were more pronounced in the structures reported here and closing of the loop brought an aspartate residue into close proximity of the catalytic histidine. Table 4.1 shows the conformations of the loop in the structures elucidated in this thesis.

Table 8: Summary of E2CD crystal structures

structure	E2salt lipoamide	E2salt native	E2salt lipoamide	E2salt native	E2peg CoA
cryo protectant	EDO	EDO	GOL	GOL	EDO + isopropanol
loop	closed	closed	open	open	open
CoA binding site	blocked	blocked	blocked	blocked	free
CoA	-	-	-	-	✓
lipoamide	✓	-	✓	-	-
resolution [Å]	1.11	1.08	1.34	1.35	1.9

The table sums up cryo-protectants, state of the loop, state of the CoA binding site and type of substrates observed in these structures. The loop was in the closed conformation in the E2salt structures that were cryo-protected with ethylene glycol and open in all other structures. The loop was both in closed conformation in the both the lipoamide soak and native E2salt EDO structures. However, the loop was open in both native and lipoamide E2salt structures cryo-protected with glycerol, and in the E2peg structure soaked with CoA and cryo-protected with EDO and isopropanol. Lipoamide binding did not influence the rearrangement, since native structures of the EDO soak also showed a closed loop as well.

One explanation could be, that the CoA site blocked by the neighboring N-terminus mimics CoA binding. However, structures with a blocked CoA binding site and cryo-protected with GOL did not display loop closure. Therefore, a combination of the blocked CoA binding site and the presence of ethylene glycol led to loop closure. One possible explanation could be that ethylene glycol occupies a key allosteric position, or mimics the alkyl chain of lipoamide. One EDO molecule was occupying a region close to the active site, which is usually occupied by the β-mercapto-ethylamine arm of CoA. An EDO molecule in this position could therefore mimic CoA binding near the active site and facilitate loop rearrangement. However, the loop was in the open conformation in the E2peg structures complexed with CoA and cryo protected with EDO, but an explanation for this might be the low occupancy of CoA in the active site.

4.8.2 A closed loop conformation completes the catalytic dyad

The postulated mechanism of acetyl-transfer involves a catalytic dyad containing a histidine and aspartate residue, which activates the thiolate of CoA for nucleophilic attack. Asp417 has previously been proposed as a member of the catalytic dyad, according to crystal structures and site directed mutagenesis studies. A multiple sequence alignment shows that both Asp417 and Asp311 are partially conserved among different 2-oxoacid E2 subunits (figure 4.7) and most E2s contain aspartate in position 417. The aspartate residues are indicated by red triangles. The BCDH of *Acetobacter vinelandii* , however, contains an asparagine residue instead of aspartate and interestingly, mutations of asparagine to aspartate resulted in a decrease of activity by one order of magnitude [219]. The *B. subtilis* BCDH and human PDH do not contain an acidic residue at position 311. The black triangles show the conserved tripeptide sequence DHR, which contains the catalytic His413. Both Asp412 and Arg414, framing His413, were suggested to be catalytic residues. However, initial E2 crystal structures however showed that they play a structural role by orienting His413 towards the active site. A search of E2 structures with resolution <3 Å in the PDB showed that Asp417 points away from His413, with distances greater than 3.35 Å observed in all analyzed structures (PDB IDs:1DPC,1EAA-1EAF,4N72,2II3-2II5). In contrast, the structures reported here show that closure of the loop brings Asp311 to within 2.7 Å distance of His413. It is likely that E2 subunits from different organisms or different 2-oxoacid dehydrogenase complexes employ different residues for catalytic dyad formation. The position of Asp311 clashed with CoA when the structures were aligned, suggesting that either the loop adapts a different conformation when CoA binds, or loop rearrangement plays rather a structural role in connecting CoA binding and the lipoamide channel, as

reported for the BCDH core. Further kinetic data is needed to verify the role of Asp311 in catalysis.

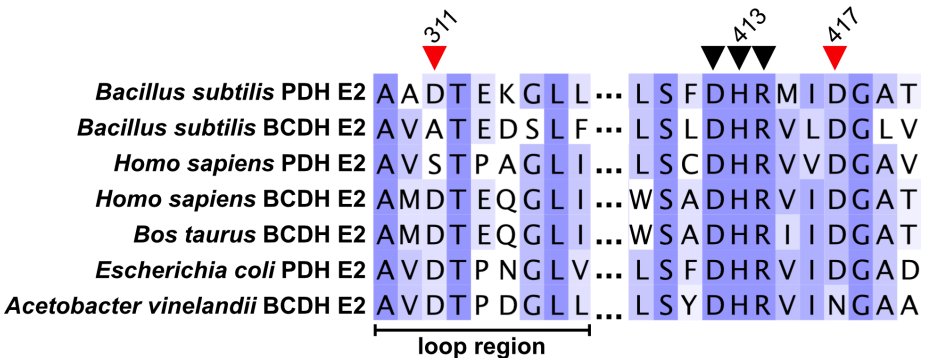

Figure 4.7: Multiple sequence alignment of E2 from different organisms. Multiple amino acid sequences of a loop region containing Asp311 and the conserved catalytic region are aligned. Conserved aspartates are indicated with red triangles. The conserved DHR sequence is indicated by black triangles.

4.8.3 Comparison of lipoamide position in the active site

Reduced lipoamide is a mimic of the natural E2 substrate: S8-acetylated lipoamide covalently attached to the LD. To elucidate details of the acetyl interaction, acetylated lipoamide mimics were soaked into the crystal, but were not observed to bind the active site. This is likely due to a weak affinity, since neither molecules contained the thiol group at C6. During this thesis, a 4 Å cryo-EM structure of LD bound to the E2 core of *E. coli* was published [138]. Figure 4.8 shows a comparison between the lipoamide position in the cryo-EM structure (blue) and the structures reported here (grey). In structures reported here, the loop region is closed and Asp311 is located in close proximity to His413, whereas the Asp311 counterpart points towards the protein surface in the cryo-EM structure. In both structures, S8 of the lipoamide is positioned close to His413, at a distance of 3.8 Å in the structures reported here and 2.5 Å in the cryo-EM structure. Evaluation of atomic distances in the PDB show a typical S-N distance of 3.5 Å, which are commonly observed in catalytic dyads of cysteine proteases [220]. This is 1.1 Å longer than the modelled distance in the cryo-EM structure [221], which is likely explained by the low resolution (4-7.5 Å) of the cryo EM structure resulting in poor lipoamide density. The main difference between the structures is the lipoamide entry point. The lipoamide attached to the LD enters the lipoamide channel in direction of the loop region, while free lipoamide enters the channel from the other side. A high resolution structure of the E2 in complex with acetylated lipoamide should provide more insights into the orientation of the acetyl group during catalysis.

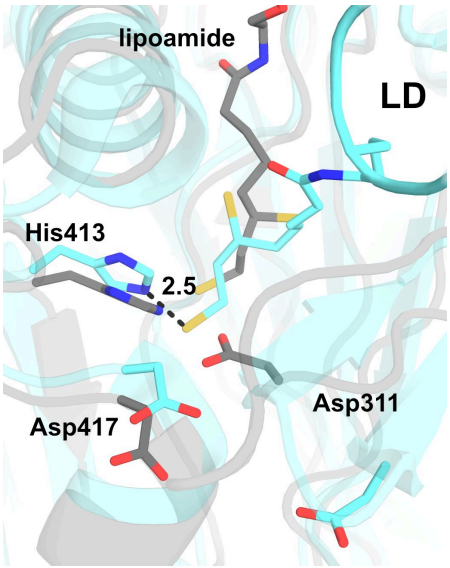

Figure 4.8: Comparison of lipoamide positions in the E2 active site. The active site of E2 complexed with free lipoamide is shown (grey) overlayed with the cryo-EM structure of the *E. coli* E2 core bound to the LD (blue) (PDB ID: 7B9K). The loop region around Asp311 shows a different conformation and lipoamide enters the active site from a different position. In both structures Asp417 and its analogue in *E. coli* are pointing away from His413. S8 of the lipoamide in the cryo-EM structure is at a distance of 2.5 Å to the His413 equivalent in *E. coli*.

4.9 A pre-oxidation intermediate trapped in the E3 active site

4.9.1 Rotation of a leucine sidechain clears the active site

The E3 enzyme is a flavin-dependent enzyme, which catalyzes the reoxidation of the reduced lipoamide following E2 catalyzed acetyl-transfer to CoA. Structural information concerning the interaction with its substrate lipoamide has not yet been elucidated. In this thesis, the substitution of a catalytic cysteine in combination with a long soak with a soluble lipoamide analogue trapped a mixed lipoamide disulfide in the active site (figure 3.29, chapter 3.14). The disulfide bond was formed between S8 of the lipoamide and the thiol group of Cys47. The interaction of Cys47 with lipoamide is expected due to its proximity towards the lipoamide channel, but this thesis provides the first structural evidence of this interaction. Lipoamide binding coincided with the formation of an alternative conformation of Leu48, whereby rotation of the sidechain by 180° about its C2α-C2β bond, which cleared the active site for the lipoamide. In E3 structures deposited in the PDB, the leucine residue samples between the open and closed conformation. Some of the E3 complexes with open conformation include *Mycobacterium tuberculosis*, human, and *Thermus thermophilus* E3 (PDB IDs:2A8X,6I4Q,2EQ6).

4.9.2 Substrate accommodation in flavin-dependent reductases

Dihydrolipoyl dehydrogenases share functional and structural similarity with other flavin-dependent oxidoreductases such as glutathione reductase. These similarities are illustrated by a structural alignment of a crystal structure of the human glutathione reductase, which is complexed with a mixed disulfide with its substrate glutathione (GSH) (figure 4.9) [222]. Residues of the E3 and glutathione reductase are depicted in blue and grey, respectively, and bound GSH molecules are depicted in grey. The similarities between the enzymes include the positions of the active site disulfide, FAD cofactor, catalytic histidine 447 and several hydrophobic residues near the active site. The positions of both sulfur atoms of the lipoamide are indicated by a red circle. S6 of the lipoamide and a GSH thiol are both accommodated by pocket formed by hydrophobic residues. These include two leucine residues and one isoleucine residue in the E3 enzyme, and one leucine residue and two valine residues in the GSH reductase. A multiple sequence alignment with different model organisms shows, that the hydrophobic residues Ile53, Leu48 and Leu99 are conserved amongst E3s of different species (figure 4.10). The residues are indicated by red triangles. The alignment covers the sequence of six amino acids that forms the conserved catalytic disulfide in the active site (indicated by black triangle). However, glutathione reductases contain valine residues in place of Leu48 and Ile53.

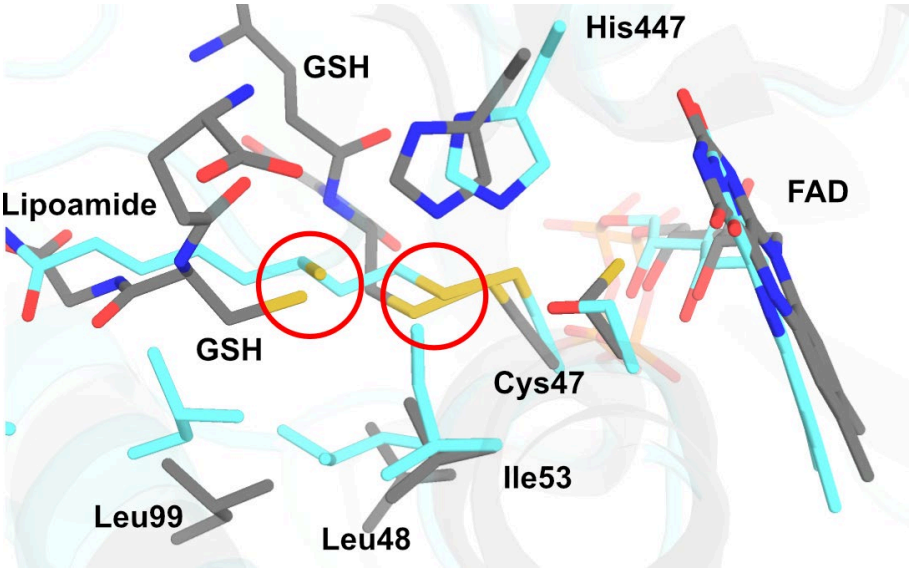

Figure 4.9: Overlay of E3 and glutathione reductase bound to lipoamide and glutathione. The E3 structure bound to lipoamide (blue) is overlayed with a structure of the human glutathione reductase complexed with its substrate glutathione (grey) (PDB ID: 1GRE). The overall active site is conserved between the oxidoreductases. Both sulfur atoms of the lipoamide are accommodated by a similar set of hydrophobic residues.

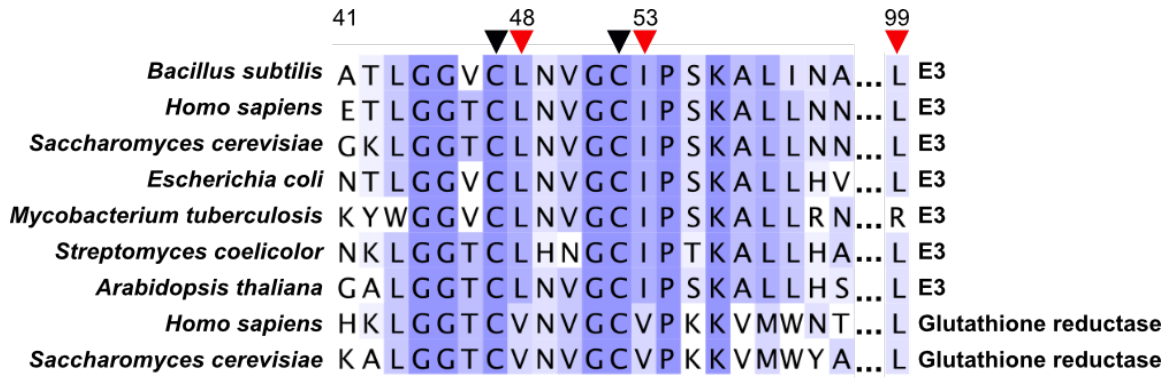

Figure 4.10: Multiple sequence alignment of E3 with different model organisms. The alignment shows the conservation of several hydrophobic residues, which accommodate lipoamide thiol groups.

The conservation amongst dihydrolipoyl dehydrogenases, and the observed open and closed conformations of Leu48 may suggest a gating function of Leu48. Many enzymes employ gating mechanisms. Active site channels, for example, are gated to restrict solvent or substrate access to redox sensitive sites [223]. A similar principle is observed in the cholesterol oxidase, another flavin-dependent enzyme. Conformations of a phenylalanine residue open or restrict access to the active site [224]. These findings show a structural conservation of how flavin-dependent oxidoreductases accommodate hydrophobic thiol groups of their respective substrates in the active site. Substitutions of Leu48 could be analyzed in kinetic experiments, to verify the potential gating mechanism.

The E3 structure complexed with the lipoamide disulfide showed a tyrosine residue hydrogen bonded to a C-terminal histidine near the active site. This tyrosine residue, Tyr22, is also conserved amongst all E3s and has been suggested to have both catalytic and structural roles [186]. Tyr22 and the C-terminal histidine form the backside of the lipoamide tunnel, however the structural evidence reported here shows that both lipoamide sulfur atoms point away from the tyrosine hydroxyl group. This therefore suggests a structural rather than catalytical role for Tyr22, at least during the first half-reaction of the E3 (the oxidation of lipoamide). The mixed disulfide shown here was only 60% occupied, therefore longer soaks could increase the occupancy, which may reveal further details of lipoamide interaction. The success of trapping redox active intermediates by long crystal soaks is illustrated by the high occupancy of glutathione in the glutathione reductase structure described earlier (PDB ID:1GRE). In that example, crystals were incubated with glutathione for up to 18 days to capture different intermediates [222]. Interestingly, the highest occupancy of lipoamide in the E3 enzyme was obtained in co-soaks with NAD^+. NAD^+ could oxidize FAD, which then favors disulfide formation in the active site. However, the residue in proximity to FAD, Cys52, was substituted with serine. Therefore, the exact mechanism behind that observation requires further clarification.

5 Conclusion and Outlook

In this thesis, the individual subunits of the *B. subtills* PDH complex were investigated by X-ray crystallography. High resolution structures of the E1, E2, and E3 were elucidated. The pyruvate decarboxylation reaction of the E1 enzyme was followed by time-resolved serial crystallography, which visualized the inherent half-of-the-sites reactivity of this enzyme. High resolution data allowed the identification of a proton wire connecting both active sites. A substrate mediated proton asymmetry was observed, which may be a driving factor in active site communication of thiamine-dependent enzymes. Several reaction intermediates were elucidated at high resolution by different cryo-trapping techniques. Amongst them were the pre-decarboxylation intermediate lactyl-ThDP, and a tautomeric mixture of post-decarboxylation intermediates. A new inhibition mechanism of fluoropyruvate was postulated based on the formation of a tricyclic ThDP form containing a seven-membered ring. High resolution structures of the E2 catalytic domain showed, how the essential prosthetic lipoyl group interacts with active site residues. This lead to the discovery of an aspartate residue, which completes the catalytic dyad upon closure of a loop region. The E3-lipoamide interaction was elucidated for the first time. The structural data showed, how flavin-dependent oxidoreductases accommodate sulfhydryl groups of their respective substrates and how a leucine residue gates the active site.

Although several reaction intermediates have been elucidated in this thesis, some questions remain unclear. There are no structural details about the interaction of the E1 with lipoamide due to its weak affinity. Therefore, the mechanism of reductive trans-acetylation catalyzed by the E1 is not fully understood. To elucidate the underlying mechanism, the mixture of post-decarboxylation intermediates observed in this thesis needs to be deconvoluted. In addition, a structure of E1 bound to the LD might give further insights into the mechanism. Furthermore, the interaction of E2 with its natural substrate, acetylated lipoamide, will give additional information about the acetyl transfer reaction. The observations of the dynamic E2 loop need to be transferred onto the full icosahedral core, preferably in complex with CoA. The occupancy of the mixed disulfide observed in the E3 can be increased by longer soaks. In addition, the same reaction can be assessed in native E3 crystals to trap other covalent adducts between lipoamide, Cys52 and FAD. Finally, a high-resolution structure of the full pyruvate dehydrogenase complex needs to be elucidated to gather insights into its subunit stoichiometry and lipoyl domain-subunit interactions.

Appendix

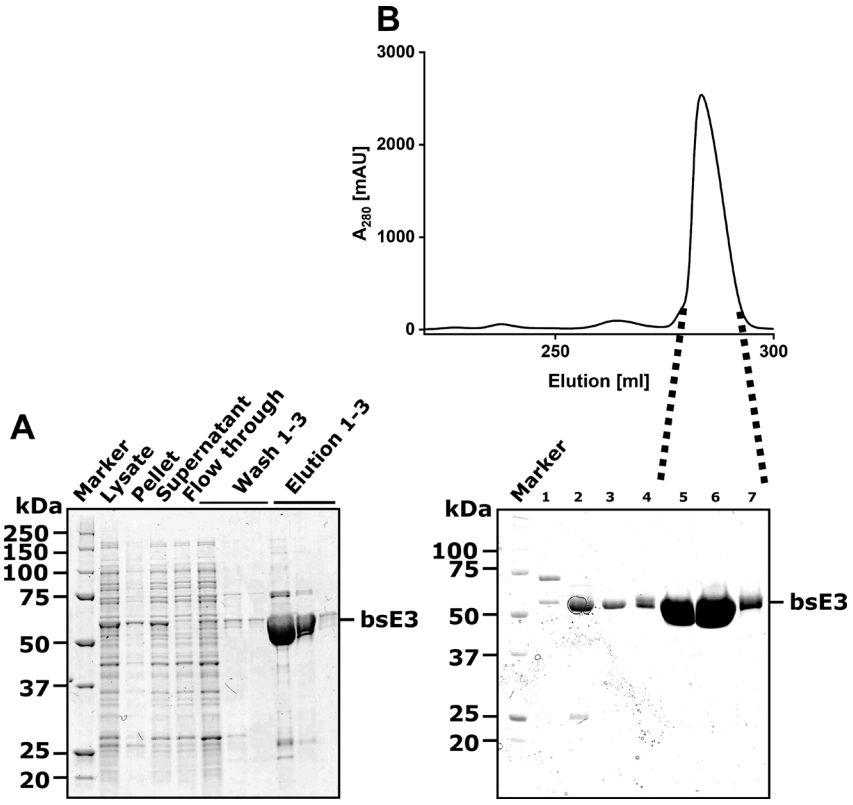

Appendix Figure 1: Purification of the *B. subtilis PDH* E3. A) The E3 was purified via Ni-NTA chromatography. A band running at 50 kDa corresponds to the E3. B) The E3 was further purified via Anion Exchange chromatography. Dotted lines represents fractions analyzed via SDS-PAGE.

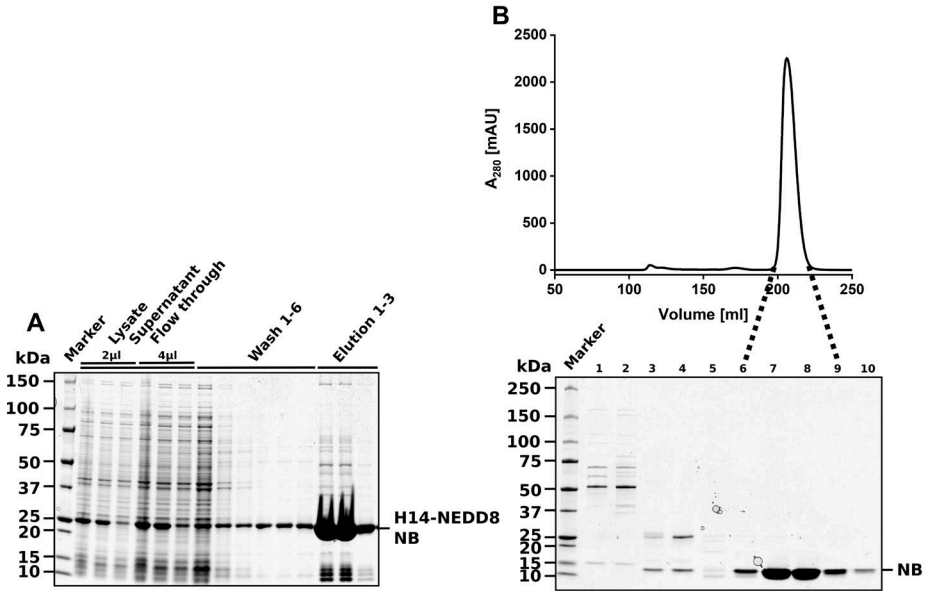

Appendix Figure 2: Purification of the alpaca nanodody. The NB was purfied via Ni-NTA chromatography (A). The tag was cleaved and the NB was further purified via size exclusion chromatography (B).

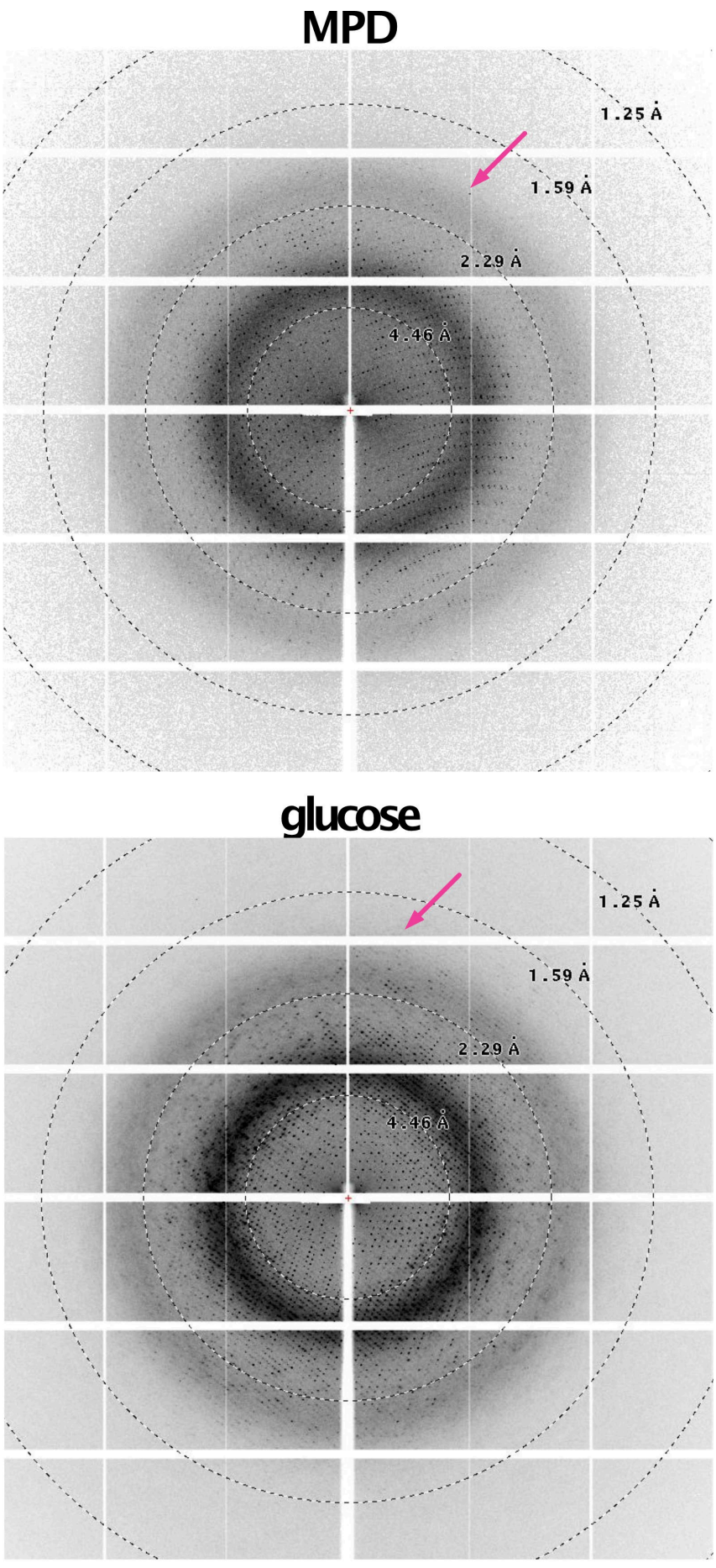

Appendix Figure 3: Diffraction pattern of E1-NB with different cryo-protectants. The arrow indicates weak reflections.

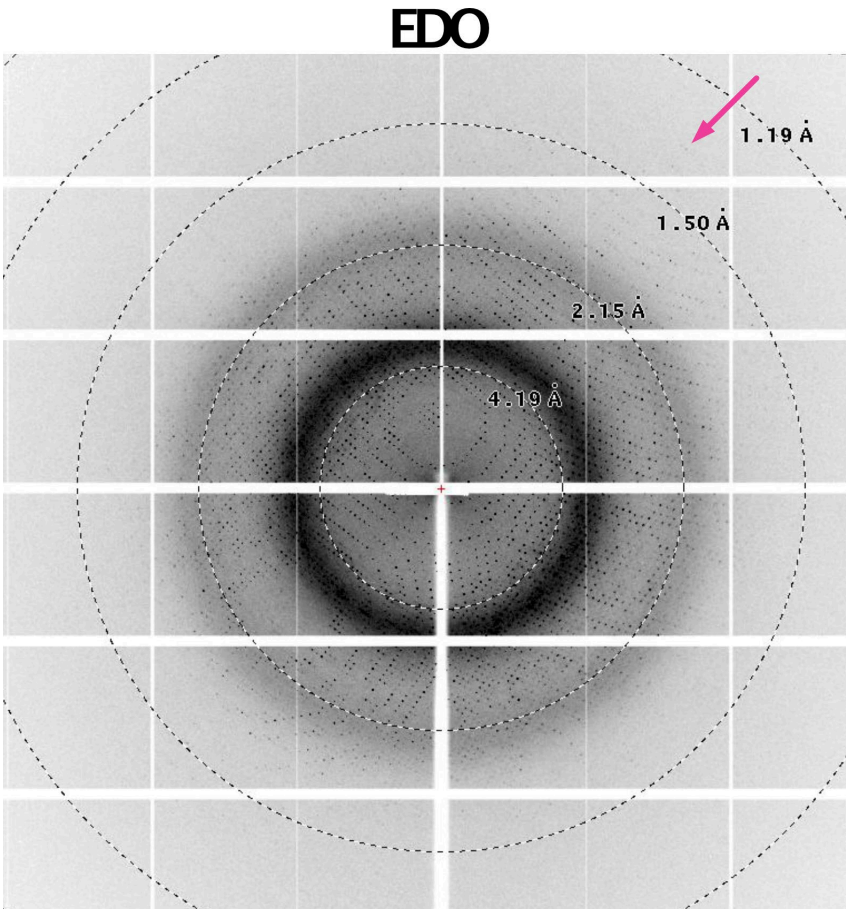

Appendix Figure 4: Diffraction pattern of an E1-NB crystals cryo-protected with EDO. The arrow indicates high-resolution reflections.

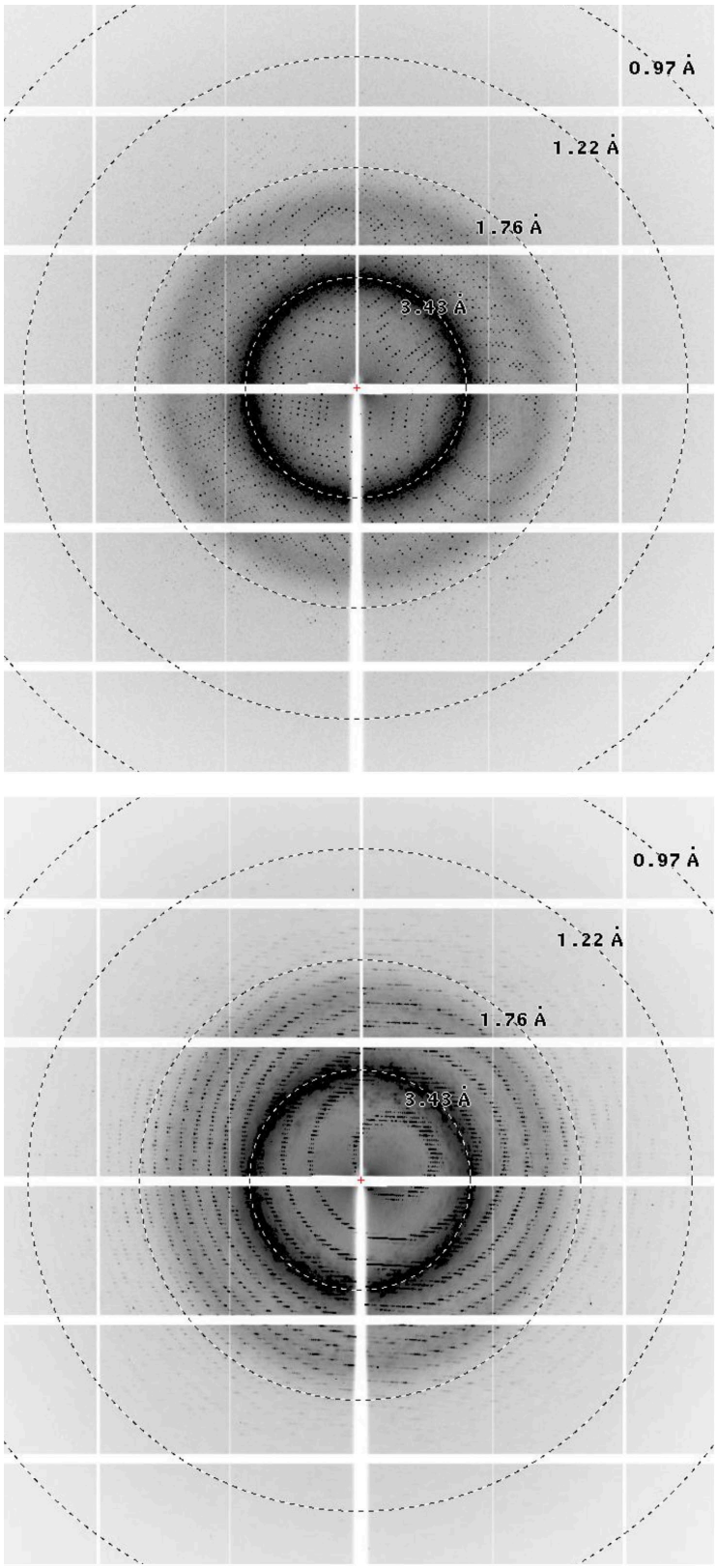

Appendix Figure 5: Diffraction pattern of crystals with different size. A diffraction pattern of a 300 µm and a 400 µm crystal is shown. The 400 µm crystal showed mosaic reflections.

Table 9: Crystallographic table 1 E1 structures part 1

Structure	**E1-NB native**	**E1-NB lactyl-ThDP**	**E1-NB carbanion-ThDP**	**E1-NB fluoro-pyruvate**
Space group	$P2_12_12$	$P2_12_12$	$P2_12_12$	$P2_12_12$
Unit cell				
a [Å]	185.9	186.1	186.9	186.5
b [Å]	101.8	102.0	102.0	101.7
c [Å]	86.7	86.8	87.1	86.9
α [°] β [°] γ [°]	90.0 90.0 90.0	90.0 90.0 90.0	90.0 90.0 90.0	90.0 90.0 90.0
Data collection				
Wavelength [Å]	0.465	0.465	0.689	0.827
Resolution range [Å]	50.42-0.95 (1.03-0.95)	62.29-1.03 (1.12-1.03)	63.73-1.03 (1.12-1.03)	93.23-1.48 (1.62-1.48)
Total reflections	29,359,087	15,105,758	17,407,535	2,823,907
Unique reflections	817,064	633,919	639,228	205,214
Multiplicity	35.9 (34.8)	23.8 (22.4)	27.2 (26.5)	13.8 (13.5)
Completeness (spherical)[%]	79.3 (18.2)	78.0 (17.7)	78.7 (17.7)	75.1 (16.5)
Completeness (ellipsoidal)[%]	97.3 (78.6)	96.9 (78.4)	97.1 (74.3)	95.8 (73.9)
Mean I/σ(I)	24.1 (1.6)	18.8 (1.7)	19.0 (1.7)	20.3 (1.6)
R_{pim}	0.015 (0.490)	0.018 (0.532)	0.015 (0.575)	0.025 (0.562)
$CC_{1/2}$	1.000 (0.697)	1.000 (0.679)	1.000 (0.676)	1.000 (0.621)
Refinement				
R_{work}	0.1060	0.1171	0.1138	0.1333
R_{free}	0.1225	0.1360	0.1333	0.1644
Number of non-hydrogen atoms				
Protein	12,619	12,619	12,607	12,623
Solvent	2,234	2,145	2,360	1,532
RMSD (bond length) [Å]	0.018	0.016	0.016	0.011
RMSD (bond angles) [°]	1.50	1.40	1.39	1.07
Mean B-factor [$Å^2$]	14.53	16.82	19.38	27.70
Wilson B [$Å^2$]	7.24	9.38	10.88	22.76
Ramachandran favored [%]	97.65	98.21	97.03	0.16
Ramachandran outliers [%]	0.25	0.12	0.2	97.51

Table 10: Crystallographic table 1 E1 structures part 2

Structure	**E1-NB MVA**	**E1-NB CAP**	**$E1_{H128}$-NB pyruvate**	**$E1_{H273N}$-NB pyruvate**
Space group	$P2_12_12$	$P2_12_12$	$P2_12_12$	$P2_12_12$
Unit cell				
a [Å]	186.0	186.3	186.2	186.4
b [Å]	101.9	101.9	101.9	102.0
c [Å]	86.8	86.9	87.0	87.1
α [°] β [°] γ [°]	90.0 90.0 90.0	90.0 90.0 90.0	90.0 90.0 90.0	90.0 90.0 90.0
Data collection				
Wavelength [Å]	0.465	0.465	0.465	0.976
Resolution range [Å]	68.69-1.04 (1.13-1.04)	86.86-1.12 (1.23-1.12)	87.04-1.39 (1.52-1.39)	93.20-1.17 (1.32-1.17)
Total reflections	18,624,556	11,378,079	3,614,515	4,790,685
Unique reflections	627,992	473,033	257,318	353,435
Multiplicity	29.7 (28.8)	24.1 (27.8)	14.0 (14.4)	13.6 (12.4)
Completeness (spherical)[%]	80.8 (19.4)	75.6 (16.0)	78.1 (17.3)	64.5 (10.9)
Completeness (ellipsoidal)[%]	96.9 (74.3)	96.8 (80.3)	96.1 (73.6)	96.0 (70.5)
Mean I/σ(I)	18.3 (1.6)	13.5 (1.5)	12.5 (1.5)	17.7 (1.9)
R_{pim}	0.022 (0.496)	0.025 (0.457)	0.034 (0.406)	0.019 (0.475)
$CC_{1/2}$	1.000 (0.671)	1.000 (0.666)	0.998 (0.668)	0.998 (0.747)
Refinement				
R_{work}	0.1148	0.1341	0.1522	0.1350
R_{free}	0.1356	0.1613	0.1869	0.1633
Number of non-hydrogen atoms				
Protein	12,619	12,619	12,602	12,619
Solvent	2,229	2,230	2,335	1,681
RMSD (bond length) [Å]	0.015	0.014	0.011	0.014
RMSD (bond angles) [°]	1.39	1.27	1.00	1.27
Mean B-factor [$Å^2$]	16.04	19.64	23.56	21.50
Wilson B [$Å^2$]	8.49	11.07	16.27	14.17
Ramachandran favored [%]	96.64	96.89	97.21	97.65
Ramachandran outliers [%]	0.28	0.42	0.15	0.16

Table 11: Crystallographic table 1 E2 structures part 1

Structure	**E1 (no nanobody)**	**E2CDsalt native ethylene glycol**	**E2CDsalt native glycerol**	**E2CDsalt lipoamide glycerol**
Space group	P1	I23	I23	I23
Unit cell				
a [Å]	80.8	117.6	118.1	118.1
b [Å]	84.4	117.6	118.1	118.1
c [Å]	98.4	117.6	118.1	118.1
α [°] β [°] γ [°]	93.2 93.8 92.2	90.0 90.0 90.0	90.0 90.0 90.0	90.0 90.0 90.0
Data collection				
Wavelength [Å]	0.976	0.540	0.976	0.976
Resolution range [Å]	84.15-1.47 (1.62-1.47)	48.03-1.08 (1.11-1.08)	83.52-1.37 (1.41-1.37)	48.22-1.34 (1.38-1.34)
Total reflections	1,145,716	4,462,776	2,253,840	2,321,350
Unique reflections	319,093	111,059	55,293	59,383
Multiplicity	3.6 (3.3)	40.2 (41.6)	40.8 (40.1)	39.1 (40.3)
Completeness (spherical)[%]	72.7 (14.3)	97.0 (62.2)	96.2 (56.4)	96.5 (58.3)
Completeness (ellipsoidal)[%]	92.8 (57.8)	97.0 (62.2)	96.2 (56.4)	96.5 (58.3)
Mean I/σ(I)	11.2 (1.8)	27.5 (1.4)	20.1 (1.4)	28.2 (1.3)
R_{pim}	0.048 (0.703)	0.010 (0.519)	0.015 (0.567)	0.011 (0.502)
$CC_{1/2}$	0.998 (0.434)	1.000 (0.607)	0.998 (0.687)	0.999 (0.685)
Refinement				
R_{work}	0.1551	0.1325	0.1489	0.1580
R_{free}	0.1921	0.1380	0.1746	0.1655
Number of non-hydrogen atoms				
Protein	21,490	1,777	1,799	1,799
Solvent	2226	261	200	189
RMSD (bond length) [Å]	0.011	0.016	0.012	0.011
RMSD (bond angles) [°]	1.09	1.54	1.21	1.18
Mean B-factor [$Å^2$]	25.18	21.77	30.15	31.62
Wilson B [$Å^2$]	20.29	13.25	21.97	23.68
Ramachandran favored [%]	97.00	94.17	96.14	96.37
Ramachandran outliers [%]	0.41	2.5	0.48	1.04

Table 12: Crystallographic table 1 E2 structures part 2

Structure	**E2CDsalt lipoamide ethylene glycol**	**E2CDsalt 8AO ethylene glycol**	**E2CDsalt 6AH ethylene glycol**	**E2CDpeg CoA**
Space group	I23	I23	I23	$P2_1$
Unit cell				
a [Å]	117.7	117.7	117.5	72.1
b [Å]	117.7	117.7	117.5	164.0
c [Å]	117.7	117.7	117.5	73.1
α [°] β [°] γ [°]	90.0 90.0 90.0	90.0 90.0 90.0	90.0 90.0 90.0	90.0 118.2 90.0
Data collection				
Wavelength [Å]	0.775	0.689	0.540	0.976
Resolution range [Å]	58.84-1.11 (1.14-1.11)	48.05-1.07 (1.10-1.07)	58.77-1.14 (1.17-1.14)	62.29-1.86 (2.04-1.86)
Total reflections	4,185,822	4,614,128	3,854,349	619,816
Unique reflections	102,356	116,176	94,871	87,860
Multiplicity	40.9 (41.9)	39.7 (40.1)	40.6 (43.0)	7.1 (7.3)
Completeness (spherical)[%]	97.1 (63.7)	97.3 (64.0)	96.7 (61.0)	69.9 (14.3)
Completeness (ellipsoidal)[%]	97.1 (63.9)	97.3 (64.0)	96.7 (61.0)	94.0 (69.7)
Mean I/σ(I)	32.7 (1.4)	28.2 (1.4)	27.8 (1.5)	18.8 (1.7)
R_{pim}	0.010 (0.533)	0.010 (0.504)	0.011 (0.528)	0.019 (0.445)
$C_{C1/2}$	1.000 (0.606)	1.000 (0.595)	1.000 (0.603)	0.999 (0.680)
Refinement				
R_{work}	0.1247	0.1368	0.1297	0.2113
R_{free}	0.1427	0.1524	0.1405	0.2336
Number of non-hydrogen atoms				
Protein	1,777	1,799	1,777	10,216
Solvent	239	237	240	584
RMSD (bond length) [Å]	0.016	0.015	0.014	0.009
RMSD (bond angles) [°]	1.85	1.45	1.40	1.03
Mean B-factor [$Å^2$]	22.01	21.75	22.70	55.53
Wilson B [$Å^2$]	13.58	12.55	15.10	42.88
Ramachandran favored [%]	94.92	95.24	94.17	96.16
Ramachandran outliers [%]	2.54	0.95	1.67	0.63

Table 13: Crystallographic table 1 E3 structures

Structure	**E3 native**	**E3$_{C52S}$**	**E3$_{C52S}$ lipoamide +NAD$^+$**
Space group	$I4_1$	$I4_1$	$I4_1$
Unit cell			
a [Å]	132.2	132.0	132.4
b [Å]	132.2	132.0	132.4
c [Å]	63.3	63.4	62.8
α [°] β [°] γ [°]	90.0 90.0 90.0	90.0 90.0 90.0	90.0 90.0 90.0
Data collection			
Wavelength [Å]	0.976	0.465	0.465
Resolution range [Å]	66.12-1.63 (1.73-1.63)	93.35-1.69 (1.81-1.69)	93.63-1.61 (1.70-1.61)
Total reflections	393,621	1,302,411	1,653,888
Unique reflections	49,949	44,484	56,451
Multiplicity	7.9 (7.9)	29.3 (29.5)	29.3 (29.1)
Completeness (spherical)[%]	73.5 (22.7)	72.7 (20.2)	80.0 (26.4)
Completeness (ellipsoidal)[%]	93.7 (72.9)	94.0 (66.2)	94.5 (72.2)
Mean I/σ(I)	12.8 (1.5)	15.5 (1.4)	18.6 (1.5)
R_{pim}	0.024 (0.514)	0.018 (0.472)	0.016 (0.445)
$CC_{1/2}$	0.993 (0.678)	1.000 (0.638)	1.000 (0.694)
Refinement			
R_{work}	0.1857	0.1861	0.1674
R_{free}	0.2009	0.2078	0.1940
Number of non-hydrogen atoms			
Protein	3,461	3461	3462
Solvent	484	444	497
RMSD (bond length) [Å]	0.009	0.009	0.010
RMSD (bond angles) [°]	1.11	1.10	1.33
Mean B-factor [Å^2]	26.80	26.00	23.30
Wilson B [Å^2]	34.24	35.96	30.93
Ramachandran favored [%]	93.01	92.79	93.57
Ramachandran outliers [%]	2.18	1.75	1.03

Table 14: Crystallographic table 1 TRX structures part 1

Structure	**E1-NB DARK TRX**	**E1-NB 0.2 s TRX (HARE 5)**	**E1-NB 0.4 s TRX (HARE 10)**	**E1-NB 1.1s TRX (HARE 20)**
Space group	$P2_12_12$	$P2_12_12$	$P2_12_12$	$P2_12_12$
Unit cell				
a [Å]	187.0	187.0	187.0	187.0
b [Å]	102.0	102.0	102.0	102.0
c [Å]	86.0	86.0	86.0	86.0
α [°] β [°] γ [°]	90 90 90	90 90 90	90 90 90	90 90 90
Data collection				
Wavelength [Å]	0.976	0.976	0.976	0.976
Resolution range [Å]	8.24-2.31	8.24-2.61	8.24-2.31	8.24-2.44
Number of hits	13,204	5,837	13,004	13,384
Hit rate [%]	51.6	22.8	50.8	52.3
Total reflections	14,335,601	4,403,312	16,751,230	14,670,823
Unique reflections	111,686	111,683	111,686	111,687
Multiplicity	128.4 (99.7)	39.4 (34.3)	150 (116.4)	131.4 (107.6)
Completeness [%]	100 (100)	100 (100)	100 (100)	100 (100)
SNR	2.25 (0.53)	1.23 (0.55)	2.34 (0.52)	2.07 (0.40)
R_{split} [%]	26.25 (215.93)	48.37 (218.43)	25.07 (221.49)	25.50 (285.84)
CC*	0.987 (0.519)	0.970 (0.527)	0.989 (0.0.479)	0.990 (0.409)
Refinement				
R_{work}	0.1592	0.1769	0.1546	0.1433
R_{free}	0.2214	0.2489	0.2136	0.1909
Number of non-hydrogen atoms	14,296	14,296	14,296	14,302
RMSD (bond length) [Å]	0.008	0.005	0.007	0.007
RMSD (bond angles) [°]	1.46	1.13	1.266	1.29
Mean B-factor [Å^2]	52.34	51.8	49.6	60.59
Ramachandran favored [%]	94.74	94.49	95.36	94.37
Ramachandran outliers [%]	0.56	0.87	0.56	0.62

Table 15: Crystallographic table 1 TRX structures part 2

Structure	**E1-NB 1.9s TRX (HARE 40)**	**E1-NB 4.8 s TRX (HARE 100)**	**E1-NB 7.7 s TRX (HARE 200)**	**E1-NB 38.1 s TRX (HARE 800)**
Space group	$P2_12_12$	$P2_12_12$	$P2_12_12$	$P2_12_12$
Unit cell				
a [Å]	187.0	187.0	187.0	187.0
b [Å]	102.0	102.0	102.0	102.0
c [Å]	86.0	86.0	86.0	86.0
α [°] β [°] γ [°]	90 90 90	90 90 90	90 90 90	90 90 90
Data collection				
Wavelength [Å]	0.976	0.976	0.976	0.976
Resolution range [Å]	8.24-2.44	8.24-2.61	8.24-2.44	8.24-2.84
Number of hits	12,972	13,211	8,518	4,439
Hit rate [%]	50.7	51.6	33.3	20.4
Total reflections	14,823,061	13,878,495	7,239,697	3,730,378
Unique reflections	111,687	111,686	111,686	111,681
Multiplicity	132.7 (108.8)	124.3 (108.3)	64.8 (52.9)	33.4 (31.6)
Completeness [%]	100 (100)	100 (100)	100 (100)	100 (100)
SNR	2.04 (0.38)	1.90 (0.54)	1.55 (0.39)	0.972 (0.48)
R_{split}	25.77 (294.41)	27.81 (212.61)	38.43 (307.26)	57.55 (251.23)
CC*	0.991 (0.413)	0.991 (0.566)	0.981 (0.402)	0.978 (0.472)
Refinement				
R_{work}	0.1508	0.1613	0.1694	0.1847
R_{free}	0.2355	0.2251	0.2316	0.2524
Number of non-hydrogen atoms	14,302	14,302	14,305	14,296
RMSD (bond length) [Å]	0.006	0.006	0.005	0.006
RMSD (bond angles) [°]	1.19	1.18	1.15	1.35
Mean B-factor [Å^2]	62.17	67.73	53.66	71.99
Ramachandran favored [%]	94.74	94.30	95.29	93.37
Ramachandran outliers [%]	0.80	0.74	0.80	0.80

References

[1] J. Rudolph and J. Stubbe, “Investigation of the Mechanism of Phosphoribosylamine Transfer from Glutamine Phosphoribosylpyrophosphate Amidotransferase to Glycinamide Ribonucleotide Synthetase,” *Biochemistry*, vol. 34, no. 7, pp. 2241–2250, Feb. 1995, doi: 10.1021/bi00007a019.

[2] Richard Nelson Perham, “Self-assembly of biological macromolecules,” *Philosophical Transactions of the Royal Society of London. B, Biological Sciences*, vol. 272, no. 915, pp. 123–136, Nov. 1975, doi: 10.1098/rstb.1975.0075.

[3] J. L. S. Milne, “Molecular architecture and mechanism of an icosahedral pyruvate dehydrogenase complex: a multifunctional catalytic machine,” *EMBO J*, vol. 21, no. 21, pp. 5587–5598, Nov. 2002, doi: 10.1093/emboj/cdf574.

[4] V. Jagannathan and R. S. Schweet, “Pyruvic oxidase of pigeon breast muscle: I. Purification and properties of the enzyme,” *Journal of Biological Chemistry*, vol. 196, no. 2, pp. 551–562, Jun. 1952, doi: 10.1016/S0021-9258(19)52389-4.

[5] M. Koike, L. J. Reed, and W. R. Carroll, “α-Keto Acid Dehydrogenation Complexes,” *Journal of Biological Chemistry*, vol. 235, no. 7, pp. 1924–1930, Jul. 1960, doi: 10.1016/S0021-9258(18)69337-8.

[6] C. Chinopoulos, “Which way does the citric acid cycle turn during hypoxia? The critical role of α-ketoglutarate dehydrogenase complex,” *J Neurosci Res*, vol. 91, no. 8, pp. 1030–1043, Aug. 2013, doi: 10.1002/jnr.23196.

[7] K.-F. Rex Sheu and J. P. Blass, “The alpha-Ketoglutarate Dehydrogenase Complex,” *Ann N Y Acad Sci*, vol. 893, no. 1, pp. 61–78, Nov. 1999, doi: 10.1111/j.1749-6632.1999.tb07818.x.

[8] M. M. Adeva-Andany, L. López-Maside, C. Donapetry-García, C. Fernández-Fernández, and C. Sixto-Leal, “Enzymes involved in branched-chain amino acid metabolism in humans,” *Amino Acids*, vol. 49, no. 6, pp. 1005–1028, Jun. 2017, doi: 10.1007/s00726-017-2412-7.

[9] P. Blackburn *et al.*, “Maple syrup urine disease: mechanisms and management,” *Appl Clin Genet*, vol. Volume 10, pp. 57–66, Sep. 2017, doi: 10.2147/TACG.S125962.

[10] C. Eymann *et al.*, “A comprehensive proteome map of growing Bacillus subtilis cells.,” *Proteomics*, vol. 4, no. 10, pp. 2849–76, Oct. 2004, doi: 10.1002/pmic.200400907.

[11] M. S. Patel and T. E. Roche, “Molecular biology and biochemistry of pyruvate dehydrogenase complexes.,” *FASEB J*, vol. 4, no. 14, pp. 3224–33, Nov. 1990, doi: 10.1096/fasebj.4.14.2227213.

[12] L. J. Reed, “A trail of research from lipoic acid to alpha-keto acid dehydrogenase complexes.,” *J Biol Chem*, vol. 276, no. 42, pp. 38329–36, Oct. 2001, doi: 10.1074/jbc.R100026200.

[13] P. A. Srere, “The molecular physiology of citrate.,” *Curr Top Cell Regul*, vol. 33, pp. 261–75, 1992, doi: 10.1016/b978-0-12-152833-1.50020-4.

[14] K. P. Patel, T. W. O’Brien, S. H. Subramony, J. Shuster, and P. W. Stacpoole, “The spectrum of pyruvate dehydrogenase complex deficiency: Clinical, biochemical and genetic features in 371 patients,” *Mol Genet Metab*, vol. 106, no. 3, pp. 385–394, Jul. 2012, doi: 10.1016/j.ymgme.2012.03.017.

[15] G. K. Brown, L. J. Otero, M. LeGris, and R. M. Brown, “Pyruvate dehydrogenase deficiency.,” *J Med Genet*, vol. 31, no. 11, pp. 875–879, Nov. 1994, doi: 10.1136/jmg.31.11.875.

[16] T. Birkenstock *et al.*, “Exometabolome Analysis Identifies Pyruvate Dehydrogenase as a Target for the Antibiotic Triphenylbismuthdichloride in Multiresistant Bacterial Pathogens,” *Journal of Biological Chemistry*, vol. 287, no. 4, pp. 2887–2895, Jan. 2012, doi: 10.1074/jbc.M111.288894.

[17] L. J. Reed, “Multienzyme complexes,” *Acc Chem Res*, vol. 7, no. 2, pp. 40–46, Feb. 1974, doi: 10.1021/ar50074a002.

[18] L. J. Reed and M. L. Hackert, “Structure-function relationships in dihydrolipoamide acyltransferases.,” *J Biol Chem*, vol. 265, no. 16, pp. 8971–4, Jun. 1990.

[19] R. N. Perham, “Swinging Arms and Swinging Domains in Multifunctional Enzymes: Catalytic Machines for Multistep Reactions,” *Annu Rev Biochem*, vol. 69, no. 1, pp. 961–1004, Jun. 2000, doi: 10.1146/annurev.biochem.69.1.961.

[20] T. Izard *et al.*, “Principles of quasi-equivalence and Euclidean geometry govern the assembly of cubic and dodecahedral cores of pyruvate dehydrogenase complexes,” *Proceedings of the National Academy of Sciences*, vol. 96, no. 4, pp. 1240–1245, Feb. 1999, doi: 10.1073/pnas.96.4.1240.

[21] J. D. Green, R. N. Perham, S. J. Ullrich, and E. Appella, “Conformational studies of the interdomain linker peptides in the dihydrolipoyl acetyltransferase component of the pyruvate dehydrogenase multienzyme complex of Escherichia coli.,” *Journal of Biological Chemistry*, vol. 267, no. 33, pp. 23484–23488, Nov. 1992, doi: 10.1016/S0021-9258(18)35864-2.

[22] M. Rahmatullah, S. Gopalakrishnan, P. C. Andrews, C. L. Chang, G. A. Radke, and T. E. Roche, “Subunit Associations in the Mammalian Pyruvate Dehydrogenase Complex,” *Journal of Biological Chemistry*, vol. 264, no. 4, pp. 2221–2227, Feb. 1989, doi: 10.1016/S0021-9258(18)94165-7.

[23] G. Kikuchi, Y. Motokawa, T. Yoshida, and K. Hiraga, “Glycine cleavage system: reaction mechanism, physiological significance, and hyperglycinemia.,” *Proc Jpn Acad Ser B Phys Biol Sci*, vol. 84, no. 7, pp. 246–63, 2008, doi: 10.2183/pjab.84.246.

[24] I. A. D. Lessard, G. J. Domingo, A. Borges, and R. N. Perham, “Expression of genes encoding the E2 and E3 components of the Bacillus stearothermophilus pyruvate dehydrogenase complex and the stoichiometry of subunit interaction in assembly in vitro,” *Eur J Biochem*, vol. 258, no. 2, pp. 491–501, Dec. 1998, doi: 10.1046/j.1432-1327.1998.2580491.x.

[25] D. S. Goodsell, “Pyruvate Dehydrogenase Complex,” *RCSB Protein Data Bank*, Sep. 2012, doi: 10.2210/rcsb_pdb/mom_2012_9.

[26] D.L Nelson and M. M. Cox, *Lehninger principles of biochemistry*, 7th ed. 2017.

[27] C. E. Henderson and R. N. Perham, “Purificaton of the pyruvate dehydrogenase multienzyme complex of *Bacillus stearothermophilus* and resolution of its four component polypeptides,” *Biochemical Journal*, vol. 189, no. 1, pp. 161–172, Jul. 1980, doi: 10.1042/bj1890161.

[28] H. Ogasawara, Y. Ishida, K. Yamada, K. Yamamoto, and A. Ishihama, “PdhR (pyruvate dehydrogenase complex regulator) controls the respiratory electron transport system in Escherichia coli.,” *J Bacteriol*, vol. 189, no. 15, pp. 5534–41, Aug. 2007, doi: 10.1128/JB.00229-07.

[29] S. J. Yeaman *et al.*, “Sites of phosphorylation on pyruvate dehydrogenase from bovine kidney and heart.,” *Biochemistry*, vol. 17, no. 12, pp. 2364–70, Jun. 1978, doi: 10.1021/bi00605a017.

[30] M. S. Patel and L. G. Korotchkina, “Regulation of the pyruvate dehydrogenase complex.,” *Biochem Soc Trans*, vol. 34, no. Pt 2, pp. 217–22, Apr. 2006, doi: 10.1042/BST20060217.

[31] J. Liang, Q. Han, Y. Tan, H. Ding, and J. Li, “Current Advances on Structure-Function Relationships of Pyridoxal 5′-Phosphate-Dependent Enzymes,” *Front Mol Biosci*, vol. 6, Mar. 2019, doi: 10.3389/fmolb.2019.00004.

[32] X.-Y. Pei, K. M. Erixon, B. F. Luisi, and F. J. Leeper, “Structural insights into the prereaction state of pyruvate decarboxylase from Zymomonas mobilis .,” *Biochemistry*, vol. 49, no. 8, pp. 1727–36, Mar. 2010, doi: 10.1021/bi901864j.

[33] V. I. Bunik, A. Tylicki, and N. v. Lukashev, “Thiamin diphosphate-dependent enzymes: from enzymology to metabolic regulation, drug design and disease models,” *FEBS Journal*, vol. 280, no. 24, pp. 6412–6442, Dec. 2013, doi: 10.1111/febs.12512.

[34] M. Casteels, M. Sniekers, P. Fraccascia, G. P. Mannaerts, and P. P. Van Veldhoven, “The role of 2-hydroxyacyl-CoA lyase, a thiamin pyrophosphate-dependent enzyme, in the peroxisomal metabolism of 3-methyl-branched fatty acids and 2-hydroxy straight-chain fatty acids,” *Biochem Soc Trans*, vol. 35, no. 5, pp. 876–880, Nov. 2007, doi: 10.1042/BST0350876.

[35] L. A. Highbarger, J. A. Gerlt, and G. L. Kenyon, “Mechanism of the reaction catalyzed by acetoacetate decarboxylase. Importance of lysine 116 in determining the pKa of active-site lysine 115.,” *Biochemistry*, vol. 35, no. 1, pp. 41–6, Jan. 1996, doi: 10.1021/bi9518306.

[36] L. M. Hinman and J. P. Blass, “An NADH-linked spectrophotometric assay for pyruvate dehydrogenase complex in crude tissue homogenates.,” *J Biol Chem*, vol. 256, no. 13, pp. 6583–6, Jul. 1981.

[37] W. Langenbeck and R. Hutschenreuter, “Über organische Katalysatoren. IV. Die Decarboxylierung der Phenylglyoxylsäure und Brenztraubensäure Mit 5 Figuren im Text,” *Z Anorg Allg Chem*, vol. 188, no. 1, pp. 1–13, Mar. 1930, doi: 10.1002/zaac.19301880102.

[38] R. W. Hanson, “Decarboxylation of a keto acids,” *J Chem Educ*, vol. 64, no. 7, p. 591, Jul. 1987, doi: 10.1021/ed064p591.

[39] R. Kourist, J.-K. Guterl, K. Miyamoto, and V. Sieber, “Enzymatic Decarboxylation-An Emerging Reaction for Chemicals Production from Renewable Resources,” *ChemCatChem*, vol. 6, no. 3, pp. 689–701, Mar. 2014, doi: 10.1002/cctc.201300881.

[40] S. R. Marsden, D. G. G. McMillan, and U. Hanefeld, “Assessing the Thiamine Diphosphate Dependent Pyruvate Dehydrogenase E1 Subunit for Carboligation Reactions with Aliphatic Ketoacids.,” *Int J Mol Sci*, vol. 21, no. 22, Nov. 2020, doi: 10.3390/ijms21228641.

[41] X. Y. Pei, C. M. Titman, R. A. W. Frank, F. J. Leeper, and B. F. Luisi, “Snapshots of Catalysis in the E1 Subunit of the Pyruvate Dehydrogenase Multienzyme Complex,” *Structure*, vol. 16, no. 12, pp. 1860–1872, Dec. 2008, doi: 10.1016/j.str.2008.10.009.

[42] S. Kale, P. Arjunan, W. Furey, and F. Jordan, “A Dynamic Loop at the Active Center of the Escherichia coli Pyruvate Dehydrogenase Complex E1 Component Modulates Substrate Utilization and Chemical Communication with the E2 Component,” *Journal of Biological Chemistry*, vol. 282, no. 38, pp. 28106–28116, Sep. 2007, doi: 10.1074/jbc.M704326200.

[43] R. Breslow, “Rapid deuterium exchange in thiazolium salts,” *J Am Chem Soc*, vol. 79, no. 7, pp. 1762–1763, Apr. 1957, doi: 10.1021/ja01564a064.

[44] R. Breslow, “On the Mechanism of Thiamine Action. IV. Evidence from Studies on Model Systems,” *J Am Chem Soc*, vol. 80, no. 14, pp. 3719–3726, Jul. 1958, doi: 10.1021/ja01547a064.

[45] M. W. Washabaugh and W. P. Jencks, “Thiazolium C(2)-proton exchange: structure-reactivity correlations and the pKa of thiamin C(2)-H revisited,” *Biochemistry*, vol. 27, no. 14, pp. 5044–5053, Jul. 1988, doi: 10.1021/bi00414a015.
[46] D. Kern *et al.*, “How thiamine diphosphate is activated in enzymes.,” *Science*, vol. 275, no. 5296, pp. 67–70, Jan. 1997, doi: 10.1126/science.275.5296.67.
[47] D. Meyer, P. Neumann, R. Ficner, and K. Tittmann, “Observation of a stable carbene at the active site of a thiamin enzyme,” *Nat Chem Biol*, vol. 9, no. 8, pp. 488–490, Aug. 2013, doi: 10.1038/nchembio.1275.
[48] R. Kluger and K. Tittmann, “Thiamin Diphosphate Catalysis: Enzymic and Nonenzymic Covalent Intermediates,” *Chem Rev*, vol. 108, no. 6, pp. 1797–1833, Jun. 2008, doi: 10.1021/cr068444m.
[49] D. S. Flournoy and P. A. Frey, “Inactivation of the pyruvate dehydrogenase complex of Escherichia coli by fluoropyruvate.,” *Biochemistry*, vol. 28, no. 25, pp. 9594–602, Dec. 1989, doi: 10.1021/bi00451a007.
[50] P. A. Frey, “2-Acetylthiamin pyrophosphate: an enzyme-bound intermediate in thiamin pyrophosphate-dependent reactions.,” *Biofactors*, vol. 2, no. 1, pp. 1–9, Mar. 1989.
[51] P. A. Frey, D. S. Flournoy, K. Gruys, and Y. S. Yang, “Intermediates in reductive transacetylation catalyzed by pyruvate dehydrogenase complex.,” *Ann N Y Acad Sci*, vol. 573, pp. 21–35, 1989, doi: 10.1111/j.1749-6632.1989.tb14984.x.
[52] M. L. DAS, M. KOIKE, and L. J. REED, “On the role of thiamine pyrophosphate in oxidative decarboxylation of alpha-keto acids.,” *Proc Natl Acad Sci U S A*, vol. 47, no. 6, pp. 753–9, Jun. 1961, doi: 10.1073/pnas.47.6.753.
[53] F. G. White and L. L. Ingraham, “Mechanism of Thiamine Action: a Model of 2-Acylthiamine,” *J Am Chem Soc*, vol. 84, no. 16, pp. 3109–3111, Aug. 1962, doi: 10.1021/ja00875a015.
[54] C. C. Chiu, A. Chung, G. Barletta, and F. Jordan, “Intramolecular Model for the Reductive Acyl Transfer Catalyzed by α-Keto Acid Dehydrogenases,” *J Am Chem Soc*, vol. 118, no. 45, pp. 11026–11029, Nov. 1996, doi: 10.1021/ja954322s.
[55] A. Levitzki, W. B. Stallcup, and D. E. Koshland, “Half-of-the-sites reactivity and conformational states of cytidine triphosphate synthetase,” *Biochemistry*, vol. 10, no. 18, pp. 3371–3378, Aug. 1971, doi: 10.1021/bi00794a009.
[56] S. A. Bernhard, M. F. Dunn, P. L. Luisi, and P. Schack, “Mechanistic studies on equine liver alcohol dehydrogenase. I. The stoichiometry relationship of the coenzyme binding sites to the catalytic sites active in the reduction of aromatic aldehydes in the transient state.,” *Biochemistry*, vol. 9, no. 1, pp. 185–92, Jan. 1970, doi: 10.1021/bi00803a024.
[57] M. Vivoli, J. Pang, and N. J. Harmer, “A half-site multimeric enzyme achieves its cooperativity without conformational changes,” *Sci Rep*, vol. 7, no. 1, p. 16529, Nov. 2017, doi: 10.1038/s41598-017-16421-2.
[58] L. S. Khailova and L. G. Korochkina, “Half-of-the-site reactivity of the decarboxylating component of the pyruvate dehydrogenase complex from pigeon breast muscle with respect to 2-hydroxyethyl thiamine pyrophosphate.,” *Biochem Int*, vol. 11, no. 4, pp. 509–16, Oct. 1985.
[59] F. Seifert *et al.*, “Direct Kinetic Evidence for Half-Of-The-Sites Reactivity in the E1 Component of the Human Pyruvate Dehydrogenase Multienzyme Complex through Alternating Sites Cofactor Activation,” *Biochemistry*, vol. 45, no. 42, pp. 12775–12785, Oct. 2006, doi: 10.1021/bi061582l.
[60] K. Schröder-Tittmann *et al.*, “Alternating Sites Reactivity Is a Common Feature of Thiamin Diphosphate-Dependent Enzymes As Evidenced by Isothermal Titration

Calorimetry Studies of Substrate Binding," *Biochemistry*, vol. 52, no. 15, pp. 2505–2507, Apr. 2013, doi: 10.1021/bi301591e.

[61] E. M. Ciszak, L. G. Korotchkina, P. M. Dominiak, S. Sidhu, and M. S. Patel, "Structural Basis for Flip-Flop Action of Thiamin Pyrophosphate-dependent Enzymes Revealed by Human Pyruvate Dehydrogenase," *Journal of Biological Chemistry*, vol. 278, no. 23, pp. 21240–21246, Jun. 2003, doi: 10.1074/jbc.M300339200.

[62] R. A. W. Frank, C. M. Titman, J. V. Pratap, B. F. Luisi, and R. N. Perham, "A Molecular Switch and Proton Wire Synchronize the Active Sites in Thiamine Enzymes," *Science (1979)*, vol. 306, no. 5697, pp. 872–876, Oct. 2004, doi: 10.1126/science.1101030.

[63] S. Dai *et al.*, "Low-barrier hydrogen bonds in enzyme cooperativity," *Nature*, vol. 573, no. 7775, pp. 609–613, Sep. 2019, doi: 10.1038/s41586-019-1581-9.

[64] W. W. Cleland, P. A. Frey, and J. A. Gerlt, "The Low Barrier Hydrogen Bond in Enzymatic Catalysis," *Journal of Biological Chemistry*, vol. 273, no. 40, pp. 25529–25532, Oct. 1998, doi: 10.1074/jbc.273.40.25529.

[65] S. Yamaguchi *et al.*, "Low-barrier hydrogen bond in photoactive yellow protein," *Proceedings of the National Academy of Sciences*, vol. 106, no. 2, pp. 440–444, Jan. 2009, doi: 10.1073/pnas.0811882106.

[66] C. S. Cassidy, J. Lin, and P. A. Frey, "A New Concept for the Mechanism of Action of Chymotrypsin: The Role of the Low-Barrier Hydrogen Bond," *Biochemistry*, vol. 36, no. 15, pp. 4576–4584, Apr. 1997, doi: 10.1021/bi962013o.

[67] P. Kuhn, M. Knapp, S. M. Soltis, G. Ganshaw, M. Thoene, and R. Bott, "The 0.78 Å Structure of a Serine Protease: *Bacillus lentus* Subtilisin ," *Biochemistry*, vol. 37, no. 39, pp. 13446–13452, Sep. 1998, doi: 10.1021/bi9813983.

[68] P. A. Frey, S. A. Whitt, and J. B. Tobin, "A Low-Barrier Hydrogen Bond in the Catalytic Triad of Serine Proteases," *Science (1979)*, vol. 264, no. 5167, pp. 1927–1930, Jun. 1994, doi: 10.1126/science.7661899.

[69] S. Lüdtke *et al.*, "Sub-ångström-resolution crystallography reveals physical distortions that enhance reactivity of a covalent enzymatic intermediate.," *Nat Chem*, vol. 5, no. 9, pp. 762–7, Sep. 2013, doi: 10.1038/nchem.1728.

[70] R. A. W. Frank, J. V. Pratap, X. Y. Pei, R. N. Perham, and B. F. Luisi, "The Molecular Origins of Specificity in the Assembly of a Multienzyme Complex," *Structure*, vol. 13, no. 8, pp. 1119–1130, Aug. 2005, doi: 10.1016/j.str.2005.04.021.

[71] S. S. Mande, S. Sarfaty, M. D. Allen, R. N. Perham, and W. G. Hol, "Protein–protein interactions in the pyruvate dehydrogenase multienzyme complex: dihydrolipoamide dehydrogenase complexed with the binding domain of dihydrolipoamide acetyltransferase," *Structure*, vol. 4, no. 3, pp. 277–286, Mar. 1996, doi: 10.1016/S0969-2126(96)00032-9.

[72] F. Dardel, A. L. Davis, E. D. Laue, and R. N. Perham, "Three-dimensional Structure of the Lipoyl domain from Bacillus stearothermophilus Pyruvate Dehydrogenase Multienzyme Complex," *J Mol Biol*, vol. 229, no. 4, pp. 1037–1048, Feb. 1993, doi: 10.1006/jmbi.1993.1103.

[73] N. G. Wallis, M. D. Allen, R. W. Broadhurst, I. A. D. Lessard, and R. N. Perham, "Recognition of a Surface Loop of the Lipoyl Domain Underlies Substrate Channelling in the Pyruvate Dehydrogenase Multienzyme Complex," *J Mol Biol*, vol. 263, no. 3, pp. 463–474, Nov. 1996, doi: 10.1006/jmbi.1996.0589.

[74] T. W. Morris, K. E. Reed, and J. E. Cronan, "Identification of the gene encoding lipoate-protein ligase A of Escherichia coli. Molecular cloning and characterization of the lplA gene and gene product.," *J Biol Chem*, vol. 269, no. 23, pp. 16091–100, Jun. 1994.

[75] S. W. Jordan and J. E. Cronan, “The Escherichia coli lipB gene encodes lipoyl (octanoyl)-acyl carrier protein:protein transferase.,” *J Bacteriol*, vol. 185, no. 5, pp. 1582–9, Mar. 2003, doi: 10.1128/JB.185.5.1582-1589.2003.

[76] D. J. O’KANE and I. C. GUNSALUS, “Accessory factor requirement for pyruvate oxidation.,” *J Bacteriol*, vol. 54, no. 1, p. 20, Jul. 1947.

[77] L. J. Reed *et al.*, “Isolation, Characterization and Structure of α-Lipoic Acid [1],” *J Am Chem Soc*, vol. 75, no. 6, pp. 1267–1270, Mar. 1953, doi: 10.1021/ja01102a001.

[78] L. J. Reed, B. G. DeBusk, I. C. Gunsalus, and C. S. Hornberger, “Crystalline α-Lipoic Acid: A Catalytic Agent Associated with Pyruvate Dehydrogenase,” *Science (1979)*, vol. 114, no. 2952, pp. 93–94, Jul. 1951, doi: 10.1126/science.114.2952.93.

[79] N. Vallianou, A. Evangelopoulos, and P. Koutalas, “Alpha-lipoic Acid and diabetic neuropathy.,” *Rev Diabet Stud*, vol. 6, no. 4, pp. 230–6, 2009, doi: 10.1900/RDS.2009.6.230.

[80] J. R. Miller *et al.*, “Escherichia coli LipA is a lipoyl synthase: in vitro biosynthesis of lipoylated pyruvate dehydrogenase complex from octanoyl-acyl carrier protein.,” *Biochemistry*, vol. 39, no. 49, pp. 15166–78, Dec. 2000, doi: 10.1021/bi002060n.

[81] S. J. Booker, “Unraveling the Pathway of Lipoic Acid Biosynthesis,” *Chem Biol*, vol. 11, no. 1, pp. 10–12, Jan. 2004, doi: 10.1016/j.chembiol.2004.01.002.

[82] A. Mattevi *et al.*, “Atomic Structure of the Cubic Core of the Pyruvate Dehydrogenase Multienzyme Eomplex,” *Science (1979)*, vol. 255, no. 5051, pp. 1544–1550, Mar. 1992, doi: 10.1126/science.1549782.

[83] W. v. Shaw, “Chloramphenicol Acetyltransferase: Enzymology and Molecular Biology,” *Critical Reviews in Biochemistry*, vol. 14, no. 1, pp. 1–46, Jan. 1983, doi: 10.3109/10409238309102789.

[84] A. Mattevi, G. Obmolova, K. H. Kalk, A. Teplyakov, and W. G. Hol, “Crystallographic analysis of substrate binding and catalysis in dihydrolipoyl transacetylase (E2p).,” *Biochemistry*, vol. 32, no. 15, pp. 3887–901, Apr. 1993, doi: 10.1021/bi00066a007.

[85] G. C. Russell and J. R. Guest, “Site-directed mutagenesis of the lipoate acetyltransferase of Escherichia coli.,” *Proc Biol Sci*, vol. 243, no. 1307, pp. 155–60, Feb. 1991, doi: 10.1098/rspb.1991.0025.

[86] M. Kato, R. M. Wynn, J. L. Chuang, C. A. Brautigam, M. Custorio, and D. T. Chuang, “A synchronized substrate-gating mechanism revealed by cubic-core structure of the bovine branched-chain α-ketoacid dehydrogenase complex,” *EMBO J*, vol. 25, no. 24, pp. 5983–5994, Dec. 2006, doi: 10.1038/sj.emboj.7601444.

[87] K. Chandrasekhar *et al.*, “Insight to the Interaction of the Dihydrolipoamide Acetyltransferase (E2) Core with the Peripheral Components in the Escherichia coli Pyruvate Dehydrogenase Complex via Multifaceted Structural Approaches,” *Journal of Biological Chemistry*, vol. 288, no. 21, pp. 15402–15417, May 2013, doi: 10.1074/jbc.M113.466789.

[88] R. Bryk *et al.*, “Triazaspirodimethoxybenzoyls as selective inhibitors of mycobacterial lipoamide dehydrogenase .,” *Biochemistry*, vol. 49, no. 8, pp. 1616–27, Mar. 2010, doi: 10.1021/bi9016186.

[89] C. A. Brautigam, J. L. Chuang, D. R. Tomchick, M. Machius, and D. T. Chuang, “Crystal structure of human dihydrolipoamide dehydrogenase: NAD+/NADH binding and the structural basis of disease-causing mutations.,” *J Mol Biol*, vol. 350, no. 3, pp. 543–52, Jul. 2005, doi: 10.1016/j.jmb.2005.05.014.

[90] R. G. Matthews, D. P. Ballou, C. Thorpe, and C. H. Williams, “Ion pair formation in pig heart lipoamide dehydrogenase: rationalization of pH profiles for reactivity of oxidized enzyme with dihydrolipoamide and 2-electron-reduced enzyme with

lipoamide and iodoacetamide.," *Journal of Biological Chemistry*, vol. 252, no. 10, pp. 3199–3207, May 1977, doi: 10.1016/S0021-9258(17)40371-1.

[91] C. Thorpe and C. H. Williams, "Differential reactivity of the two active site cysteine residues generated on reduction of pig heart lipoamide dehydrogenase.," *Journal of Biological Chemistry*, vol. 251, no. 12, pp. 3553–3557, Jun. 1976, doi: 10.1016/S0021-9258(17)33379-3.

[92] C. Zhang and S.-H. Kim, "Overview of structural genomics: from structure to function," *Curr Opin Chem Biol*, vol. 7, no. 1, pp. 28–32, Feb. 2003, doi: 10.1016/S1367-5931(02)00015-7.

[93] D. Fischer, H. Wolfson, S. L. Lin, and R. Nussinov, "Three-dimensional, sequence order-independent structural comparison of a serine protease against the crystallographic database reveals active site similarities: Potential implications to evolution and to protein folding," *Protein Science*, vol. 3, no. 5, pp. 769–778, May 1994, doi: 10.1002/pro.5560030506.

[94] Y. Cho, K. Y. Hwang, J. H. Chung, S.-H. Kim, and Y. S. Han, "Structure-based identification of a novel NTPase from Methanococcus jannaschii," *Nat Struct Biol*, vol. 6, no. 7, pp. 691–696, Jul. 1999, doi: 10.1038/10745.

[95] J. C. Kendrew, G. Bodo, H. M. Dintzis, R. G. Parrish, H. Wyckoff, and D. C. Phillips, "A Three-Dimensional Model of the Myoglobin Molecule Obtained by X-Ray Analysis," *Nature*, vol. 181, no. 4610, pp. 662–666, Mar. 1958, doi: 10.1038/181662a0.

[96] H. Yu, "Extending the size limit of protein nuclear magnetic resonance," *Proceedings of the National Academy of Sciences*, vol. 96, no. 2, pp. 332–334, Jan. 1999, doi: 10.1073/pnas.96.2.332.

[97] K. M. Yip, N. Fischer, E. Paknia, A. Chari, and H. Stark, "Atomic-resolution protein structure determination by cryo-EM.," *Nature*, vol. 587, no. 7832, pp. 157–161, Nov. 2020, doi: 10.1038/s41586-020-2833-4.

[98] J. Schrader *et al.*, "The inhibition mechanism of human 20S proteasomes enables next-generation inhibitor design.," *Science*, vol. 353, no. 6299, pp. 594–8, Aug. 2016, doi: 10.1126/science.aaf8993.

[99] F. Henneberg and A. Chari, "Chromatography-Free Purification Strategies for Large Biological Macromolecular Complexes Involving Fractionated PEG Precipitation and Density Gradients.," *Life (Basel)*, vol. 11, no. 12, Nov. 2021, doi: 10.3390/life11121289.

[100] K. Singh *et al.*, "Discovery of a Regulatory Subunit of the Yeast Fatty Acid Synthase.," *Cell*, vol. 180, no. 6, pp. 1130-1143.e20, Mar. 2020, doi: 10.1016/j.cell.2020.02.034.

[101] J. R. Helliwell, "New developments in crystallography: exploring its technology, methods and scope in the molecular biosciences.," *Biosci Rep*, vol. 37, no. 4, Aug. 2017, doi: 10.1042/BSR20170204.

[102] J. Holcomb, N. Spellmon, Y. Zhang, M. Doughan, C. Li, and Z. Yang, "Protein crystallization: Eluding the bottleneck of X-ray crystallography.," *AIMS Biophys*, vol. 4, no. 4, pp. 557–575, 2017, doi: 10.3934/biophy.2017.4.557.

[103] A. Mozzarelli and G. L. Rossi, "Protein function in the crystal.," *Annu Rev Biophys Biomol Struct*, vol. 25, pp. 343–65, 1996, doi: 10.1146/annurev.bb.25.060196.002015.

[104] J. A. Rupley and Fasman G. D., "Structure and Stability of Biological Macromolecules," 1969, pp. 291–352.

[105] M. W. Makinen and A. L. Fink, "Reactivity and cryoenzymology of enzymes in the crystalline state," *Annu Rev Biophys Bioeng*, vol. 6, no. 1, pp. 301–343, Jun. 1977, doi: 10.1146/annurev.bb.06.060177.001505.

[106] S. Matsumoto *et al.*, "Molecular Mechanism for Conformational Dynamics of Ras·GTP Elucidated from In-Situ Structural Transition in Crystal," *Sci Rep*, vol. 6, no. 1, p. 25931, May 2016, doi: 10.1038/srep25931.
[107] E. Hohenester and J. N. Jansonius, "Crystalline mitochondrial aspartate aminotransferase exists in only two conformations," *J Mol Biol*, vol. 236, no. 4, pp. 963–968, Mar. 1994, doi: 10.1016/0022-2836(94)90001-9.
[108] A. Bar-Even *et al.*, "The Moderately Efficient Enzyme: Evolutionary and Physicochemical Trends Shaping Enzyme Parameters," *Biochemistry*, vol. 50, no. 21, pp. 4402–4410, May 2011, doi: 10.1021/bi2002289.
[109] P. Douzou, G. Hui Bon Hoa, and G. A. Petsko, "Protein crystallography at sub-zero temperatures: Lysozyme-substrate complexes in cooled mixed solvents," *J Mol Biol*, vol. 96, no. 3, pp. 367–380, Aug. 1975, doi: 10.1016/0022-2836(75)90166-7.
[110] P. Mehrabi *et al.*, "Milisecond cryo-trapping by the spitrobot crystal plunger simplifies time-resolved crystallography," *bioRXiv preprint*, 2022.
[111] T. Dissanayake, J. M. Swails, M. E. Harris, A. E. Roitberg, and D. M. York, "Interpretation of pH-activity profiles for acid-base catalysis from molecular simulations.," *Biochemistry*, vol. 54, no. 6, pp. 1307–13, Feb. 2015, doi: 10.1021/bi5012833.
[112] J. Wang and E. R. Kantrowitz, "Trapping the tetrahedral intermediate in the alkaline phosphatase reaction by substitution of the active site serine with threonine.," *Protein Sci*, vol. 15, no. 10, pp. 2395–401, Oct. 2006, doi: 10.1110/ps.062351506.
[113] G. Wille, D. Meyer, A. Steinmetz, E. Hinze, R. Golbik, and K. Tittmann, "The catalytic cycle of a thiamin diphosphate enzyme examined by cryocrystallography," *Nat Chem Biol*, vol. 2, no. 6, pp. 324–328, Jun. 2006, doi: 10.1038/nchembio788.
[114] C. J. Jackson *et al.*, "In Crystallo Capture of a Michaelis Complex and Product-binding Modes of a Bacterial Phosphotriesterase," *J Mol Biol*, vol. 375, no. 5, pp. 1189–1196, Feb. 2008, doi: 10.1016/j.jmb.2007.10.061.
[115] W. Xie, X. Liu, and R. H. Huang, "Chemical trapping and crystal structure of a catalytic tRNA guanine transglycosylase covalent intermediate," *Nat Struct Mol Biol*, vol. 10, no. 10, pp. 781–788, Oct. 2003, doi: 10.1038/nsb976.
[116] F. Rabe von Pappenheim, M. Aldeghi, B. Shome, T. Begley, B. L. de Groot, and K. Tittmann, "Structural basis for antibiotic action of the B1 antivitamin 2′-methoxythiamine," *Nat Chem Biol*, vol. 16, no. 11, pp. 1237–1245, Nov. 2020, doi: 10.1038/s41589-020-0628-4.
[117] Z. Ren, D. Bourgeois, J. R. Helliwell, K. Moffat, V. Šrajer, and B. L. Stoddard, "Laue crystallography: coming of age," *J Synchrotron Radiat*, vol. 6, no. 4, pp. 891–917, Jul. 1999, doi: 10.1107/S0909049599006366.
[118] K. Moffat, D. Szebenyi, and D. Bilderback, "X-ray Laue Diffraction from Protein Crystals.," *Science*, vol. 223, no. 4643, pp. 1423–5, Mar. 1984, doi: 10.1126/science.223.4643.1423.
[119] D. Bourgeois, F. Schotte, M. Brunori, and B. Vallone, "Time-resolved methods in biophysics. 6. Time-resolved Laue crystallography as a tool to investigate photoactivated protein dynamics," *Photochemical & Photobiological Sciences*, vol. 6, no. 10, pp. 1047–1056, Oct. 2007, doi: 10.1039/b704249c.
[120] M. L. Grünbein *et al.*, "Illumination guidelines for ultrafast pump-probe experiments by serial femtosecond crystallography.," *Nat Methods*, vol. 17, no. 7, pp. 681–684, Jul. 2020, doi: 10.1038/s41592-020-0847-3.
[121] M. Levantino, B. A. Yorke, D. C. Monteiro, M. Cammarata, and A. R. Pearson, "Using synchrotrons and XFELs for time-resolved X-ray crystallography and solution scattering experiments on biomolecules," *Curr Opin Struct Biol*, vol. 35, pp. 41–48, Dec. 2015, doi: 10.1016/j.sbi.2015.07.017.

[122] H. N. Chapman, C. Caleman, and N. Timneanu, “Diffraction before destruction,” *Philosophical Transactions of the Royal Society B: Biological Sciences*, vol. 369, no. 1647, p. 20130313, Jul. 2014, doi: 10.1098/rstb.2013.0313.
[123] G. Ortega, M. Pons, and O. Millet, “Protein Functional Dynamics in Multiple Timescales as Studied by NMR Spectroscopy,” 2013, pp. 219–251. doi: 10.1016/B978-0-12-411636-8.00006-7.
[124] P. K. Agarwal, “Enzymes: An integrated view of structure, dynamics and function,” *Microb Cell Fact*, vol. 5, no. 1, p. 2, Dec. 2006, doi: 10.1186/1475-2859-5-2.
[125] D. C. F. Monteiro, E. Amoah, C. Rogers, and A. R. Pearson, “Using photocaging for fast time-resolved structural biology studies,” *Acta Crystallogr D Struct Biol*, vol. 77, no. 10, pp. 1218–1232, Oct. 2021, doi: 10.1107/S2059798321008809.
[126] K. R. Beyerlein *et al.*, “Mix-and-diffuse serial synchrotron crystallography.,” *IUCrJ*, vol. 4, no. Pt 6, pp. 769–777, Nov. 2017, doi: 10.1107/S2052252517013124.
[127] T. Weinert *et al.*, “Proton uptake mechanism in bacteriorhodopsin captured by serial synchrotron crystallography,” *Science (1979)*, vol. 365, no. 6448, pp. 61–65, Jul. 2019, doi: 10.1126/science.aaw8634.
[128] P. Nogly *et al.*, “Lipidic cubic phase injector is a viable crystal delivery system for time-resolved serial crystallography,” *Nat Commun*, vol. 7, no. 1, p. 12314, Nov. 2016, doi: 10.1038/ncomms12314.
[129] E. C. Schulz, B. A. Yorke, A. R. Pearson, and P. Mehrabi, “Best practices for time-resolved serial synchrotron crystallography,” *Acta Crystallogr D Struct Biol*, vol. 78, no. 1, pp. 14–29, Jan. 2022, doi: 10.1107/S2059798321011621.
[130] E. C. Schulz *et al.*, “The hit-and-return system enables efficient time-resolved serial synchrotron crystallography,” *Nat Methods*, vol. 15, no. 11, pp. 901–904, Nov. 2018, doi: 10.1038/s41592-018-0180-2.
[131] J. Tenboer *et al.*, “Time-resolved serial crystallography captures high-resolution intermediates of photoactive yellow protein,” *Science (1979)*, vol. 346, no. 6214, pp. 1242–1246, Dec. 2014, doi: 10.1126/science.1259357.
[132] J. Woodhouse *et al.*, “Photoswitching mechanism of a fluorescent protein revealed by time-resolved crystallography and transient absorption spectroscopy,” *Nat Commun*, vol. 11, no. 1, p. 741, Feb. 2020, doi: 10.1038/s41467-020-14537-0.
[133] T. Tosha *et al.*, “Capturing an initial intermediate during the P450nor enzymatic reaction using time-resolved XFEL crystallography and caged-substrate,” *Nat Commun*, vol. 8, no. 1, p. 1585, Nov. 2017, doi: 10.1038/s41467-017-01702-1.
[134] J. de Mos, A. Jakob, J. Becker-Baldus, A. Heckel, and C. Glaubitz, “Light-Induced Uncaging for Time-Resolved Observations of Biochemical Reactions by MAS NMR Spectroscopy.,” *Chemistry*, vol. 26, no. 30, pp. 6789–6792, May 2020, doi: 10.1002/chem.202000770.
[135] M. Schmidt, “Mix and Inject: Reaction Initiation by Diffusion for Time-Resolved Macromolecular Crystallography,” *Advances in Condensed Matter Physics*, vol. 2013, pp. 1–10, 2013, doi: 10.1155/2013/167276.
[136] P. Mehrabi *et al.*, “Liquid application method for time-resolved analyses by serial synchrotron crystallography,” *Nat Methods*, vol. 16, no. 10, pp. 979–982, Oct. 2019, doi: 10.1038/s41592-019-0553-1.
[137] D. von Stetten *et al.*, “TREXX: a new endstation for serial time-resolved crystallography at PETRA III,” *Acta Crystallogr A Found Adv*, vol. 75, no. a2, pp. e26–e26, Aug. 2019, doi: 10.1107/S2053273319095305.
[138] J. Škerlová, J. Berndtsson, H. Nolte, M. Ott, and P. Stenmark, “Structure of the native pyruvate dehydrogenase complex reveals the mechanism of substrate insertion,” *Nat Commun*, vol. 12, no. 1, p. 5277, Sep. 2021, doi: 10.1038/s41467-021-25570-y.

[139] E. M. Bruch *et al.*, “Actinobacteria challenge the paradigm: A unique protein architecture for a well-known, central metabolic complex,” *Proceedings of the National Academy of Sciences*, vol. 118, no. 48, Nov. 2021, doi: 10.1073/pnas.2112107118.
[140] A. Mattevi, G. Obmolova, K. H. Kalk, A. Teplyakov, and W. G. J. Hol, “Crystallographic analysis of substrate binding and catalysis in dihydrolipoyl transacetylase (E2p),” *Biochemistry*, vol. 32, no. 15, pp. 3887–3901, Apr. 1993, doi: 10.1021/bi00066a007.
[141] L. D. Graham and R. N. Perham, “Interactions of lipoyl domains with the E1p subunits of the pyruvate dehydrogenase multienzyme complex from *Escherichia coli*,” *FEBS Lett*, vol. 262, no. 2, pp. 241–244, Mar. 1990, doi: 10.1016/0014-5793(90)80200-3.
[142] L. D. Graham, L. C. Packman, and R. N. Perham, “Kinetics and specificity of reductive acylation of lipoyl domains from 2-oxo acid dehydrogenase multienzyme complexes.,” *Biochemistry*, vol. 28, no. 4, pp. 1574–81, Feb. 1989, doi: 10.1021/bi00430a023.
[143] J. Newman, “Novel buffer systems for macromolecular crystallization,” *Acta Crystallogr D Biol Crystallogr*, vol. 60, no. 3, pp. 610–612, Mar. 2004, doi: 10.1107/S0907444903029640.
[144] P. R. Evans and G. N. Murshudov, “How good are my data and what is the resolution?,” *Acta Crystallogr D Biol Crystallogr*, vol. 69, no. 7, pp. 1204–1214, Jul. 2013, doi: 10.1107/S0907444913000061.
[145] C. Vonrhein *et al.*, “Data processing and analysis with the autoPROC toolbox,” *Acta Crystallogr D Biol Crystallogr*, vol. 67, no. 4, pp. 293–302, Apr. 2011, doi: 10.1107/S0907444911007773.
[146] M. D. Winn *et al.*, “Overview of the CCP4 suite and current developments,” *Acta Crystallogr D Biol Crystallogr*, vol. 67, no. 4, pp. 235–242, Apr. 2011, doi: 10.1107/S0907444910045749.
[147] P. Emsley and K. Cowtan, “Coot: model-building tools for molecular graphics,” *Acta Crystallogr D Biol Crystallogr*, vol. 60, no. 12, pp. 2126–2132, Dec. 2004, doi: 10.1107/S0907444904019158.
[148] T. A. White *et al.*, “CrystFEL: a software suite for snapshot serial crystallography,” *J Appl Crystallogr*, vol. 45, no. 2, pp. 335–341, Apr. 2012, doi: 10.1107/S0021889812002312.
[149] A. A. Lebedev, P. Young, M. N. Isupov, O. v. Moroz, A. A. Vagin, and G. N. Murshudov, “JLigand: a graphical tool for the CCP4 template-restraint library,” *Acta Crystallogr D Biol Crystallogr*, vol. 68, no. 4, pp. 431–440, Apr. 2012, doi: 10.1107/S090744491200251X.
[150] P. Evans, “Scaling and assessment of data quality,” *Acta Crystallogr D Biol Crystallogr*, vol. 62, no. 1, pp. 72–82, Jan. 2006, doi: 10.1107/S0907444905036693.
[151] E. Gasteiger *et al.*, “Protein Identification and Analysis Tools on the ExPASy Server,” in *The Proteomics Protocols Handbook*, Totowa, NJ: Humana Press, 2005, pp. 571–607. doi: 10.1385/1-59259-890-0:571.
[152] G. N. Murshudov *et al.*, “REFMAC5 for the refinement of macromolecular crystal structures,” *Acta Crystallogr D Biol Crystallogr*, vol. 67, no. 4, pp. 355–367, Apr. 2011, doi: 10.1107/S0907444911001314.
[153] W. Kabsch, “XDS,” *Acta Crystallogr D Biol Crystallogr*, vol. 66, no. 2, pp. 125–132, Feb. 2010, doi: 10.1107/S0907444909047337.
[154] D. G. Gibson, L. Young, R.-Y. Chuang, J. C. Venter, C. A. Hutchison, and H. O. Smith, “Enzymatic assembly of DNA molecules up to several hundred kilobases,” *Nat Methods*, vol. 6, no. 5, pp. 343–345, May 2009, doi: 10.1038/nmeth.1318.

[155] D. F. Swinehart, “The Beer-Lambert Law,” *J Chem Educ*, vol. 39, no. 7, p. 333, Jul. 1962, doi: 10.1021/ed039p333.
[156] S. Frey and D. Görlich, “A new set of highly efficient, tag-cleaving proteases for purifying recombinant proteins,” *J Chromatogr A*, vol. 1337, pp. 95–105, Apr. 2014, doi: 10.1016/j.chroma.2014.02.029.
[157] D. von Stetten *et al.*, “TREXX: a new endstation for serial time-resolved crystallography at PETRA III,” *Acta Crystallogr A Found Adv*, vol. 75, no. a2, pp. e26–e26, Aug. 2019, doi: 10.1107/S2053273319095305.
[158] B. Norton-Baker *et al.*, “A simple vapor-diffusion method enables protein crystallization inside the HARE serial crystallography chip,” *Acta Crystallogr D Struct Biol*, vol. 77, no. 6, pp. 820–834, Jun. 2021, doi: 10.1107/S2059798321003855.
[159] I. Melnikov, O. Svensson, G. Bourenkov, G. Leonard, and A. Popov, “The complex analysis of X-ray mesh scans for macromolecular crystallography,” *Acta Crystallogr D Struct Biol*, vol. 74, no. 4, pp. 355–365, Apr. 2018, doi: 10.1107/S2059798318002735.
[160] D. Meyer *et al.*, “Unexpected tautomeric equilibria of the carbanion-enamine intermediate in pyruvate oxidase highlight unrecognized chemical versatility of thiamin.,” *Proc Natl Acad Sci U S A*, vol. 109, no. 27, pp. 10867–72, Jul. 2012, doi: 10.1073/pnas.1201280109.
[161] A. R. Pearson and P. Mehrabi, “Serial synchrotron crystallography for time-resolved structural biology,” *Curr Opin Struct Biol*, vol. 65, pp. 168–174, Dec. 2020, doi: 10.1016/j.sbi.2020.06.019.
[162] S. G. F. Rasmussen *et al.*, “Crystal structure of the β2 adrenergic receptor–Gs protein complex,” *Nature*, vol. 477, no. 7366, pp. 549–555, Sep. 2011, doi: 10.1038/nature10361.
[163] E. Pardon *et al.*, “A general protocol for the generation of Nanobodies for structural biology,” *Nat Protoc*, vol. 9, no. 3, pp. 674–693, Mar. 2014, doi: 10.1038/nprot.2014.039.
[164] T. Pleiner *et al.*, “Nanobodies: site-specific labeling for super-resolution imaging, rapid epitope-mapping and native protein complex isolation.,” *Elife*, vol. 4, p. e11349, Dec. 2015, doi: 10.7554/eLife.11349.
[165] C. Kupitz, I. Grotjohann, C. E. Conrad, S. Roy-Chowdhury, R. Fromme, and P. Fromme, “Microcrystallization techniques for serial femtosecond crystallography using photosystem II from *Thermosynechococcus elongatus* as a model system,” *Philosophical Transactions of the Royal Society B: Biological Sciences*, vol. 369, no. 1647, p. 20130316, Jul. 2014, doi: 10.1098/rstb.2013.0316.
[166] R. Bücker *et al.*, “Serial protein crystallography in an electron microscope.,” *Nat Commun*, vol. 11, no. 1, p. 996, Feb. 2020, doi: 10.1038/s41467-020-14793-0.
[167] P. Mehrabi *et al.*, “Time-resolved crystallography reveals allosteric communication aligned with molecular breathing.,” *Science*, vol. 365, no. 6458, pp. 1167–1170, Sep. 2019, doi: 10.1126/science.aaw9904.
[168] T. Moreno-Chicano *et al.*, “High-throughput structures of protein–ligand complexes at room temperature using serial femtosecond crystallography,” *IUCrJ*, vol. 6, no. 6, pp. 1074–1085, Nov. 2019, doi: 10.1107/S2052252519011655.
[169] M. J. Wheeler, S. Russi, M. G. Bowler, and M. W. Bowler, “Measurement of the equilibrium relative humidity for common precipitant concentrations: facilitating controlled dehydration experiments.,” *Acta Crystallogr Sect F Struct Biol Cryst Commun*, vol. 68, no. Pt 1, pp. 111–4, Jan. 2012, doi: 10.1107/S1744309111054029.

[170] J. Sanchez-Weatherby and I. Moraes, “Crystal Dehydration in Membrane Protein Crystallography.,” *Adv Exp Med Biol*, vol. 922, pp. 73–89, 2016, doi: 10.1007/978-3-319-35072-1_6.
[171] M. Senda, T. Hayashi, M. Hatakeyama, K. Takeuchi, A. T. Sasaki, and T. Senda, “Use of Multiple Cryoprotectants to Improve Diffraction Quality from Protein Crystals,” *Cryst Growth Des*, vol. 16, no. 3, pp. 1565–1571, Mar. 2016, doi: 10.1021/acs.cgd.5b01692.
[172] I. Russo Krauss, F. Sica, C. A. Mattia, and A. Merlino, “Increasing the X-ray diffraction power of protein crystals by dehydration: the case of bovine serum albumin and a survey of literature data.,” *Int J Mol Sci*, vol. 13, no. 3, pp. 3782–3800, 2012, doi: 10.3390/ijms13033782.
[173] J. R. Helliwell, “Protein crystal perfection and its application,” *Acta Crystallogr D Biol Crystallogr*, vol. 61, no. 6, pp. 793–798, Jun. 2005, doi: 10.1107/S0907444905001368.
[174] U. Chinte, B. Shah, K. DeWitt, K. Kirschbaum, A. A. Pinkerton, and C. Schall, “Sample size: an important parameter in flash-cooling macromolecular crystallization solutions,” *J Appl Crystallogr*, vol. 38, no. 3, pp. 412–419, Jun. 2005, doi: 10.1107/S0021889805005029.
[175] W. Shin, J. Pletcher, G. Blank, and M. Sax, “Ring stacking interactions between thiamin and planar molecules as seen in the crystal structure of a thiamin picrolonate dihydrate complex.,” *J Am Chem Soc*, vol. 99, no. 10, pp. 3491–9, May 1977, doi: 10.1021/ja00452a050.
[176] N.-S. Hsu *et al.*, “The Mesomeric Effect of Thiazolium on non-Kekulé Diradicals in *Pichia stipitis* Transketolase,” *Angewandte Chemie International Edition*, vol. 57, no. 7, pp. 1802–1807, Feb. 2018, doi: 10.1002/anie.201709799.
[177] L. S. Leung and P. A. Frey, “Fluoropyruvate: An unusual substrate for Escherichia coli pyruvate dehydrogenase,” *Biochem Biophys Res Commun*, vol. 81, no. 2, pp. 274–279, Mar. 1978, doi: 10.1016/0006-291X(78)91529-2.
[178] K. J. Gruys, C. J. Halkides, and P. A. Frey, “Synthesis and properties of 2-acetylthiamin pyrophosphate: an enzymatic reaction intermediate,” *Biochemistry*, vol. 26, no. 24, pp. 7575–7585, Dec. 1987, doi: 10.1021/bi00398a007.
[179] R. Suzuki *et al.*, “Crystal structures of phosphoketolase: thiamine diphosphate-dependent dehydration mechanism.,” *J Biol Chem*, vol. 285, no. 44, pp. 34279–87, Oct. 2010, doi: 10.1074/jbc.M110.156281.
[180] S. S. Pang, R. G. Duggleby, R. L. Schowen, and L. W. Guddat, “The Crystal Structures of Klebsiella pneumoniae Acetolactate Synthase with Enzyme-bound Cofactor and with an Unusual Intermediate,” *Journal of Biological Chemistry*, vol. 279, no. 3, pp. 2242–2253, Jan. 2004, doi: 10.1074/jbc.M304038200.
[181] V. I. Bunik and D. Degtyarev, “Structure-function relationships in the 2-oxo acid dehydrogenase family: Substrate-specific signatures and functional predictions for the 2-oxoglutarate dehydrogenase-like proteins,” *Proteins: Structure, Function, and Bioinformatics*, vol. 71, no. 2, pp. 874–890, May 2008, doi: 10.1002/prot.21766.
[182] L. D. Graham, L. C. Packman, and R. N. Perham, “Kinetics and specificity of reductive acylation of lipoyl domains from 2-oxo acid dehydrogenase multienzyme complexes,” *Biochemistry*, vol. 28, no. 4, pp. 1574–1581, Feb. 1989, doi: 10.1021/bi00430a023.
[183] L. J. Reed, M. Koike, M. E. Levitch, and F. R. Leach, “Studies on the nature and reactions of protein-bound lipoic acid,” *Journal of Biological Chemistry*, vol. 232, no. 1, pp. 143–158, May 1958, doi: 10.1016/S0021-9258(18)70382-7.
[184] M. A. Moxley, D. A. Beard, and J. N. Bazil, “Global Kinetic Analysis of Mammalian E3 Reveals pH-dependent NAD+/NADH Regulation, Physiological Kinetic

Reversibility, and Catalytic Optimum," *Journal of Biological Chemistry*, vol. 291, no. 6, pp. 2712–2730, Feb. 2016, doi: 10.1074/jbc.M115.676619.
[185] R. D. Bach, O. Dmitrenko, and C. Thorpe, "Mechanism of Thiolate−Disulfide Interchange Reactions in Biochemistry," *J Org Chem*, vol. 73, no. 1, pp. 12–21, Jan. 2008, doi: 10.1021/jo702051f.
[186] J. Benen, W. Berkel, C. Veeger, and A. Kok, "Lipoamide dehydrogenase from Azotobacter vinelandii. The role of the C-terminus in catalysis and dimer stabilization," *Eur J Biochem*, vol. 207, no. 2, pp. 499–505, Jul. 1992, doi: 10.1111/j.1432-1033.1992.tb17076.x.
[187] F. L. Kyrilis *et al.*, "Integrative structure of a 10-megadalton eukaryotic pyruvate dehydrogenase complex from native cell extracts," *Cell Rep*, vol. 34, no. 6, p. 108727, Feb. 2021, doi: 10.1016/j.celrep.2021.108727.
[188] S. Prajapati *et al.*, "Structural and Functional Analyses of the Human PDH Complex Suggest a 'Division-of-Labor' Mechanism by Local E1 and E3 Clusters," *Structure*, vol. 27, no. 7, pp. 1124-1136.e4, Jul. 2019, doi: 10.1016/j.str.2019.04.009.
[189] S. Liu, X. Xia, J. Zhen, Z. Li, and Z. H. Zhou, "Structures and comparison of endogenous 2-oxoglutarate and pyruvate dehydrogenase complexes from bovine kidney," *Cell Discov*, vol. 8, no. 1, p. 126, Nov. 2022, doi: 10.1038/s41421-022-00487-y.
[190] P. Mehrabi *et al.*, "The HARE chip for efficient time-resolved serial synchrotron crystallography," *J Synchrotron Radiat*, vol. 27, no. 2, pp. 360–370, Mar. 2020, doi: 10.1107/S1600577520000685.
[191] J. D. BERNAL and D. CROWFOOT, "X-Ray Photographs of Crystalline Pepsin," *Nature*, vol. 133, no. 3369, pp. 794–795, May 1934, doi: 10.1038/133794b0.
[192] M. L. Shelby *et al.*, "A fixed-target platform for serial femtosecond crystallography in a hydrated environment," *IUCrJ*, vol. 7, no. 1, pp. 30–41, Jan. 2020, doi: 10.1107/S2052252519014003.
[193] S. Oghbaey *et al.*, "Fixed target combined with spectral mapping: approaching 100% hit rates for serial crystallography," *Acta Crystallogr D Struct Biol*, vol. 72, no. 8, pp. 944–955, Aug. 2016, doi: 10.1107/S2059798316010834.
[194] B. W. Low, C. C. H. Chen, J. E. Berger, L. Singman, and J. F. Pletcher, "Studies of insulin crystals at low temperatures: effects on mosaic character and radiation sensitivity," *Proceedings of the National Academy of Sciences*, vol. 56, no. 6, pp. 1746–1750, Dec. 1966, doi: 10.1073/pnas.56.6.1746.
[195] E. F. Garman and T. R. Schneider, "Macromolecular Cryocrystallography," *J Appl Crystallogr*, vol. 30, no. 3, pp. 211–237, Jun. 1997, doi: 10.1107/S0021889897002677.
[196] B. N. Shah, U. Chinte, S. J. Tomanicek, B. L. Hanson, and C. A. Schall, "Flash Cooling Protein Crystals: Estimate of Cryoprotectant Concentration Using Thermal Properties," *Cryst Growth Des*, vol. 11, no. 5, pp. 1493–1501, May 2011, doi: 10.1021/cg1013939.
[197] K. Diederichs, "Crystallographic Data and Model Quality," 2016, pp. 147–173. doi: 10.1007/978-1-4939-2763-0_10.
[198] P. Mehrabi, D. von Stetten, J.-P. Leimkohl, F. Tellkamp, and E. C. Schulz, "An environmental control box for serial crystallography enables multi-dimensional experiments," *bioRxiv pre-print*, 2021.
[199] T. A. White *et al.*, "*CrystFEL* : a software suite for snapshot serial crystallography," *J Appl Crystallogr*, vol. 45, no. 2, pp. 335–341, Apr. 2012, doi: 10.1107/S0021889812002312.

[200] L. Ronda, S. Bruno, S. Bettati, P. Storici, and A. Mozzarelli, “From protein structure to function via single crystal optical spectroscopy,” *Front Mol Biosci*, vol. 2, Apr. 2015, doi: 10.3389/fmolb.2015.00012.
[201] R. Henderson, “Cryo-protection of protein crystals against radiation damage in electron and X-ray diffraction,” *Proc R Soc Lond B Biol Sci*, vol. 241, no. 1300, pp. 6–8, Jul. 1990, doi: 10.1098/rspb.1990.0057.
[202] R. L. Owen, E. Rudiño-Piñera, and E. F. Garman, “Experimental determination of the radiation dose limit for cryocooled protein crystals,” *Proceedings of the National Academy of Sciences*, vol. 103, no. 13, pp. 4912–4917, Mar. 2006, doi: 10.1073/pnas.0600973103.
[203] M. Weik *et al.*, “Specific chemical and structural damage to proteins produced by synchrotron radiation,” *Proceedings of the National Academy of Sciences*, vol. 97, no. 2, pp. 623–628, Jan. 2000, doi: 10.1073/pnas.97.2.623.
[204] E. de la Mora *et al.*, “Radiation damage and dose limits in serial synchrotron crystallography at cryo- and room temperatures,” *Proceedings of the National Academy of Sciences*, vol. 117, no. 8, pp. 4142–4151, Feb. 2020, doi: 10.1073/pnas.1821522117.
[205] T. Teng and K. Moffat, “Primary radiation damage of protein crystals by an intense synchrotron X-ray beam,” *J Synchrotron Radiat*, vol. 7, no. 5, pp. 313–317, Sep. 2000, doi: 10.1107/S0909049500008694.
[206] J. M. Holton and K. A. Frankel, “The minimum crystal size needed for a complete diffraction data set,” *Acta Crystallogr D Biol Crystallogr*, vol. 66, no. 4, pp. 393–408, Apr. 2010, doi: 10.1107/S0907444910007262.
[207] R. E. Hubbard and M. Kamran Haider, “Hydrogen Bonds in Proteins: Role and Strength,” in *eLS*, Wiley, 2010. doi: 10.1002/9780470015902.a0003011.pub2.
[208] Z. Sun, Q. Liu, G. Qu, Y. Feng, and M. T. Reetz, “Utility of B-Factors in Protein Science: Interpreting Rigidity, Flexibility, and Internal Motion and Engineering Thermostability,” *Chem Rev*, vol. 119, no. 3, pp. 1626–1665, Feb. 2019, doi: 10.1021/acs.chemrev.8b00290.
[209] M. Vivoli, J. Pang, and N. J. Harmer, “A half-site multimeric enzyme achieves its cooperativity without conformational changes,” *Sci Rep*, vol. 7, no. 1, p. 16529, Nov. 2017, doi: 10.1038/s41598-017-16421-2.
[210] R. A. W. Frank, F. J. Leeper, and B. F. Luisi, “Structure, mechanism and catalytic duality of thiamine-dependent enzymes,” *Cellular and Molecular Life Sciences*, vol. 64, no. 7–8, pp. 892–905, Apr. 2007, doi: 10.1007/s00018-007-6423-5.
[211] M. Prejanò, F. E. Medina, M. J. Ramos, N. Russo, P. A. Fernandes, and T. Marino, “How the Destabilization of a Reaction Intermediate Affects Enzymatic Efficiency: The Case of Human Transketolase,” *ACS Catal*, vol. 10, no. 4, pp. 2872–2881, Feb. 2020, doi: 10.1021/acscatal.9b04690.
[212] A. Turano, W. Furey, J. Pletcher, M. Sax, D. Pike, and R. Kluger, “Synthesis and crystal structure of an analog of 2-(.alpha.-lactyl)thiamin, racemic methyl 2-hydroxy-2-(2-thiamin)ethylphosphonate chloride trihydrate. A conformation for a least-motion, maximum-overlap mechanism for thiamin catalysis,” *J Am Chem Soc*, vol. 104, no. 11, pp. 3089–3095, Jun. 1982, doi: 10.1021/ja00375a024.
[213] R. M. Wynn, M. Machius, J. L. Chuang, J. Li, D. R. Tomchick, and D. T. Chuang, “Roles of His291-α and His146-β′ in the Reductive Acylation Reaction Catalyzed by Human Branched-chain α-Ketoacid Dehydrogenase,” *Journal of Biological Chemistry*, vol. 278, no. 44, pp. 43402–43410, Oct. 2003, doi: 10.1074/jbc.M306204200.
[214] J. K. Howie, J. J. Houts, and D. T. Sawyer, “Oxidation-reduction chemistry of DL-.alpha.-lipoic acid, propanedithiol, and trimethylene disulfide in aprotic and in

aqueous media," *J Am Chem Soc*, vol. 99, no. 19, pp. 6323–6326, Sep. 1977, doi: 10.1021/ja00461a025.

[215] M. Machius *et al.*, "A Versatile Conformational Switch Regulates Reactivity in Human Branched-Chain α-Ketoacid Dehydrogenase," *Structure*, vol. 14, no. 2, pp. 287–298, Feb. 2006, doi: 10.1016/j.str.2005.10.009.

[216] N. Nemeria, L. Korotchkina, M. J. McLeish, G. L. Kenyon, M. S. Patel, and F. Jordan, "Elucidation of the Chemistry of Enzyme-Bound Thiamin Diphosphate Prior to Substrate Binding: Defining Internal Equilibria among Tautomeric and Ionization States," *Biochemistry*, vol. 46, no. 37, pp. 10739–10744, Sep. 2007, doi: 10.1021/bi700838q.

[217] J. A. Zoltewicz and G. Uray, "Thiamin: A Critical Evaluation of Recent Chemistry of the Pyrimidine Ring," *Bioorg Chem*, vol. 22, no. 1, pp. 1–28, Mar. 1994, doi: 10.1006/bioo.1994.1001.

[218] R. F. W. Hopmann and G. pietro Brugnoni, "Decomposition of the Yellow Form of Thiamine," *Angewandte Chemie International Edition in English*, vol. 20, no. 11, pp. 961–962, Nov. 1981, doi: 10.1002/anie.198109611.

[219] J. Hendle *et al.*, "Crystallographic and Enzymic Investigations on the Role of Ser558, His610, and Asn614 in the Catalytic Mechanism of Azotobacter vinelandii Dihydrolipoamide Acetyltransferase (E2p)," *Biochemistry*, vol. 34, no. 13, pp. 4287–4298, Apr. 1995, doi: 10.1021/bi00013a018.

[220] I. G. Kamphuis, K. H. Kalk, M. B. A. Swarte, and J. Drenth, "Structure of papain refined at 1.65 Å resolution," *J Mol Biol*, vol. 179, no. 2, pp. 233–256, Oct. 1984, doi: 10.1016/0022-2836(84)90467-4.

[221] P. Zhou, F. Tian, F. Lv, and Z. Shang, "Geometric characteristics of hydrogen bonds involving sulfur atoms in proteins," *Proteins: Structure, Function, and Bioinformatics*, vol. 76, no. 1, pp. 151–163, Jul. 2009, doi: 10.1002/prot.22327.

[222] P. A. Karplus and G. E. Schulz, "Substrate binding and catalysis by glutathione reductase as derived from refined enzyme: Substrate crystal structures at 2Å resolution," *J Mol Biol*, vol. 210, no. 1, pp. 163–180, Nov. 1989, doi: 10.1016/0022-2836(89)90298-2.

[223] A. Gora, J. Brezovsky, and J. Damborsky, "Gates of enzymes.," *Chem Rev*, vol. 113, no. 8, pp. 5871–923, Aug. 2013, doi: 10.1021/cr300384w.

[224] P. I. Lario, N. Sampson, and A. Vrielink, "Sub-atomic Resolution Crystal Structure of Cholesterol Oxidase: What Atomic Resolution Crystallography Reveals about Enzyme Mechanism and the Role of the FAD Cofactor in Redox Activity," *J Mol Biol*, vol. 326, no. 5, pp. 1635–1650, Mar. 2003, doi: 10.1016/S0022-2836(03)00054-8.